Université de Montréal

Drop-on-Demand Bioprinting of HUVECs and Capillary-Like Networks via Laser-Induced Side Transfer

par

Mahyar Erfanian

Département de pharmacologie et physiologie - Institut de génie biomédical

Faculté de médecine

Mémoire présenté en vue de l'obtention du grade de

Maîtrise ès sciences appliquées (M.Sc.A.)

en génie biomédical

Décembre 2022

Université de Montréal

Faculté de médecine

Ce mémoire intitulé

Drop-on-Demand Bioprinting of HUVECs and Capillary-Like Networks via Laser-Induced Side Transfer

présenté par

Mahyar Erfanian

a été évalué par un jury composé des personnes suivantes :

Houman Savoji
(président-rapporteur)

Christos Boutopoulos
(directeur de recherche)

Bruno Larrivée
(codirecteur)

Stéphanie Lehoux
(membre du jury)

Résumé

La fabrication de tissus biologiques a été largement étudiée pour ses applications dans la recherche, la transplantation d'organes et le dépistage de drogues. Bien que des tissus minces ou avasculaires aient été fabriqués avec succès auparavant, le maintien de la viabilité des tissus épais nécessite la présence d'un réseau capillaire tout au long de la construction pour permettre l'apport de nutriments et l'élimination des déchets cellulaires par le sang. En plus des cellules endothéliales, l'incorporation de types de cellules de soutien dans le réseau capillaire est nécessaire pour favoriser la survie et la maturation. Comparée à d'autres méthodes de biofabrication, la bioimpression est une technologie prometteuse qui permet la fabrication précise de motifs 3D complexes à haute résolution spatiale.

Nous avons conçu de nouveau notre procédé technique de bio-impression laser nommé LIST (de l'anglais *laser-induced side transfer*) dans laquelle la bioencre de la suspension cellulaire passe à travers un capillaire horizontal avec un orifice face à l'échafaudage. Lorsque le laser frappe la bioencre, une bulle se forme qui propulse une gouttelette à travers l'orifice. Nous avons mené une étude détaillée pour caractériser cette bio-impression technique et validé sa cytocompatibilité par l'évaluation de la viabilité de HUVECs imprimés grâce à LIST. Nous avons incorporé des fibroblastes et des péricytes dans nos échantillons et observé le recrutement progressif de ces cellules par les structures de type capillaire HUVEC imprimées sur Matrigel. Des images fluorescentes ont été analysées pour quantifier le recrutement de fibroblastes/péricytes au fil du temps.

Mots clés : biofabrication, bioimpression par laser, laser-induced side transfer (LIST), cellules endothéliales, angiogenèse, micro-vasculature

Abstract

The fabrication of biological tissues in laboratory settings has been widely investigated for its applications in research, organ transplantation, and drug screening. Although several previous attempts to generate avascular or thin tissues have been successful, there remains the challenge to create thick functional tissues. Maintaining the viability of thick tissues requires the presence of a capillary network throughout the construct to allow the intake of nutrients and the discard of cellular waste through blood. In addition to endothelial cells, the incorporation of supporting cell types is necessary to promote survival, maturation, and acquire in vivo-like functionality. Compared to other biofabrication methods, bioprinting is a promising technology that enables the precise fabrication of complex 3D patterns at high spatial resolution.

We have come up with a new configuration of our in-house laser-based bioprinting technique called laser-induced side transfer (LIST) in which the bioink passes through a horizontal glass capillary with an orifice facing the receiving substrate. When the laser beam causes bubble formation in the bioink, a liquid jet exits through the orifice that will eventually form a droplet. We have conducted a detailed study to characterize this bioprinting technique and validated its cytocompatibility through viability assessment of LIST-printed human umbilical vein endothelial cells (HUVECs). In an effort to generate physiological blood vessels, we incorporated fibroblasts and pericytes in our samples and observed the gradual recruitment of these cells by the printed HUVEC capillary-like structures on Matrigel. Fluorescent images were taken and analyzed to quantify the fibroblast/pericyte recruitment over time.

Keywords: biofabrication, laser-based bioprinting, laser-induced side transfer (LIST), endothelial cells, angiogenesis, micro-vasculature

Contents

List of tables

List of figures

List of acronyms

2D	two-dimensional
3D	three-dimensional
BMP9	bone morphogenetic protein 9
CAD	computer-aided design
CSL	cumulative sprout length
DAPI	4,6-diamidino-2-phenylindole
DOD	drop-on-demand
EBB	extrusion-based bioprinting

EC	endothelial cell
ECM	extracellular matrix
GFP	green fluorescent protein
HBMSC	human bone marrow mesenchymal stem cell
HBPC	human brain pericyte
HMVEC	human microvascular endothelial cell
HPMEC	human pulmonary microvascular endothelial cell
HSP	heat shock protein
HUVEC	human umbilical cord endothelial cell
HUVSMC	human umbilical vein smooth muscle cell

iPSC-EC	induced pluripotent stem cell-derived endothelial cell
LBB	laser-based bioprinting
LIFT	laser-induced forward transfer
LIST	laser-induced side transfer
MRI	magnetic resonance imaging
PC	pericyte
ROI	region of interest
SMC	smooth muscle cell
SNR	signal-to-noise ratio
VEGF	vascular endothelial growth factor

VEGFR	vascular endothelial growth factor receptor

Acknowledgement

I would like to express my deep gratitude to my mentors Professor Christos Boutopoulos and Professor Bruno Larrivée for their invaluable supervision and guidance. It was impossible to make it through this study without their continuous effective support.

I am grateful to Dr. Erika Hooker and Dr. Hamid Ebrahimi Orimi for patiently assisting and supporting me throughout my research experiments and to Dr. Mikhail Sergeev for his extremely helpful microscopy training.

I also wish to pay my special regards to Jennyfer Zapata-Farfan, Malcolm Latorre, Nicolas Desjardins-Lecavalier, and Kevin Lanthier for their priceless help and enlightening suggestions during this project.

This work would not be possible without the warm support of my family and friends. I would like to thank them deeply for their constant encouragement and emotional support throughout these years.

Chapter 1

Introduction

Fabrication of functional body tissues in laboratory settings that can be used in drug screening and organ transplantation is an essential goal of tissue engineering and regenerative medicine. The poor representation of human physiology by the current commonly-used drug screening tools has led to several clinical trial disasters (Attarwala, 2010; Moore, 2016; Manning et al., 1995). Exploiting the physiological properties of biofabricated tissues in drug screening would get us one step closer to the gradual discontinuation of animal sacrifice in drug screening that raises a lot of ethical concerns, aids in saving time and financial resources, and brings about more accurate drug testing results (Zhang et al., 2018). Furthermore, considering the shortage of available donors, tissue constructs can potentially aid in keeping pace with the demands for organ transplantation and repairing the injured tissues of patients (Da Silva and Frontera, 2015). Previously, simple avascular and thin tissues such as skin (Compton et al., 1998), bladder (Atala et al., 2006), cartilage (Vunjak-Novakovic et al., 1998), and trachea (Jungebluth et al., 2011) have been fabricated however bioartificial tissues would not survive for long if their thickness exceeds the diffusion limit of oxygen which depends on the tissue type but is generally considered to be about 200 µm (Jain, 1999; MacDougall and McCabe, 1967). On the other hand, it is now well-known that simple two-dimensional (2D) tissue models do not mimic the behavior and phenotype of the cells in vivo (Fitzgerald et al., 2015; Abbott, 2003).

For the fabricated tissues to survive and mature, a medium of nutrient and waste transportation to or from the cells is required to prevent necrosis. Previously, a number of methods such as flow perfusion bioreactors (Bancroft et al., 2003) or oxygen-producing polymers (Harrison et al., 2007) have been used to fulfill this purpose but proper vascularization of the tissues (Polykandriotis et al., 2006) is the leading approach due to multiple reasons. Among such reasons, there are the self-regulating potential of endothelial cells (ECs) for angiogenesis in hypoxic areas of the tissue (Tufro-McReddie et al., 1997), the dependence of tissues on their interactions with vasculature for maturation and functioning (e.g. kidney (Satchell and Braet, 2009), liver (Lammert et al., 2003), and pancreas (Lammert et al., 2001)), and improved anastomosis of the implanted vascularized tissues with the native blood vessels (Chen et al., 2009). Reliance on hypoxia-induced vasculogenesis in the implanted tissue by the host body is feasible to a certain degree to achieve vascularization, however, it has been shown that this process is rather slow and cannot keep up with the oxygen demands of the cells and will lead to necrosis of the core parts of the tissue soon after implantation (Rouwkema et al., 2008; Grellier et al., 2009). Therefore, in order to maintain the viability of the implanted tissue, a number of vascularization methods have been investigated including the use of angiogenesis-inducing scaffolds (Zhang et al., 2015; Tamplenizza et al., 2015), incorporation of growth factors and signals that promote angiogenesis in the matrix (Borselli et al., 2007), and pre-vascularization of the engineered tissue construct before implantation (Yu et al., 2009; Black et al., 1998; Rouwkema et al., 2009; Wang et al., 2010).

To generate pre-vascularized tissues, ECs need to be incorporated into the tissue construct to form blood vessels and support the tissue following implantation. It has been shown that ECs can develop functional capillaries that anastomose to the host's circulatory system and perfuse the graft (Alajati et al., 2008; Ben-Shaul et al., 2019; Roux et al., 2018; Steffens et al., 2009). Several approaches can be used in the pre-vascularization of bio-fabricated tissues. The simplest way to achieve vascularization is by exploiting the self-assembly potential of ECs by seeding the cells in a hydrogel matrix and allowing them to form a vascular bed on their own (Lee et al., 2014; Salameh et al., 2021; Mori et al., 2017). The issue with this approach is

that the self-assembled network is isotropic and uniform in vessel size (Guidolin et al., 2009; Serini et al., 2003) and we have no control over the vascular pattern. However, in physiological tissues, the native vasculature is self-similar and anisotropic to enable directionality of the blood flow to and from the heart (McDonald and Choyke, 2003). Another way to achieve hollow vascular channels is through the use of sacrificial or fugitive ink. Fugitive ink refers to a temporary support material for the main scaffold that could be removed subsequently to produce hollow structures (Prendergast et al., 2017). The material removal mode depends on the properties of the fugitive ink. We could simply pull out the fibers manually (e.g. agarose (Bertassoni et al., 2014) and nylon wires (Salameh et al., 2021)) or it could be dissolved by water (e.g. carbohydrate glass (Miller et al., 2012)), degraded by enzymes (e.g. alginate (Campbell et al., 2018)) or liquefied through reversible thermosensitive gelation (e.g. gelatin (Lee et al., 2014, 2010) and Pluronic F-127 (Kolesky et al., 2014; Zheng et al., 2021; Wu et al., 2011)). Following the fugitive ink removal, ECs could be seeded inside the hollow channels to form the inner wall of blood vessels allowing the tissue to be perfused with a medium. Nevertheless, creations of hollow structures with complex geometry or small dimensions and inadequate precision and accuracy for the generation of micro-capillaries are among the limitations associated with this technique (Grebenyuk and Ranga, 2019).

Since tissues have a microscopic level of complexity with small capillaries being present in close proximity (< 200 µm) of all component cells, there's the need for a biofabrication method that allows the fabrication of tissues with high microscopic resolution. Bioprinting allows the precise generation of complex patterns in three-dimensional (3D) space. Using computer-aided design (CAD), it is possible to have various patterns of biological constructs as input to the bioprinting system. In the following section, we have provided an overview of common bioprinting techniques including the laser-based technique that is the main focus of this study.

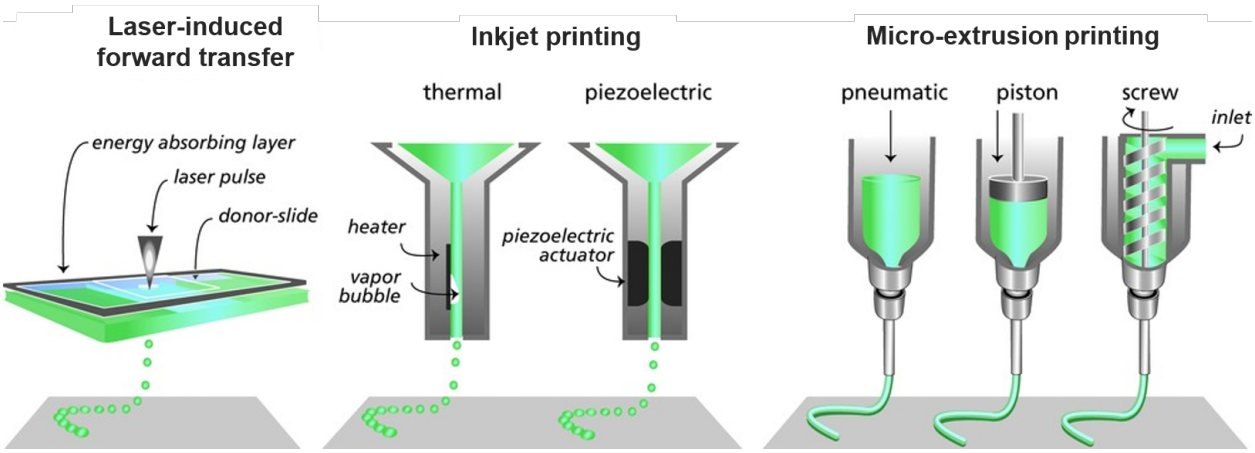

Fig. 1.1. The most common bioprinting techniques (Malda et al., 2013).

1.1. Bioprinting

Bioprinting can be defined as the precise spatially patterned deposition of cells and biomaterials and with regard to this definition, any material that is printed through such technologies is called bioink. Bioprinting techniques can be classified into three categories: extrusion-based bioprinting (EBB), inkjet bioprinting, and laser-based bioprinting (LBB) (figure 1.1). Among the mentioned bioprinter types, the latter two could be drop-on-demand (DOD) techniques meaning that the droplets of bioink are generated only when required which leads to higher accuracy and control over the printing process.

1.1.1. Extrusion-based bioprinting

EBB which is a widely-used technique employs a fluid dispensing system that extrudes continuous filaments of material through pneumatic, mechanical or electromagnetic force. Pneumatic dispensing systems use compressed air as the driving force to extrude materials through the nozzle. Mechanical systems can be pistol- or screw-driven. Dispensing systems that extrude material by electromagnetic force use electric pulses that pass through solenoids (Ozbolat and Hospodiuk, 2016).

Printing materials with a wide range of fluid properties is feasible using extrusion-based bioprinters. Materials with viscosities ranging from 30 mPa/s to more than $6x10^7$ have been printed in the past using this technique (Murphy and Atala, 2014) but due to the

high shear stress that the cells are exposed to, in this technique, the viability rates are usually lower than other major bioprinting techniques and ranges from 40% to 86% (Smith et al., 2004; Chang et al., 2008). Small nozzle diameters and high dispensing pressures are among the factors that affect the viability rate negatively. On the other hand, large nozzle diameters sacrifice the printing resolution. However, larger nozzles can cover a wider range of viscosities and hence, cell densities. Therefore, high cell densities can be printed via EBB with low resolution to fabricate larger blood vessels (Kolesky et al., 2016).

1.1.2. Inkjet bioprinting

Inkjet printing is a technique that allows us to print materials in a continuous or non-continuous manner. In continuous inkjet printing, there is a continuous generation of droplets but the droplets that are not printed end up in a recovery loop to avoid material waste (Sweet, 1965). For the purpose of bioprinting, only non-continuous inkjet printing has been used previously and this is due to the complexity and high probability of contamination during ink circulation in continuous inkjet printing.

Inkjet bioprinters print cells and biological materials in a non-continuous manner by employing several types of actuators. Using thermal, piezoelectric, electrostatic, or electro-hydrodynamic actuators (figure 1.2), a pressure pulse is generated and if the pulse surpasses the droplet ejection threshold, droplets are produced. Thermal inkjet uses a heating element for a few microseconds in the bioink that produces droplets by bubble formation (Cui et al., 2012). The heating plate temperature rises to about 300°C however, the bulk temperature increase stays in the 4°C to 10°C range (Calvert, 2001). Piezoelectric inkjet uses a material in the chamber wall that deforms in response to electric pulses and pushes the bioink out of the nozzle (Wijshoff, 2010). Similar to the piezoelectric actuators that work on the basis of chamber wall deformation, electrostatic inkjet uses a chamber wall called the pressure plate and in the presence of an electric field that is generated by an electrode plate, the pressure plate is pulled outward and increases chamber volume. The extra volume in the chamber is loaded with bioink and when the electric field turns off, the wall returns to its previous

position and the extra volume of the bioink will be pushed out of the nozzle as a droplet (Nakamura et al., 2005). Finally, electrohydrodynamic inkjet that is a non-DOD technique uses a metal-coated nozzle and the substrate as electrodes, and using an electric field, bioink is forced to come out of the nozzle as single droplets (Park et al., 2007).

Among the mentioned types of inkjet bioprinters, thermal, piezoelectric, and electrostatic inkjet are DOD techniques that have advantages in terms of printing accuracy over electrohydrodynamic inkjet bioprinting. Depending on the type of the inkjet bioprinter, cell survival rates could differ but generally, cell viability is higher than in EBB and is about 85% or more. One of the major drawbacks associated with inkjet printing is that we're limited to materials with a small range of low viscosities from about 3.5 to 12 mPa.s and since increasing cell density lowers the tendency of cell suspensions to flow (Wahlberg et al., 2018), printing cell concentrations higher than $1x10^6$ cells/mL is complicated in inkjet bioprinting (Li et al., 2020). Although not common, print heads have been made that are able to handle viscosities up to about 100 mPa.s (Calvert, 2001).

1.1.3. Laser-based bioprinting

Bioprinters that utilize laser energy as the driving force for droplet deposition are generally based on the laser-induced forward transfer (LIFT) technique. Although it is relatively new and was used only in 2001 for cell bioprinting purposes (Wu et al., 2001), there is a rapidly growing interest in this technique.

In LIFT, a pulsed laser beam is focused on a thin layer of bioink that is coated on the donor substrate (usually glass) which is transparent at the wavelength of the laser (figure 1.3). When the laser hits the bioink, it causes local evaporation or plasma formation (Xiong et al., 2015) in the bioink and the generation of a bubble. The expanding bubble causes the bioink jet formation at the liquid-air interface and finally if the laser energy is higher than the droplet ejection threshold, a droplet is generated and lands on the receiver substrate that is facing the donor substrate (Serra and Piqué, 2019). On the donor substrate, an energy-absorbing layer (e.g. gold or titanium) could be incorporated between the glass and the

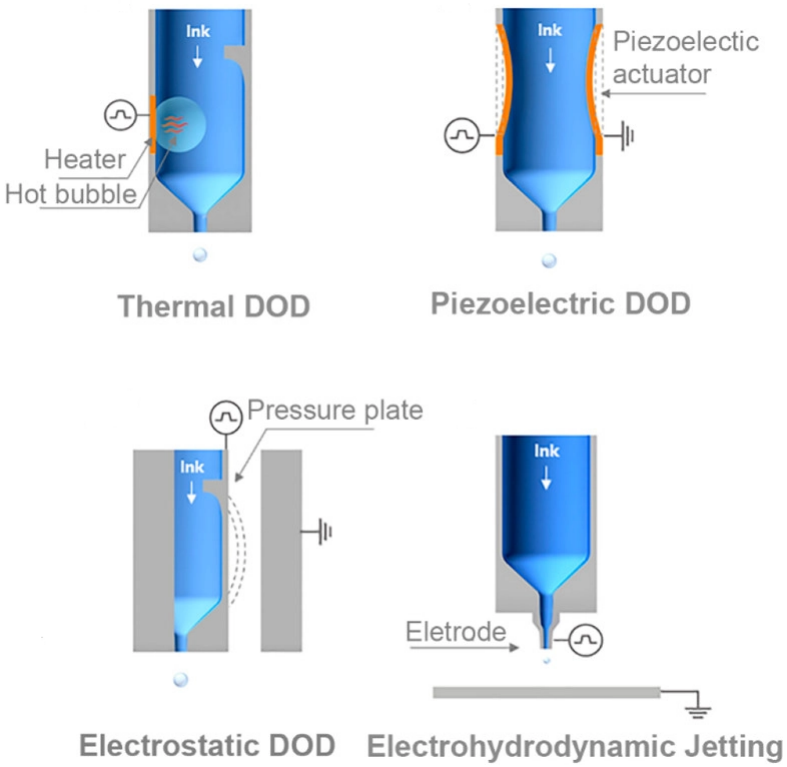

Fig. 1.2. Schematic representation of different types of inkjet bioprinting techniques used for bioprinting. Among the shown types, thermal, piezoelectric, and electrostatic inkjet printers are DOD (Li et al., 2020).

bioink film to increase the absorption of laser energy. It should be noted that the underlying mechanism of bubble or jet formation is not fully understood yet (Unger et al., 2011) however, a lot of studies have been done to visualize the process via high-speed cameras (Dou et al., 2021).

Several parameters play a role in the resolution of the printed patterns such as laser energy, the thickness of the bioink film, fluid properties of the bioink, the gap between the donor and the receiver substrates, and surface properties of the receiver substrate (Guillemot et al., 2010). The resolution of laser-based bioprinters is generally higher than other bioprinting techniques but it comes at the price of sacrificing the printing speed and scale-up capability. Thus, contrary to inkjet and especially extrusion-based bioprinters, simultaneous printing of both scaffold and the cells is not efficient. Therefore, LBB is usually considered to be a 2D printing technique. Nonetheless, in order to fabricate 3D tissue constructs a number

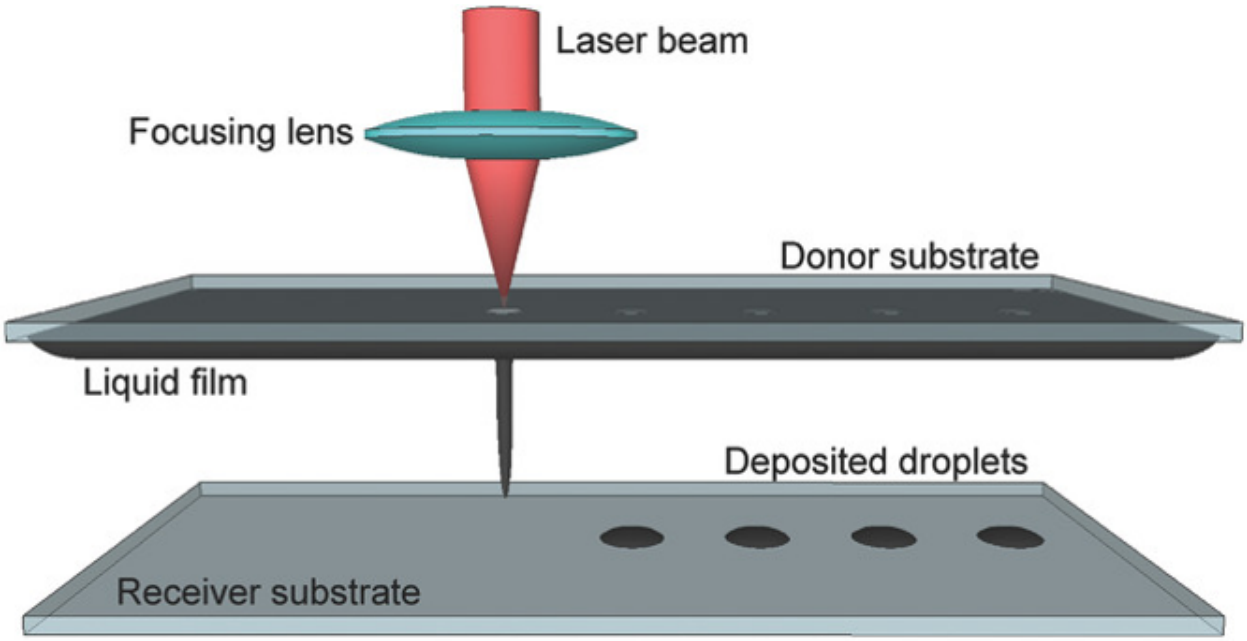

Fig. 1.3. Schematic diagram showcasing the working principle of LIFT LBB technique (Serra and Piqué, 2019).

of strategies have been employed such as multi-step sequential 2D cell printing and manual hydrogel matrix deposition (Gruene et al., 2011; Kérourédan et al., 2019; Koch et al., 2021; Barron et al., 2004), use of foremade 3D scaffolds as the receiver substrate (Ovsianikov et al., 2010), or cell printing on thin layers of stackable substrates followed by scaffold assembly (Pirlo et al., 2012).

This printing technique is nozzle-free so the cell clogging issue that might be present with EBB or inkjet bioprinting does not happen with LBB. As a result of the absence of the nozzle, the shear stress at the orifice that contributes to lower cell viability rates in other bioprinting techniques (Cui et al., 2010; Chang et al., 2008) is not present. Furthermore, being a nozzle-free technique leads to the compatibility of this method with high viscosities compared to inkjet bioprinters. This technique can print a wide variety of materials with viscosities up to about 1 Pa.s (Lin et al., 2009). As a result, high cell densities up to $100x10^6$ that are unfeasible to print with inkjet printers have been previously printed with LIFT (Guillotin et al., 2010; Koch et al., 2021). Cells can be printed at high cell densities while maintaining high viability rates and functionality, exhibiting the biocompatibility and potentials of this technique for biofabrication (JA, 2004; Lin et al., 2010).

1.2. Cell types

The blood vessels in our body have a great diversity with various sizes and cell compositions (figure 1.4). From the aorta which is the largest artery in our body to the capillaries, the diameter of blood vessels ranges from about 3cm to less than 10 µm (Fleischer et al., 2020). Blood vessels in the native tissue are composed of three layers called tunica intima, tunica media, and tunica adventitia (also known as tunica external) from the innermost to the outermost layer. Tunica intima is basically a monolayer of ECs (also known as the endothelium) that lines the inner surface of all blood vessels in the entire vascular network and through which nutrients, cellular waste, or signaling molecules get exchanged between the tissue cells and blood. The middle layer or tunica media is the place for the mural or perivascular cells that perform several roles including regulation of the blood pressure, provision of structural support to the vessels, regulation of material exchange with body tissues, and stabilization of ECs and preventing them from uncontrollable proliferation (Stratman et al., 2017; Lin et al., 2021). This middle layer has a varying cell composition throughout the vascular system; In large vessels, smooth muscle cells (SMCs) surround the endothelium through layers with variable thickness according to the vessel size. Mainly functioning as the exchange site between the blood and the tissue cells, capillaries are lined with a non-continuous layer of pericytes (PCs) instead of SMCs. Finally, tunica adventitia is a supporting connective tissue in which the main cell component is fibroblasts whose primary role is to synthesize the ECM. In addition to fibroblasts, several other cell types including immune cells and progenitor cells reside in this outer layer (Mazurek et al., 2017) but, will not be discussed further here.

1.2.1. Endothelial cells

The main cell type in the structure of the vasculature is ECs. Depending on the source of ECs, they can show different characteristics so it's important to use suitable EC types tailored to our application.

The most common source of ECs in the pre-vascularization of tissue constructs is HUVEC which is extracted from the veins in the umbilical cord of the newborn. This cell

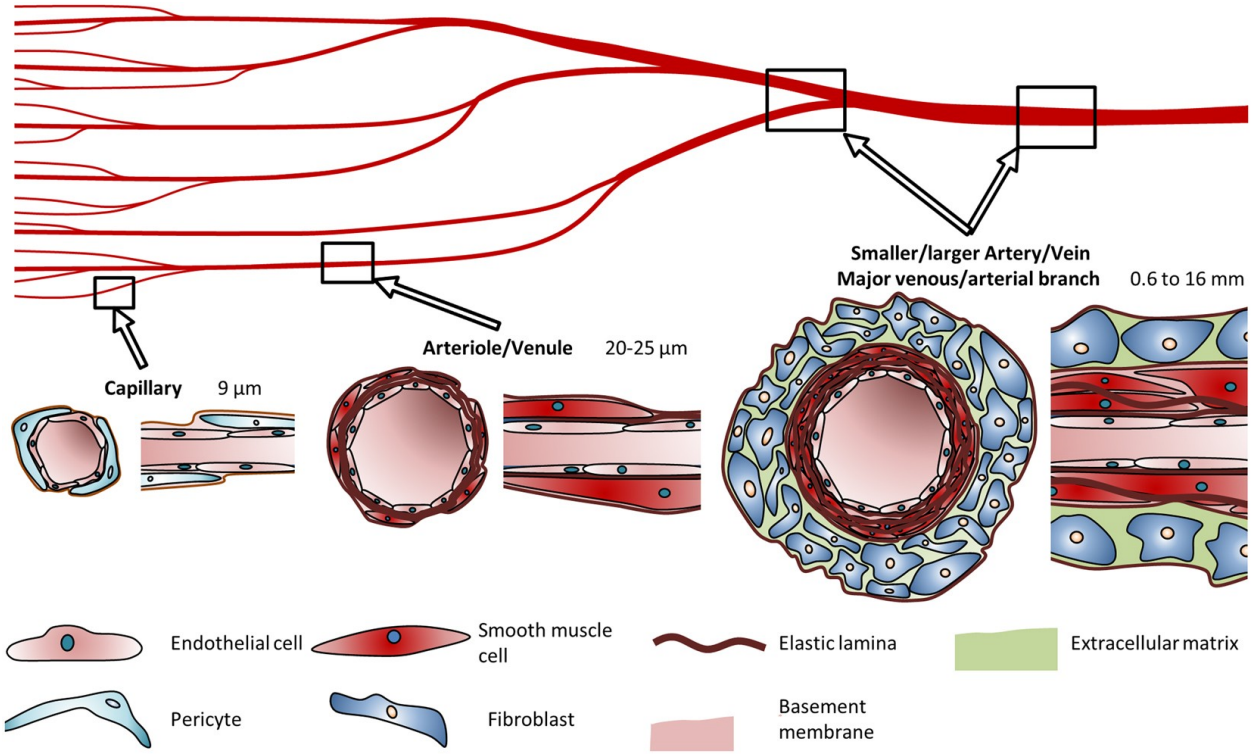

Fig. 1.4. The cellular composition of blood vessels in the native tissue from capillaries smaller than 10 µm to large arteries and veins in 1 cm size order (Schöneberg et al., 2018).

type is widely available and inexpensive as it's derived from donated human umbilical cords, otherwise being discarded as medical waste. HUVECs are derived from the big veins in the umbilical cord and are, therefore, more suitable for the biofabrication of larger vessels. Another important cell type is human microvascular endothelial cell (HMVEC) which is extracted from the microvasculature of various tissues and as a result, has greater potential for biofabrication of microvessels. Another interesting EC source that has not been investigated much is induced pluripotent stem cell-derived endothelial cells (iPSC-ECs). By following the groundbreaking protocol published by Takahashi et al. (2007), it is possible to induce pluripotency on differentiated cells and dedifferentiate them to obtain stem cells. These stem cells can later be differentiated into ECs, giving us an opportunity to fabricate patient-specific vascularized tissue constructs with cells extracted from the patient's own body. This would facilitate organ transplantation by lowering the chance of implant rejection by the immune response and improve the predictability of drug screening tools for each patient (Barrs et al., 2020).

1.2.2. Supporting cells

Through contraction and relaxation of the contractile protein filaments in their cytoskeleton, SMCs regulate the blood flow inside the vessels. Arteries have a thick lining of SMCs tailored to regulate high-pressure blood. The blood pressure plummets as the arteries branch into arterioles with fewer SMC layers. Veins and venules have thinner tunica media (fewer SMC layers) compared to the arteries and arterioles of the same size. Controlled by the multiple layers of SMCs, the blood pressure reduces from arteries to veins (Mazurek et al., 2017).

In capillaries, PCs take the place of SMCs as perivascular cells and reside mostly in the cell-cell junctions or the branching points of the endothelium to stabilize and mature the ECs (Ando et al., 2016). Healthy PC coverage in capillaries depends on the distinct role of the vasculature in that particular tissue and capillaries that lack enough population of PCs would consequently be leaky and unstable (Winkler et al., 2011). PCs are mural cells that have a varying abundance depending on the position of the capillary bed; the ratio of ECs to PCs ranges from 1:10 to 1:1 (Stratman et al., 2017). The highest population of PCs in the human body is found in the central nervous system (Armulik et al., 2011) where they perform the role of maintenance and development of the blood-brain barrier (Yamazaki and Mukouyama, 2018).

Fibroblasts are the primary cell type in the outermost layer of vasculature and perform several important roles such as secretion of collagen and other ECM proteins and contribution to the wound healing process following tissue damage (Di Carlo et al., 2018).

Owing to the fact that in the native tissue vascular networks are not only made up of ECs, incorporation of other cell types is crucial for the generation of stable and functional blood vessels. Accordingly, supporting cell types like fibroblasts (Koch et al., 2021), PCs (Darland et al., 2003), SMCs (Korff et al., 2001; Wu and Ringeisen, 2010), and stem cells (particularly in bone tissue) (Koob et al., 2011; Au et al., 2008; Unger et al., 2007; Güven et al., 2011; Aguirre et al., 2010) have been included in the tissue constructs in the past research.

1.3. Angiogenesis

Angiogenesis is the expansion of a pre-existing vascular network. This is not to be confused with vasculogenesis which is *de novo* formation of blood vessels directly from angioblast precursors (Swift and Weinstein, 2009). Angiogenesis can be divided into intussusceptive angiogenesis (splitting) (Caduff et al., 1986) and sprouting angiogenesis. Here we focus on the underlying mechanism of sprouting angiogenesis.

The cells need oxygen to survive and in case of hypoxia where there are low levels of oxygen, the cells start secreting pro-angiogenic molecules to signal the capillaries surrounding the hypoxic tissue. The main pro-angiogenic growth factor that plays a crucial role in angiogenesis is vascular endothelial growth factor (VEGF)-A (Gerhardt et al., 2003). The ECs in the surrounding capillary network that receive the highest dose of VEGF-A turn into tip cells characterized by extending structures called filopodia. These filopodia protrude toward the angiogenic center by following the VEGF-A gradient and breaking down the basement membrane and the ECM using proteolytic enzymes. As the tip cell protrudes towards the angiogenic center, the adjacent ECs to the tip cell, also known as the stalk cells, proliferate to support the sprout elongation. This would allow the tip cell to migrate further toward the hypoxic tissue. When blood flows through the newly formed sprouts, the hypoxic tissue cells start receiving more amount of oxygen and gradually slow down the release of pro-angiogenic factors (Jakobsson et al., 2010). Afterward, perivascular cells will cover the newly formed endothelium to induce quiescence and stabilization (figure 1.5).

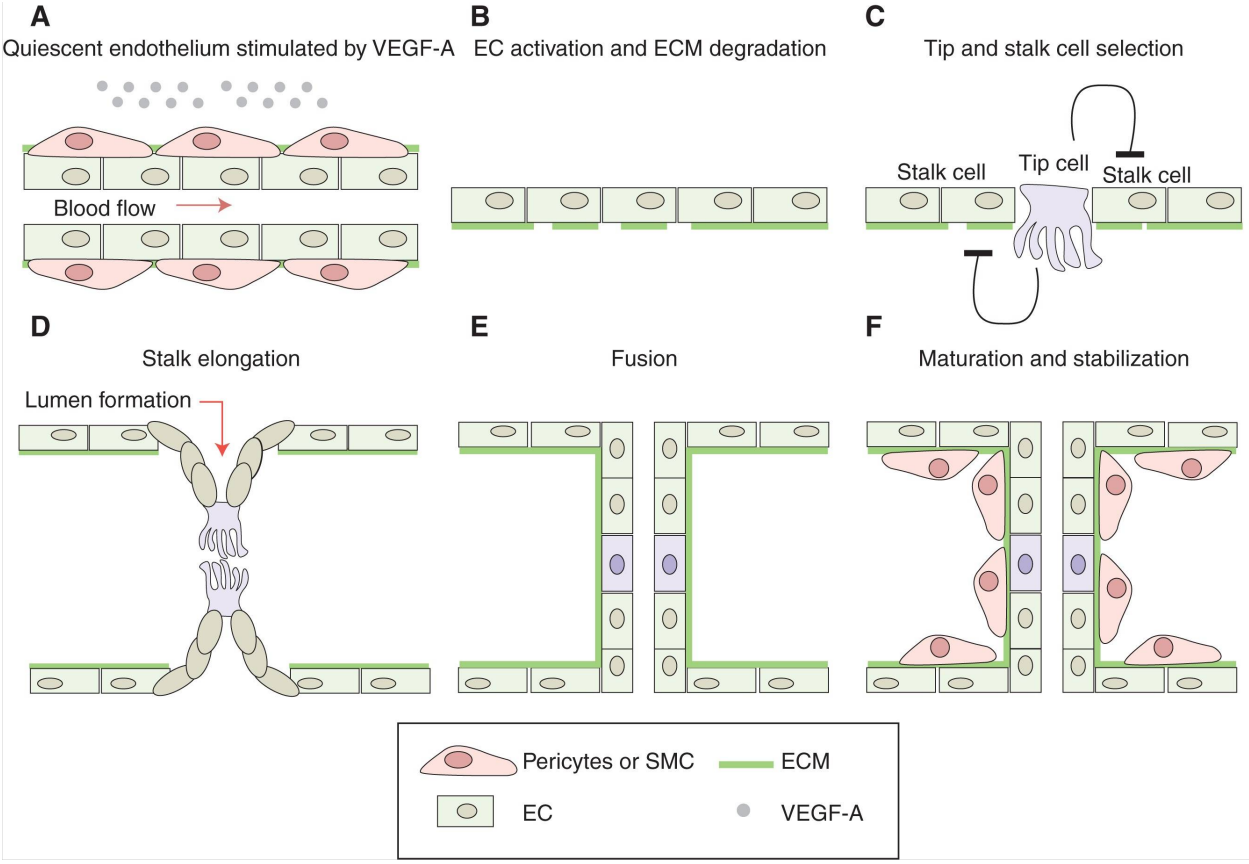

Fig. 1.5. Schematic diagram showing the steps of sprouting angiogenesis (Blanco and Gerhardt, 2013).

1.4. ECM-mimicking hydrogels

Hydrogels play the role of the ECM in laboratory settings and serve as a bed on which the printed cells attach, communicate, proliferate, and migrate. The majority of the hydrogels that have been used in bioprinting are extracted enzymatically from natural mammalian or non-mammalian sources due to biocompatibility and in some cases, angiogenesis-promoting nature. Synthetic hydrogels are produced chemically and their characteristics can be precisely controlled through chemical modifications of their building blocks (monomers). Since they're synthesized under controlled conditions, batch-to-batch consistency is one of their marked advantages over naturally-derived hydrogels but they suffer from low biocompatibility which would affect cell behavior. A number of common hydrogels in bioprinting are listed in table 1.1 among which only Pluronic F-127 is a synthetic polymer.

Benning et al. (2018) conducted a comprehensive study on the effect of the hydrogel substrates mentioned in table 1.1 on HUVEC spheroid behavior. These compounds need to be printed in their liquid state so the gelation method of the hydrogel matrix affects the complexity of the printing process. Hydrogels with the chemical gelation method can be adapted to bioprinting settings by sequential printing of reagents or printing of one reagent on the other on a substrate. However, printing thermosensitive biomaterials is technically more complicated; Matrigel must be kept below 10°C and agarose and gelatin must be kept above 37°C to prevent gelation so the temperature at the print head must be continuously monitored and adjusted with temperature control equipment to maintain the biomaterial at liquid state during the printing step.

Physical properties of the materials in the liquid state (as bioink) and their viscoelastic properties after gelation (as substrate) were assessed and then HUVEC spheroids were printed on hydrogels to evaluate cell viability, proliferation, and vasculogenesis. Based on the surface tension measurements, all the tested materials are easily printable since they have a higher surface tension than the minimum requirement for inkjet bioprinters (35 mN/m) (Calvert, 2001). Except for gelatin, Pluronic F-127, and thrombin which showed characteristics of Newtonian fluids, all the other materials were non-Newtonian and showed shear-thinning behavior. Moreover, except agarose, all the other materials were in the range of printable viscosities by inkjet printers. Regarding the viscoelastic properties, the materials preferably need to have a high storage modulus to withstand the conditions for implantation. Among the tested hydrogels, collagen had the lowest storage modulus values between 2 to 33 Pa for 1 to 3 mg/mL concentrations.

In their cell studies, the viability of HUVECs after 24 hours on the hydrogels was assessed and it was shown that alginate, due to a low viability rate of only 71%, and Pluronic F-127 and agarose, due to low cell attachment are not suitable candidates to mimic the role of the ECM. In cell proliferation assessment, the population of the HUVECs increased up to 7 to 8 times after 7 days on fibrin, Matrigel, collagen, and gelatin, and interestingly, cell proliferation had an inverse correlation with hydrogel concentration in the case of Matrigel,

collagen, and gelatin. On the other hand, HUVECs did not proliferate on Pluronic F-127, agarose and alginate; so these hydrogels showed desirable results neither in cell viability and attachment nor in cell proliferation experiments so they were not assessed in their cell studies any further. In the cell sprouting experiments, HUVEC spheroids were seeded on the remaining group of hydrogels and it was observed that only gelatin could not support endothelial sprouting while fibrin, Matrigel, and collagen showed favorable results (figure 1.6). Therefore, these three hydrogels were found to be suitable substitutes for the ECM; however, Matrigel needs to be kept below 10°C to be printable which makes the process difficult but in the presence of temperature-controlling equipment, Matrigel is also a favorable choice due to promotion of cord formation in ECs (Kuzuya and Kinsella, 1994).

Hydrogel	Gelation Mode	Gelation Time	Benefits	Limitations
Matrigel	thermal: above 10°C (irreversible)	30 mins	high biological activity	long gelation time, poor mechanical properties, undesirable source
Fibrin	chemical: thrombin (irreversible)	secs	high biological activity, fast gelation	fast degradation, poor mechanical properties
Collagen type I	thermal (reversible), chemical (irreversible)	30-60 mins	high biological activity	long gelation time, poor mechanical properties
Gelatin	thermal: below 37°C (reversible), chemical (irreversible)	mins	high cell attachment	must be modified to be printable
Alginate	chemical: divalent cations (reversible)	mins	similar structure to ECM	low cell attachment
Agarose	thermal: below 37°C (reversible)	mins	cytocompatible	low cell attachment, poor mechanical properties
Pluronic F-127	thermal (reversible)	mins	batch-to-batch consistency	low cell attachment, fast degradation

Table 1.1. A number of ECM-mimicking biomaterials that are commonly used in bioprinting applications. In this list, Pluronic F-127 is the only synthetic hydrogel (Benning et al., 2018; Prendergast et al., 2017).

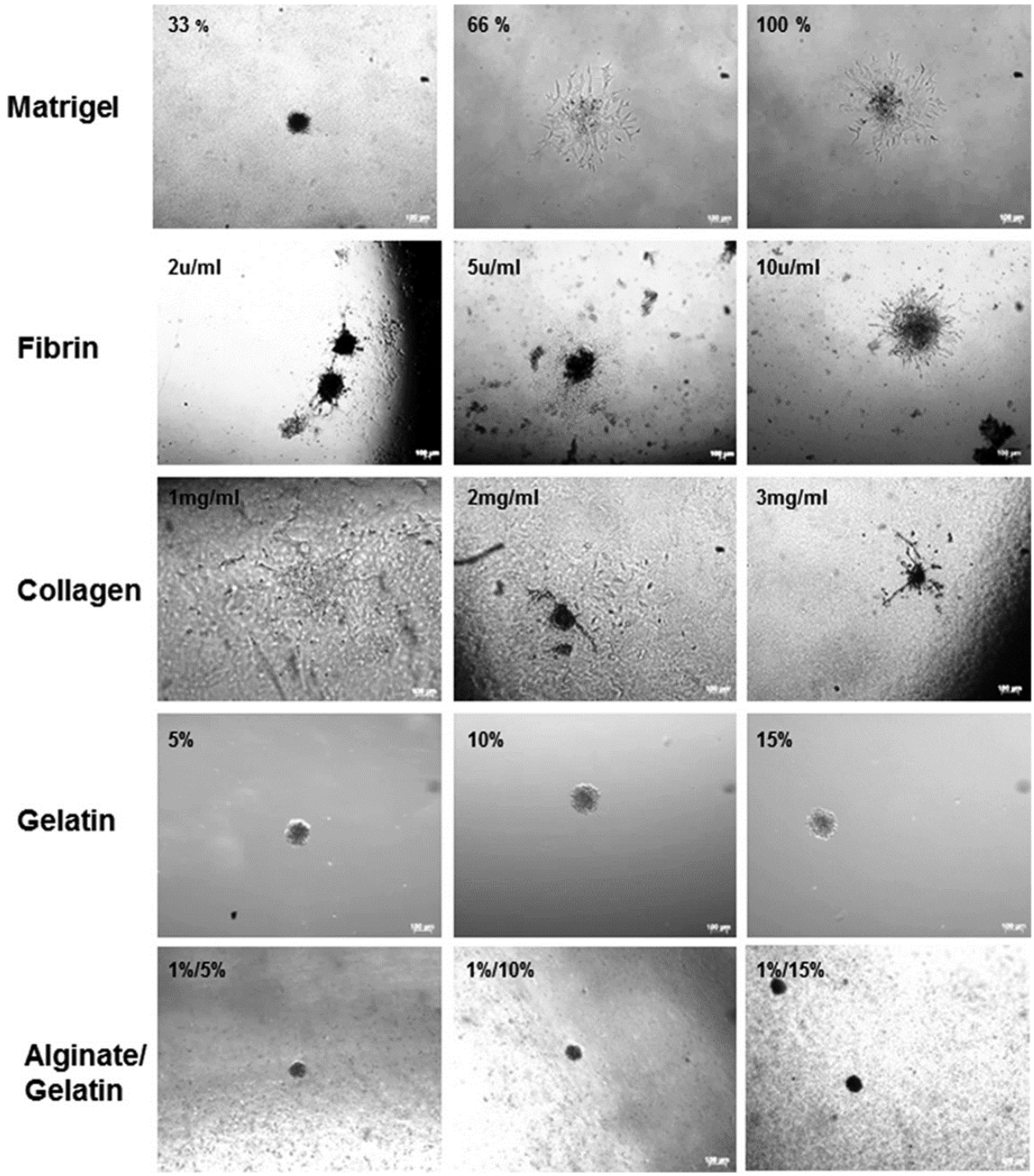

Fig. 1.6. Sprouting of manually-deposited HUVEC spheroids on a number of commonly-used hydrogels in biofabrication at varying concentrations. Phase contrast images were taken after 24 hours. Scale bars denote 100 µm length (Benning et al., 2018).

In a previous work of our lab, Orimi et al. (2022) manually deposited three hydrogel formulations on substrates that served as a bed for printing HUVECs. In figure 1.7, the HUVEC

printing outcome on fibrin, Matrigel, and Matrigel/thrombin is shown. The HUVEC-laden bioink was formulated with fibrinogen so in the case of fibrin and Matrigel/thrombin hydrogels, the droplets that land on the substrate quickly gel. On fibrin substrates, the printed HUVECs migrated to other areas of the gel and proliferated leading to gradual coverage of the whole surface of the gel. With Matrigel substrates, we see the cord-like formations that HUVECs normally form on this hydrogel however these structures start to disintegrate two days after printing. Interestingly, HUVECs that were printed on Matrigel/thrombin substrates stayed in place even on the second day post-printing and did not migrate to other areas. These ECs developed stable cord-like formations that adhered to the surface of the gel and did not disintegrate. Combined with bioprinting, Matrigel/thrombin substrates show great potential for the purpose of guided angiogenesis; in other words, we can control the direction of the capillary formation using these hydrogels and bioprinting technologies.

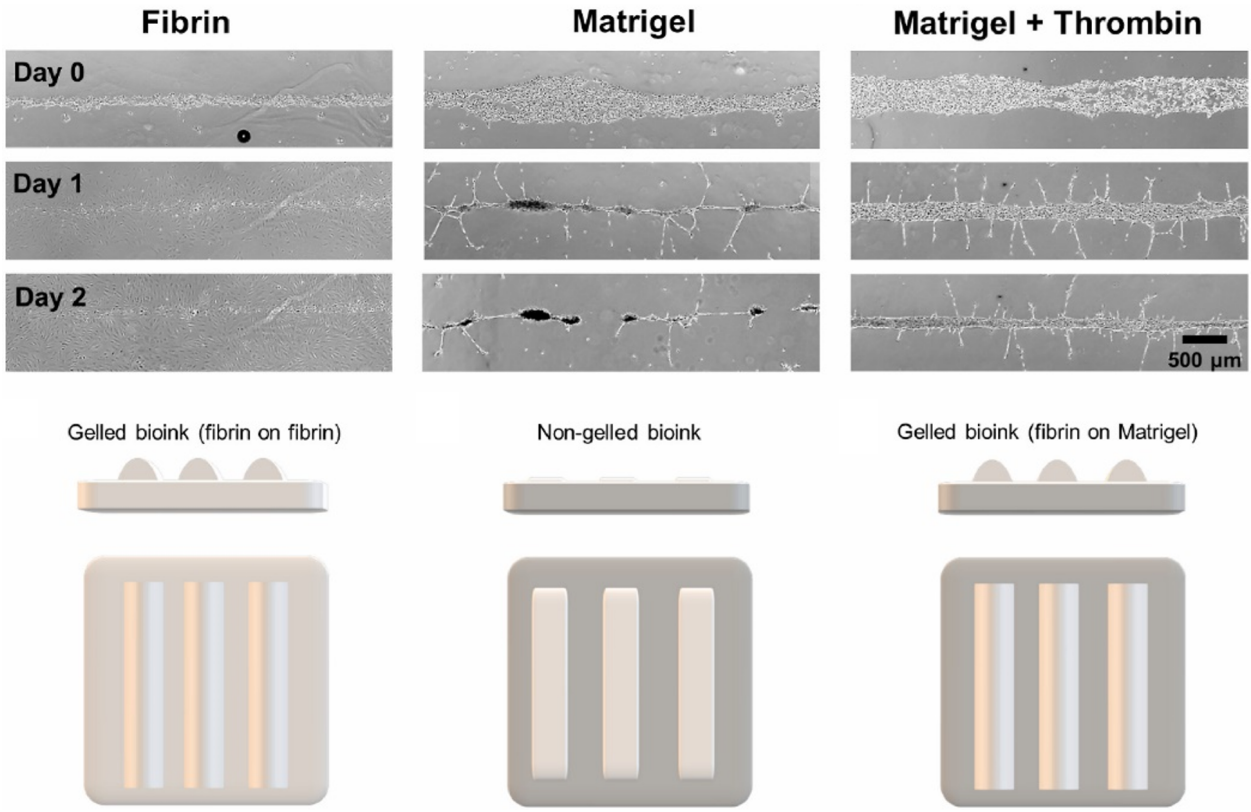

Fig. 1.7. The outcome of printing HUVEC-laden fibrinogen-containing bioink on fibrin, Matrigel, and Matrigel/thrombin hydrogels until day 2 post-printing. Fibrin hydrogels could not keep the initial printing pattern in place and HUVECs proliferated and migrated to other areas. Matrigel failed to keep the cord-like formations in place while the Matrigel/thrombin hydrogel showed strong adhesion properties and kept the HUVEC tubular structures in place. The bioink did not gel on Matrigel substrates due to the absence of thrombin.

1.5. Applications of DOD bioprinting in angiogenesis

In this section, we have provided a detailed review of the previous applications of DOD bioprinting methods in angiogenesis research. We will discuss the previous research works done with inkjet and laser-based bioprinters as well as hybrid bioprinting methods through which the advantages of more than one bioprinting technique are exploited.

1.5.1. In vitro studies

The first effort to print ECs using an inkjet bioprinting system was done in 2005 when Nakamura et al. (2005) used an inkjet bioprinter to seed bovine vascular ECs at a micrometer

resolution. They used an electrostatic actuator to prevent heat generation which they believed contributes to cell death. Printing of a cell suspension bioink in the cell density order of 1x10^6 cell/ml at 85 to 240 µm resolution was shown to be successful without significant mechanical cell damage for the first time.

When HMVEC suspension in thrombin was printed on a small layer of fibrinogen, fibrin channels were created where the droplets land. Simultaneous printing of ECs and fibrin scaffold led to the generation of tubular structures. ECs proliferated inside the fibrin microchannels and sealed them however, the inner part of the channels was not hollow and therefore not perfusable since it was filled with clusters of cells in fibrin (Cui and Boland, 2009).

In an effort to resemble the physiological 3D environment of the cells, instead of printing a cell suspension, Gutzweiler et al. (2017) printed HUVEC spheroids on fibrin substrates. Using a piezoelectric inkjet print head, they deposited an array of single spheroids with a distance of 500 µm between the adjacent droplets. They monitored the development of sprouts and vasculogenesis in the printed constructs for 7 days and observed that the neighboring HUVEC spheroids formed interconnections that continued growing for about 3 days post-printing. Afterward, no further sprouting or interconnection growth was seen so there was the need to support and stabilize the EC structures.

As described earlier, fibrin and collagen were among the hydrogel matrices that support vasculogenesis. Therefore, Tröndle et al. (2019) exploited the pro-angiogenic properties of these hydrogels to investigate cell behavior through various printing patterns made with cell suspension and spheroid bioinks. In order to quantify the sprouting behavior of the cells, they defined cumulative sprout length (CSL) as the sum of the length of every single sprout extending from each cell aggregate and averaging over the number of cell aggregates. They printed HUVEC suspension and spheroids separately on fibrin and measured CSL. The quantification showed that CSL is significantly higher for printed cell suspension compared to HUVEC spheroids over the first three days in culture. Furthermore, it was found that the neighboring droplets of the cell suspension bioink that are up to $d_{separate}$ = 750 µm apart

(design 1) develop straight interconnections toward each other that are not only morphologically distinct from the other branched sprouts extending in other directions but also have more than twice the CSL value which is shown in figure 1.8 as CSL(+). In another printing pattern (design 2), droplets were printed $d_{overlap} = 200$ µm apart which caused them to merge and form a continuous line of HUVEC suspension bioink droplets. The confocal images confirmed that this design led to lumen formation and branching sprouts that are connected to the lumen. The average cross-sectional area of the lumen and the sprouts was measured to be about 6400 μm^2 and 740 μm^2, respectively. Lumen formation was also confirmed by perfusion. It's worth mentioning that the number of dead round cells that were washed away in the inner space of these channels after perfusion was higher in collagen and this hydrogel did not support sprouting as much as fibrin. Lumen formation in these constructs shows a promising perspective for the fabrication of thick tissues by incorporating tissue-specific secondary cell type layers in between the EC layers with branched printed patterns. These customized constructs, therefore, have the potential to be used in regenerative medicine for implantation (figure 1.9).

Usually, bioprinting techniques generate heat in the bioink and cause heat stress to the cells through the use of thermal actuators, friction in the nozzles or the laser beam in the nozzle-free LIFT printers. In response to heat stress, the cells express a group of proteins called heat shock proteins (HSPs) (Lee et al., 2012) that can potentially induce angiogenesis (Ritossa, 1962). Solis et al. (2019) showed that compared to manually-pipetted HMVECs, the heat that is generated through thermal inkjet bioprinting of HMVECs causes a significant increase in expression of angiogenic factors such as VEGF-A, FGF-1, HSPs, and other factors that have proven to induce angiogenesis. In addition, thermal inkjet bioprinted HMVECs show 2 to 3 times more elongation and even significantly higher viability rates after three days in culture. Therefore, the heat shock that is imposed on ECs during bioprinting actually ends up being helpful to the cells shown by higher survival rates and production of vascular networks.

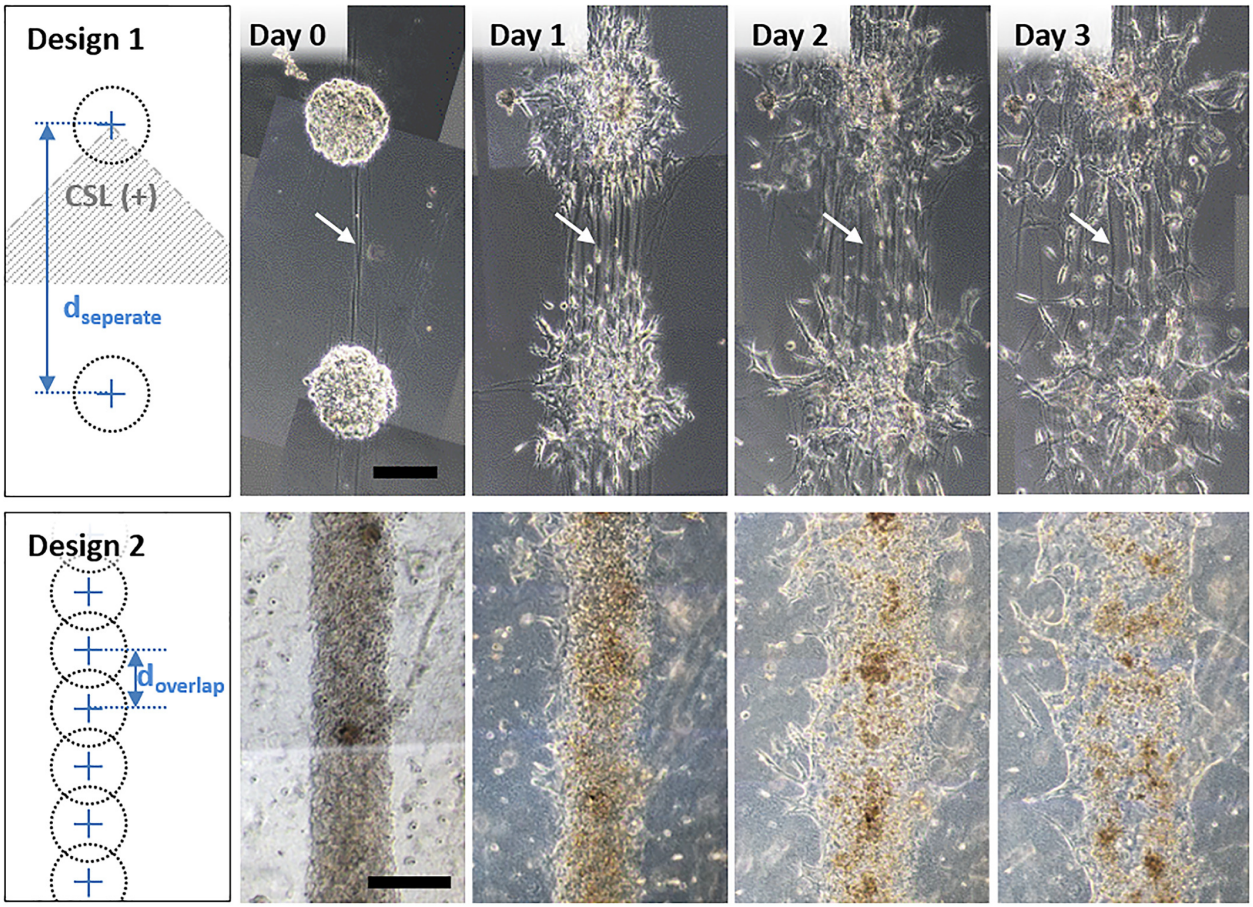

Fig. 1.8. Two different HUVEC printing designs that allow investigation of the pattern of EC sprouting direction (top row) and tubulogenesis and lumen formation (bottom row). White arrows show the sprouts that are directed toward the adjacent cell suspension droplets. Scale bars denote 250 µm length (Tröndle et al., 2019).

The first time that LBB was used to print ECs was in 2010 when Wu and Ringeisen (2010) tried to generate a pattern of HUVECs on Matrigel that was inspired by the self-similar vein network in leaves. HUVECs were printed successfully and formed self-assembled structures to which the group referred as lumen structures however the development of lumen was unclear and confirmed by neither imaging nor perfusion. This self-assembled network was formed one day after printing and developed sprouts that interestingly, were mostly perpendicular to the main HUVEC printed lines[1]. However, these structures gradually degraded after a few days and were not stable. Therefore, in order to stabilize and maintain the HUVEC structures for longer, they investigated co-culturing ECs with SMCs that are known to have a

[1]Printed line refers to the patterns of cells that form continuous structures following the bioprinting procedure. This should not to be confused with immortalized cell lines.

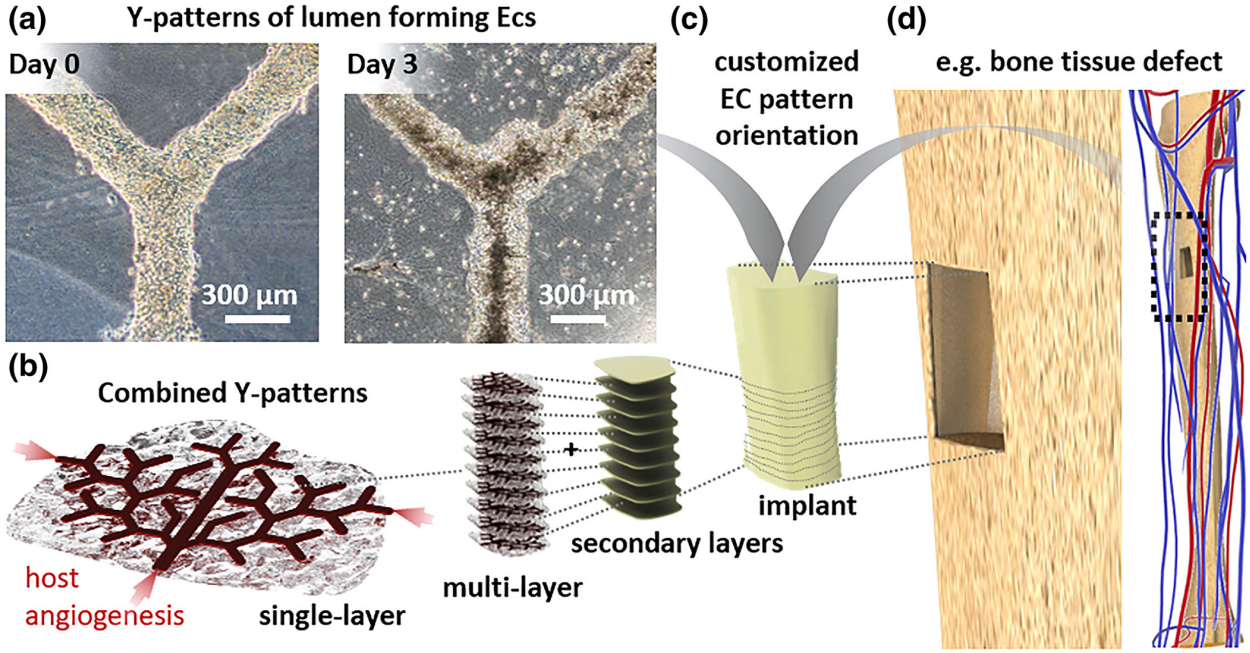

Fig. 1.9. The potential of lumen forming ECs for use in regenerative medicine. (a) Branched Y-shaped patterns of ECs could be printed (b) in several layers in combination with tissue-specific secondary cell types to (c) fabricate customized tissue constructs tailored to any particular tissue into which they will be (d) implanted (Tröndle et al., 2019).

symbiotic relationship in stabilizing and maturing each other. Human umbilical vein smooth muscle cells (HUVSMCs) were printed on top of the printed HUVECs after they formed their network on the first day and it was shown that the co-culture helped ECs to maintain the stability of the self-assembled structures after nine days (figure 1.10). Furthermore, HUVECs also aided in stabilizing HUVSMCs; printed HUVSMCs stayed in the contractile state on their own that caused them to disintegrate and aggregate into cell clusters while the co-culture with HUVECs changed their phenotype into the proliferative state characterized by the extended morphology. When seeded on the printed HUVEC samples, HUVSMCs that were in proximity of the printed ECs had the proliferative phenotype while the other SMCs that were far from the printed lines stayed contractile. Therefore, the importance of the incorporation of multiple cell types in vascular networks for the stability and functionality of ECs was shown.

As mentioned earlier, achieving 3D tissue constructs with LBB could be done through the manual deposition of the hydrogel in between the cell layers or the use of 3D scaffolds.

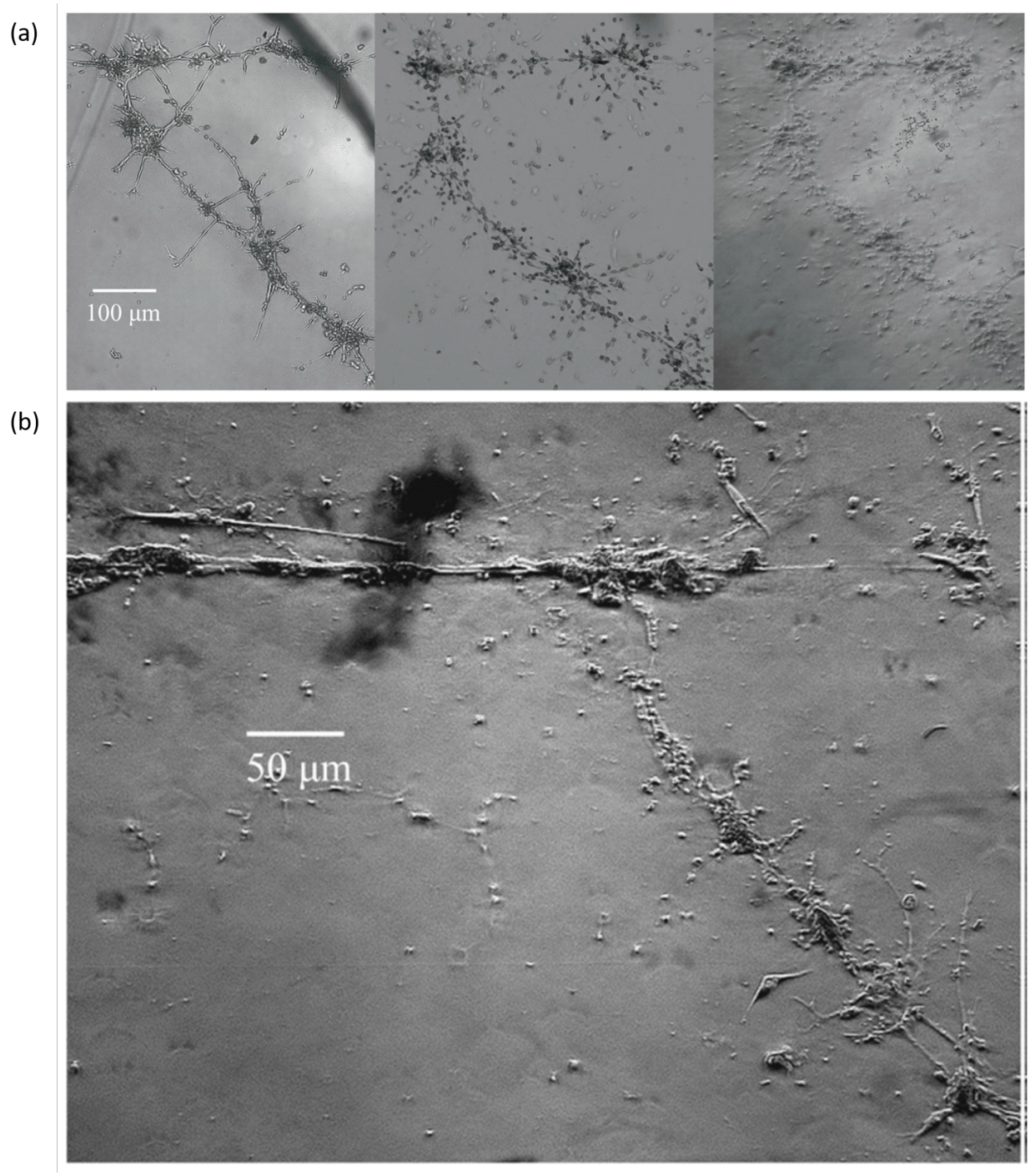

Fig. 1.10. (a) Self-assembled network of HUVECs after one day (left), 5 days (middle), and 13 days (right) and (b) co-culture of HUVECs and HUVSMCs nine days post-printing. The structure made by HUVECs in the co-culture has remained intact for longer. The cells were not stained so it is difficult to distinguish the two cell types (Wu and Ringeisen, 2010).

Inspired by these approaches, Pirlo et al. (2012) created thin 300 µm Poly(lactic-co-glycolic acid) (PLGA) layers that they referred to as "biopapers". These biopapers were stacked on top of each other after cell deposition to create a centimeter-scale 3D construct. HUVECs were printed in different patterns and coated with Matrigel to investigate cord formation by ECs. They investigated the effect of cell density by printing single- or triple-wide lines (that merged together) and observed that the triple-wide line pattern improved capillary network formation with cells that had a viability rate of 95%. Then they stacked four single biopapers on each other and cultured them for four days and noticed a reduction in the overall thickness of the engineered construct. It was not possible to separate the individual layers anymore which shows the merging of the single biopapers and the feasibility of their use in the fabrication of 3D tissue constructs.

LBB has been used to study the migration of ECs in the presence of supporting cell types. Bourget et al. (2016) assessed the tendency of HUVECs to migrate out of their initial patterned position on a printed line and the effect of human bone marrow mesenchymal stem cells (HBMSCs) on this process. First, they investigated the migration of each cell type separately and then their behavior in the co-culture was assessed. HUVECs that were printed in lines were seen outside of the initial droplet landing area after 24 hours and covered the surface of the collagen hydrogel while HBMSCs did not migrate out of their initial position in the same time slot. When cells were printed together in a 1:1 ratio, it was observed that HUVECs mostly stayed at their initial patterned location. It was deduced that HBMSCs have the ability to influence HUVECs to reduce their migration in the co-culture. Controlling the migration of ECs allows us to fabricate tissue constructs with any given pattern of the capillary network that does not disintegrate due to cell migration.

In a recent study, Koch et al. (2021) performed two EC printing experiments to investigate lumen formation by ECs. First, they printed human pulmonary microvascular endothelial cells (HPMECs) at a high cell density of 100×10^8 cells/mL on a 66% Matrigel hydrogel that was diluted by the culture medium. As a result of the lower stiffness of the gel substrate compared to pure Matrigel, their droplets penetrated the hydrogel and caused depressions

on the surface. After one day in culture, they observed the formation of tubular structures with actual lumina whose diameter ranged from about 10 to 60 µm (figure 1.11). However, after two days these structures disintegrated and the ECs moved from their initial position to other areas. This could be due to the low stiffness of the hydrogel matrix that facilitated cell migration compared to pure Matrigel. Furthermore, they changed the volume of the printed droplets by adjusting printing parameters such as laser energy and found that the structures that are printed with smaller droplets form thinner capillaries and larger droplets lead to thicker capillaries. However, printing with too small droplets leads to frequent interruptions (several non-continuous capillary segments) in the printed lines while too large droplets fail to generate tubular structures and rather produce gutters with unemployed cells ending up around and inside the open channel. So there's an optimization to be made in the printing droplet size to fabricate hollow non-fragmented capillaries. In their second experiment, they fabricated a skin construct through the printing of multiple cell types layer by layer. Using LIFT, they deposited a grid pattern of ECs sandwiched in the middle of 18 fibroblast layers that were covered with 9 additional layers of keratinocytes. This construct was imaged after three days and it seems that through the self-assembly of ECs and the growth factors expressed by the supporting cells, some tubular structures have formed. However, the majority of these structures seem to be filled with cells and have collapsed lumina which is not a characteristic of the physiological microvessels. It should also be noted that this group used an immortalized EC line to generate the hollow tubular structures in their first experiment while in the skin construct, HUVECs were the EC source and the developed lumina did not look as convincing. Therefore, the printing of a primary EC source might not lead to these tubular structures as much as a cell line without the aid of growth factors as was shown by our group in the case of HUVECs (Ebrahimi Orimi et al., 2020).

1.5.2. In vivo studies

One of the challenges of animal studies is the obligation to sacrifice the model to monitor the implanted tissue, especially if assessments are to be made at several time points during

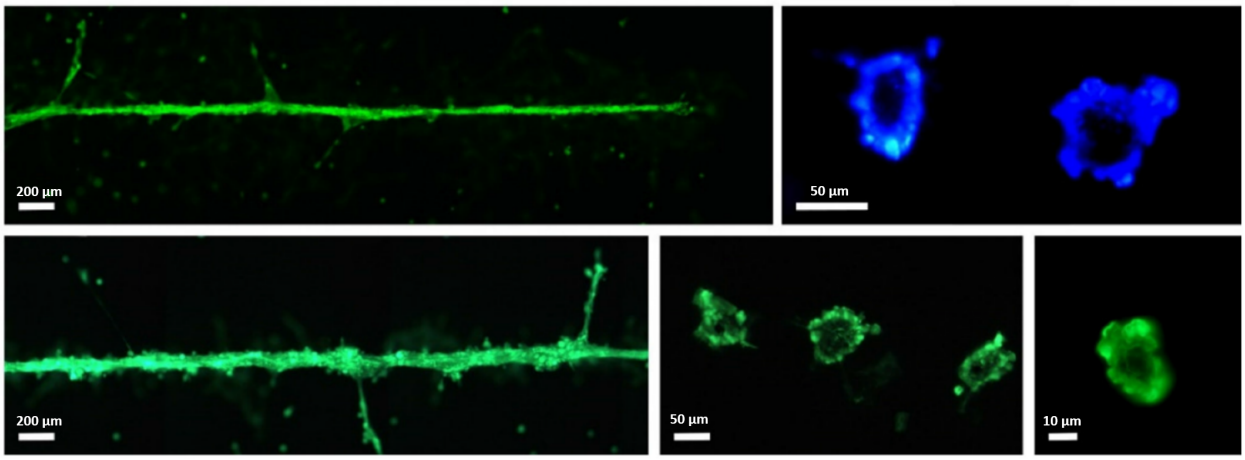

Fig. 1.11. The formation of tubular structures with lumina by LIFT printed HPMECs after 24 hours. The upper left image shows a thinner capillary printed by small droplets while the lower left image shows a large capillary printed by large droplets. The Z-stack images on the right show lumina with diameters of 15 and 50 µm. HPMECs were labeled with GFP and stained with Hoechst 33342 prior to imaging (Koch et al., 2021).

the experiments. Xu et al. (2008) showed that it is possible to monitor the development of inkjet-printed ECs in tissue implants in vivo through magnetic resonance imaging (MRI). Contrast-enhanced MRI was used by intravenous injection of a contrast agent (Gd-DTPA) in mice to improve the signal-to-noise ratio (SNR). This way, there is no need to sacrifice the host for imaging by tissue dissection and the dynamics and functionality of the printed tissue implants can continuously be monitored by MRI in animal studies.

One of the applications of fabricated tissue constructs is in wound healing. After injuries, wound contraction is normally expected to happen however too much contraction leads to joint malfunction and undesirable aesthetic outcomes. Printed skin tissue constructs can be transplanted on the wound site to accelerate and improve the healing process. Yanez et al. (2015) fabricated a skin construct by printing HMVECs on fibrin that was sandwiched in between two layers of fibroblasts (bottom) and keratinocytes (top) suspended in collagen. They transplanted these skin constructs into full-thickness wounds on nude mice and found out that wound contraction would be reduced by 17% compared to a commercially-available wound dressing (apligraph) without ECs that showed similar wound contraction compared to no wound dressing controls. Furthermore, the ECs in the artificial tissue formed capillaries through self-assembly and integrated into the native tissue. This shows the great potential

of the fabricated skin constructs in the wound healing process that could eventually help patients with chronic wounds caused by a variety of medical conditions.

1.6. Significance of the study

Bioprinting is a powerful tool in many aspects and when it comes to tissue pre-vascularization with micro-scale capillaries, there are not many other methods that can compete with its precision, versatility, and ease of use. As mentioned, LBB offers an outstanding resolution and cell viability rate compared to other bioprinting techniques. By re-designing the DOD LBB technique that was previously developed in our lab (Ebrahimi Orimi et al., 2020), we provide solutions for flow compensation during high-speed printing and bioink inhomogeneity that introduce challenges for all nozzle-based bioprinting techniques.

There have been multiple studies that show the fabrication of blood vessels of various sizes. Larger blood vessels have been generated in a more controlled manner however the inclusion of capillary networks has been mostly random without having control over the design and the position of the fabricated networks. Using the substrate hydrogels that we have optimized in our lab for the purpose of guided angiogenesis (Orimi et al., 2022), we can generate more predictable and reproducible network patterns that could be used in angiogenesis assays or drug screening. Furthermore, the inclusion of perivascular cell types is crucial for the physiological function and stability of capillaries which is a subject that has not been touched a lot by other research groups. Using a re-designed configuration of a LBB technique that was developed in our lab, we fabricate such capillaries with multiple cell types.

Chapter 2

Aims and Objectives

Bioprinting is a technology that allows patterning cells and biomaterials with high spatial resolution. Our previously introduced in-house LIST LBB has major advantages over the well-known LIFT technique such as the potential to print constructs with clinically-relevant size, technical simplicity, and ease of use while still maintaining a comparable cell viability rate (Ebrahimi Orimi et al., 2020). However, nozzle clogging, flow compensation, and inhomogeneity of the cell suspension during print are a number of challenges that still exist in our bioprinting technique that could be addressed in a new configuration.

The native vasculature has a hierarchical complex structure with multiple cell types in several layers. Capillaries are the smallest blood vessel type in the hierarchy of vascular network and also the exchange site of nutrients and cellular waste with the tissues. As mentioned in the previous chapter, there have been several studies to pattern the ECs and allow their self-organization into capillaries. However, there are very few successful reports of the fabrication of these capillaries using multiple vascular cell types that aid in the maturation and stabilization of ECs.

The aims of this study are to:

- Re-design our in-house LIST technique to overcome a number of challenges we faced in the past
- Characterize the re-designed LIST configuration using a model ink and validate its cytocompatibility with a HUVEC-laden bioink

- Examine whether the bioprinted capillary-like structures recruit perivascular cell types

Our objectives include:

- Modifications to the vertical LIST setup to assemble the new horizontal configuration
- Adjusting the printing and bioink parameters to successfully deposit droplets and obtain reproducible printing patterns
- Conduction of a detailed study to characterize the printing potentials of the horizontal configuration allowing for the projection of the optimal printing parameters
- Validation of the biocompatibility of the horizontal LIST for cell patterning applications through HUVEC viability measurements
- Exploitation of the horizontal LIST to incorporate fibroblasts and PCs into the HUVEC capillary-like structures

Our group has previously investigated the optimal hydrogel substrate and bioink formulations to achieve guided angiogenesis through LIST bioprinting (Ebrahimi Orimi et al., 2020; Orimi et al., 2022). We continue to employ these formulations to fulfill the aims of our study.

Chapter 3

Methods and Materials

3.1. Preparation of the model ink

A fibrinogen solution (5 mg/mL) was prepared by dissolving fibrinogen from bovine plasma (F8630-5G, Sigma-Aldrich) in PBS (311-010-CL, Wisent Inc). The solution was pipetted several times and then placed on a vortex mixer for complete dissolution. Then Allura red dye (458848, Sigma-Aldrich) was mixed with the fibrinogen solution for a final concentration of 10mM to increase the absorbance of the 532 nm laser light.

3.2. Cell culture

HUVECs (PromoCell) were cultured in EGM-2 complete culture medium (CC-3156 and CC-4176, Lonza). For experiments, HUVECs were used in passages 3 or 4. Normal human lung fibroblast cells (IMR90) were cultured in DMEM 1x medium (319-016-CL, Wisent Inc.) that was supplemented with 10% fetal bovine serum. IMR90 cells were used in passages 17 to 30 for the experiments. Human brain pericytes (HBPC) were cultured in Pericyte Growth Medium 2 (C-28041, PromoCell) and were used in passages 7 or 8 for experiments. All culture media were supplemented with 2% Penicillin-Streptomycin Solution (30-002-CI, Corning) to minimize contamination. The cells were grown in Petri dishes coated with 0.1% bovine gelatin in sterile water and were cultured at 5% CO2, 37°C. The culture media was replaced 3 times per week and the cells were split when they reached 90% confluency.

3.3. Preparation of the cell suspension bioink

A fibrinogen solution (5 mg/mL) was prepared by dissolving fibrinogen from bovine plasma in warm EBM-2 basal medium (CC-3156, Lonza) at 37°C. The solution was pipetted several times and then placed on a vortex mixer for complete dissolution. The solution was then sterilized by passing through a 0.45 µm syringe filter with cellulose acetate membrane (28145-481, VWR) with minimal protein binding. Aprotinin from bovine lung (10820, Sigma-Aldrich) was added to the solution to reach the final concentration of 50 µg/mL. Then Allura red dye was mixed with the fibrinogen solution for a final concentration of 10mM to increase the absorbance of the 532 nm laser light. For the next step, the cells were treated with 0.05% Trypsin-EDTA (59417C, MilliporeSigma) for about 2-4 minutes and neutralized with DMEM complete medium. Cells were counted using a hemocytometer and centrifuged at 1200 RPM for 5 minutes. Then, the cell pellet was suspended in the red fibrinogen solution to reach the desired cell density of $20x10^6$ cells/mL (vertical LIST) or $5x10^6$ cells/mL (horizontal LIST).

3.4. Preparation of fibrin substrates

A portion of the fibrinogen solution was separated before mixing with the red dye and used for the preparation of the fibrin substrates. Using the drop-casting method, we deposited 15 µL thrombin 100 units/mL from bovine plasma (T7513-100UN, Sigma Aldrich) on an 18x18 mm^2 sterile glass cover slip. Then, 300 µL of the fibrinogen solution that had already been prepared was pipetted on the cover slip and the fibrin gel formed rapidly afterward. The thrombin stock solution was prepared at a concentration of 100 units/mL in a 0.1% (w/v) BSA solution dissolved in sterile water. The stock solution was aliquoted and kept at -20°C.

3.5. Preparation of Matrigel substrates

Matrigel (Growth Factor Reduced, Phenol Red-free, LDEVfree, Corning) which is solubilized basement membrane matrix secreted by Engelbreth-Holm-Swarm (EHS) mouse sarcoma was thawed at room temperature and was immediately put on ice to prevent gelation. To prepare the Matrigel substrates, 100 µL of Matrigel was mixed with 5 µL of thrombin 100

units/mL and then was deposited on an 18x18 mm^2 sterile glass cover glass. The Cover slip was kept inside a Petri dish and put in an incubator at 37°C for three hours for complete gelation.

3.6. Rheological characterization of fibrin substrates

The storage modulus (G') and loss modulus (G") of the fibrin hydrogels at three various fibrinogen concentrations (5, 7.5, 10 mg/mL) was measured using a Discovery, Hybrid-2rheometer (TA Instruments, New Castle, DE, USA). 7.5 µL drops of thrombin were spread on the fixed plate followed by deposition of 150 µL of fibrinogen solution in EBM-2 at the mentioned concentrations that led to cylindrical samples about 20 mm in diameter and 500 µm in thickness. The temperature was set to 22 °C and measurements were taken 15 min following the sample preparation (soaking time). The hydrogels were compressed by axial force and the applied oscillation strain ranged from 1% to 300% using an angular frequency of 10 rad/s. Storage and loss moduli were averaged over a range of strain between 1% and 10% where the rheology presents plateau regime in all samples.

3.7. Seeding four different formulations of IMR90 cell suspension on fibrin and Matrigel substrates

In this experiment, four fibrin substrates and four Matrigel substrates were prepared to test the effect of the different substrate and bioink formulations. The following cell suspension bioinks were prepared for a final cell density of 5 x 10^6 cells/mL:

- **CM+F+D**: DMEM basal medium, fibrinogen, Allura red dye, and IMR90 cells
- **CM+F**: DMEM basal medium, fibrinogen, and IMR90 cells
- **CM+D**: DMEM basal medium, Allura red dye, and IMR90 cells
- **CM**: DMEM basal medium and IMR90 cells

For each solution containing fibrinogen or Allura red dye, we used the concentration of 5 mg/mL and 10 mM in PBS, respectively. Each bioink was later pipetted on one fibrin and one Matrigel substrate and the samples were put in the incubator. Prior to the addition of

culture medium, the samples without fibrinogen in the bioink formulation were kept in the incubator for one hour and the samples that contained fibrinogen in the bioink formulation were kept inside the incubator for 20 minutes since thrombin helps with cell attachment. Images were taken after depositing the droplets (prior to adding the culture medium) and after adding the culture medium to verify cell attachment to the substrate. We took images after 3 days in culture to investigate the proliferation and migration of fibroblasts on fibrin and Matrigel substrates.

3.8. Live-dead assay for red dye cytotoxicity assessment

In this experiment, we exposed the fibroblasts to a solution of Allura red dye and observed the effect of the dye on IMR90 viability over three days and compared the viability rate with a control group that was not exposed to the dye. To do so, we trypsinized and counted IMR90 cells. Then after centrifugation and resuspension in DMEM culture medium, the cells were seeded on a 6-well plate at different concentrations. Considering the speed of IMR90 proliferation, the cells were seeded in each of the three pairs of the 6-well plate at a particular concentration that was predicted to reach confluency by the time of viability measurement. More precisely, 500,000 cells, 250,000 cells, and 150,000 cells were seeded in each of the three pairs of the wells for D0, D1, and D3 samples, respectively (table 3.1). The day after cell seeding, fibroblasts in the experimental group were exposed to 10 mM Allura red dye dissolved in DMEM complete medium for one hour and were kept at room temperature to mimic the 1-hour duration of bioprinting in which the cells stay at room temperature and are exposed to the dye. Fibroblasts in the control group were covered with DMEM complete medium during this period. Then, the plates in the experimental group were washed with PBS three times and then fresh DMEM culture medium was added and the samples were put inside the incubator. After an hour, the cells in the D0 samples in both experimental and control groups were trypsinized and centrifuged. Then IMR90 cells were resuspended in DMEM and 50 µL of the cell suspension was mixed with Trypan blue (17-942E, Lonza) in a 1:1 volume ratio. Since dead cells have a porous plasma membrane, Trypan

blue passes through their membrane and stains their cytoplasm. The membrane in live cells remains intact and they stay unstained. Using a hemocytometer and a 10x objective, the ratio of live cells over all cells was calculated for both control and experimental groups and reported as the viability rate on day 0. The same procedure was performed on the samples for day 1 and day 3. Data analysis and statistical comparisons were done through two-way ANOVA analysis.

Group	Day 0	Day 1	Day 3
Allura red 10 mM	500,000 cells	250,000 cells	150,000 cells
Control	500,000 cells	250,000 cells	150,000 cells

Table 3.1. Number of IMR90 cells seeded in a 6-well plate for Allura red cytotoxicity assessment.

3.9. Printing setup and procedure

We used a LBB technique that was developed in our lab and coined laser-induced side transfer or LIST. The first configuration of this printing technique was introduced by our lab in 2020 (Ebrahimi Orimi et al., 2020) which uses a bioink-filled hollow glass capillary (8330, Vitrocom, 0.3 mm inner diameter, 0.15 mm wall thickness and 50 mm long) vertically pointing toward the receiving substrate (figure 3.1.a). We use a nanosecond laser pulse (Ultra compact pulsed Nd:YAG, Nano L series) which is focused in the middle of the glass capillary via a 4X Olympus plan achromat objective. The bioink is supplied to the glass capillary through a piece of plastic tubing (ADF00001, Tygon) via a syringe pump (NE-1000, New Era Pump Systems Inc.). Following the focused laser pulse in the middle of the glass capillary, a bubble forms due to the evaporation of the bioink. The high pressure induced by the bubble causes the formation of a liquid jet and finally ejection of a bioink droplet from the distal end of the capillary toward the receiving substrate. The capillary end is located 500 µm below the focal point of the laser beam and about 500-650 µm above the receiving substrate. The system is comprised of all the optical elements and other parts that can be seen in figure 3.1.b. A detailed description of the printing setup has been already published

(Roversi et al., 2022). This configuration was used in the early stages of our cell studies before the seeding of secondary vascular cell types.

In this project, we came up with a new configuration that uses a horizontal glass capillary (8250, Vitrocom, 0.5 mm inner diameter, 0.15 mm wall thickness, and 50 mm long) with a 200 µm diameter orifice (laser-machined at Polytechnique Montréal) in the middle of the side that faces the receiver substrate (figure 3.2). In this configuration, the ends of the glass capillary are both connected to two pieces of plastic tubing, one of which is connected to the syringe pump. Therefore, it is possible to have an adjustable flow of the bioink through the glass capillary. The direction in which the bioink flows away from the syringe and towards the free end of the plastic tubing is called the injection direction and the reverse direction is referred to as the suction direction in this document.

3.9.1. Characterization of the horizontal LIST

For the characterization of the redesigned LIST, the cell-free model ink droplets were directly printed on microscopic glass slides (SKU BI0082B, Eisco Labs). The printing pattern of the samples was 500 µm apart droplets forming parallel 10 mm long lines that are 1 mm far from one another.

For the ink jet angle measurements, we chose two flow rates that are 15x and 50x multiples of the ink loss at the 20Hz printing rate, and monitored the jet angle during the injection and the suction of the model ink. The negative angles show the tendency of the ink jet to slant toward the direction of the flow during injection and the positive angles show the tendency of the ink jet to slant toward the direction of the flow during suction. The angle was measured with reference to the line that is vertical to the surface of the orifice (figure 3.3).

3.9.2. Cell printing experiments

To begin the printing procedure, the plastic tubing was loaded with the cell suspension bioink, and using the syringe pump, the bioink was pushed to reach the orifice and fill the

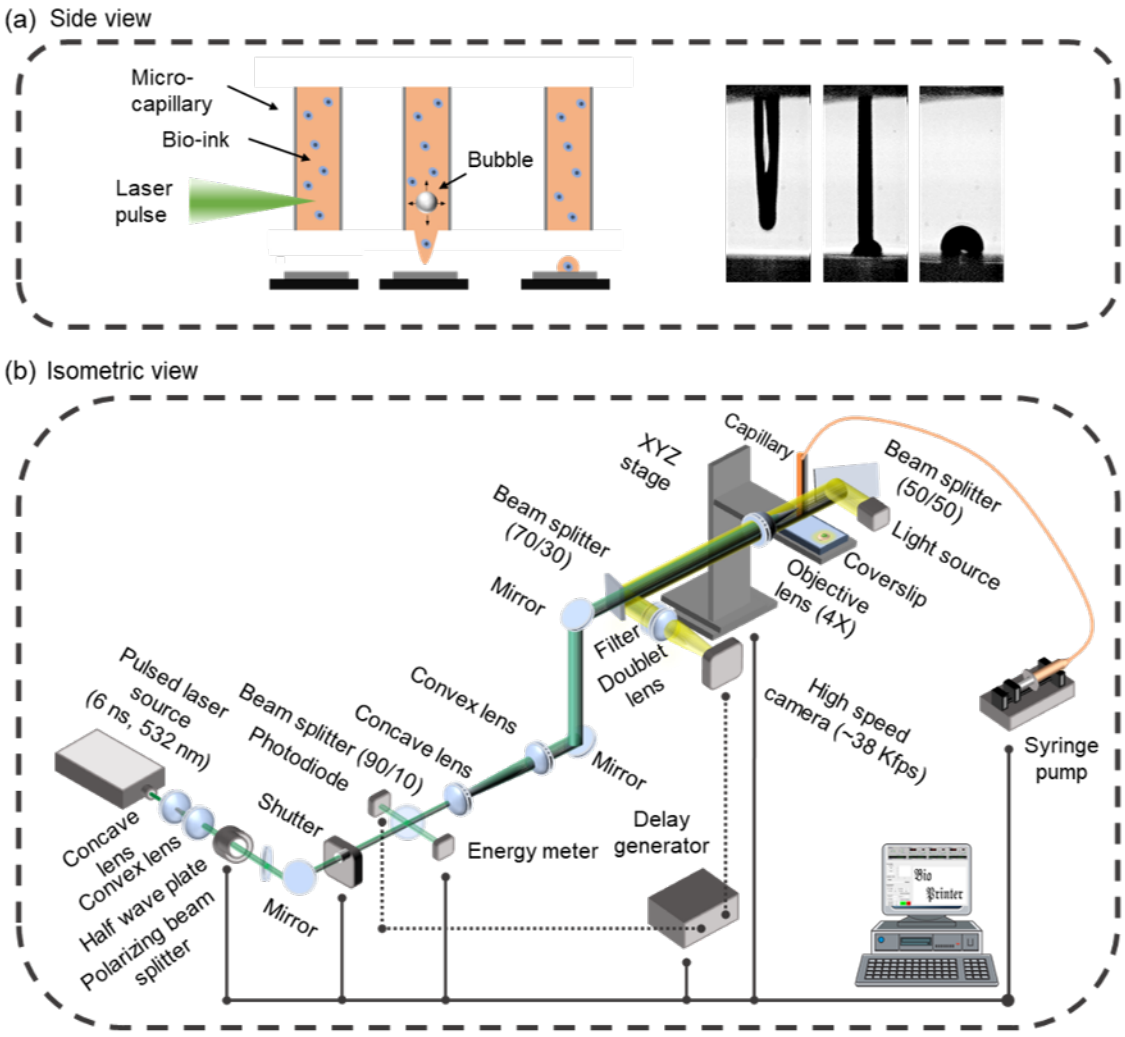

Fig. 3.1. Overview of LIST (a) schematic of LIST bioprinting (left) and high-imaging of jet formation and droplet ejection from the capillary tip onto the substrate (right) and (b) detailed schematic of LIST setup (Ebrahimi Orimi et al., 2020).

glass capillary. The receiving gel substrate was mounted on the motorized XYZ translation stage (PT1-Z8, Thorlabs) and was brought about 600-700 µm below the orifice. The energy of the laser beam at the capillary level was adjusted to about 60-80 µJ and a pattern of several 8 mm-long lines with a predetermined distance was given to the printer using MATLAB. The patterns were then printed with single droplets at the rate of 1 Hz.

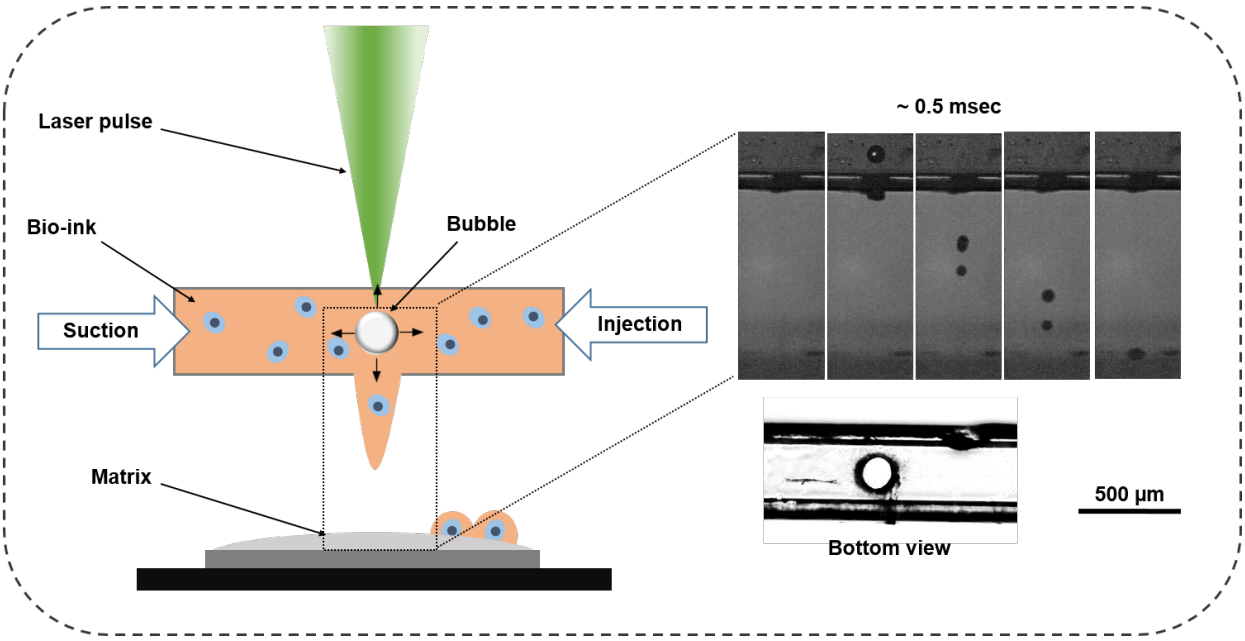

Fig. 3.2. Schematic of droplet printing using the horizontal configuration of LIST (left) and indicative images of droplet ejection in the horizontal LIST from the orifice on the capillary onto the substrate (upper right) and orifice at the bottom side of the glass capillary facing the receiving substrate (lower right).

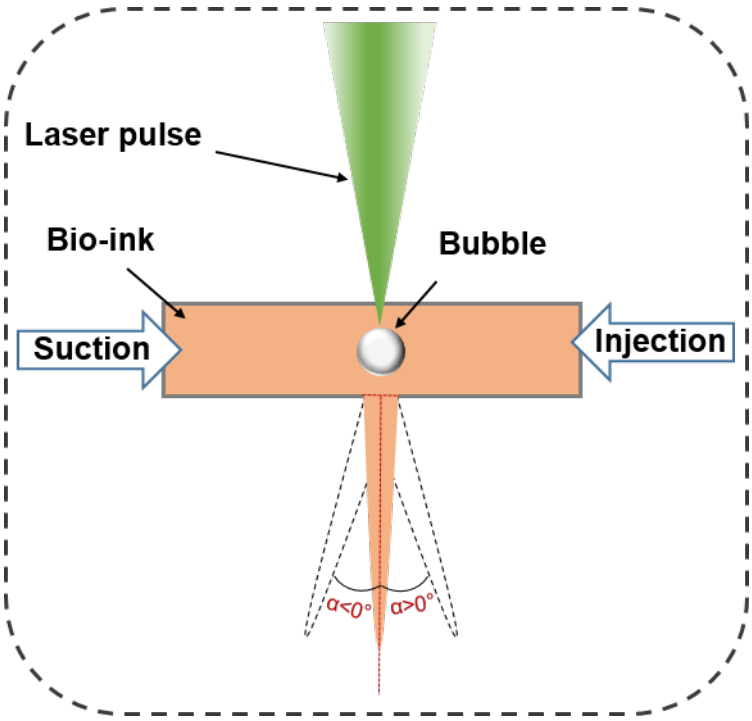

Fig. 3.3. Schematic diagram displaying the sign of the ink jet angle with regard to the direction of the ink flow through the capillary. The angle of the jet was measured in the plane that covers the length of the glass capillary and is perpendicular to the surface of the orifice.

3.10. Post-printing procedure

After printing, the samples were put in the incubator for about 20 minutes to allow time for cell attachment. Then, the culture medium was added and refreshed after 30 minutes to remove the diffused red dye. Afterward, the medium was replaced every other day.

3.11. Staining procedure and imaging

To distinguish the cells in experiments that involve more than one cell type, we stained them using PKH67 Fluorescent Cell Linker Kits (PKH67GL, MilliporeSigma) and PKH26 Red Fluorescent Cell Linker Kits (PKH26GL, MilliporeSigma). To do so, following the dissociation and centrifugation of the cells, they were washed with serum-free medium and then resuspended in Diluent C (CGLDIL, MilliporeSigma). The red or green fluorescent cell membrane labeling dye was mixed with the cell suspension for a final concentration of 2 µM. After keeping the suspension for 3-5 minutes in the incubator to allow the dye to bind to the cell membrane, an equal volume of fetal bovine serum was mixed with the suspension to stop the reaction. After a minute, the suspension was centrifuged again and washed with the complete medium 3 times. Then, the cells were ready to be mixed with the fibrinogen solution to make the bioink.

For the post-printing viability experiments, Calcein AM 0.402 µM (400146, Cayman chemical) and Hoechst 33342 14.2 µM (14533; Sigma-Aldrich) were used to distinguish the live and dead cells by fluorescent microscopy. Unlike dead cells, viable cells take up Calcein AM and following its hydrolysis by their intracellular esterases, release the fluorescent Calcein that emits green fluorescence when excited. On the other hand, Hoechst 33342 binds the cell DNA and stains the nuclei of all viable and dead cells, emitting bright blue fluorescence upon excitation. To stain the cells, after washing three times with PBS, the samples were exposed to a 1:1000 staining solution for 15 minutes and then imaged.

Zeiss AxioObserver Z1 motorized inverted microscope was used for imaging the samples.

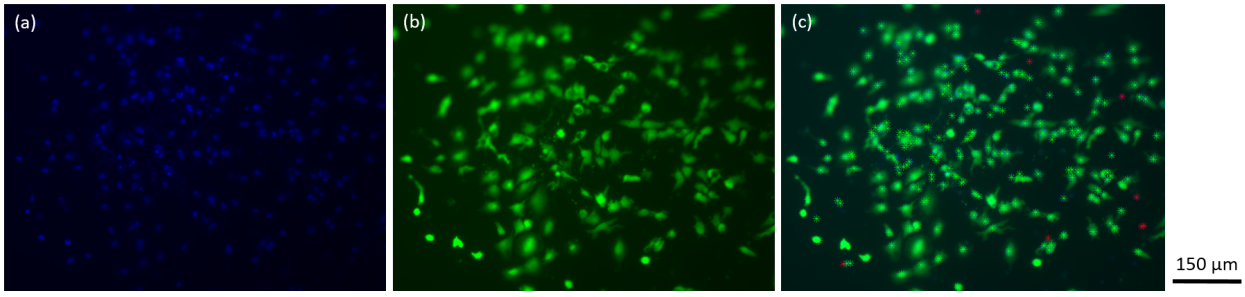

Fig. 3.4. Detection of viable and dead cells by our MATLAB algorithm. Hoechst 33342 and Calcein AM were used to stain (a) the nuclei of all cells (blue) and (b) the viable cells (green), respectively. (c) Any cell that did not meet our viability criteria was counted as dead and shown with a red asterisk compared to green asterisks for viable cells.

3.12. Image analysis and quantification

In the characterization study of the horizontal configuration of the LIST bioprinting technique, we developed a MATLAB algorithm that generates a binary image or matrix in which the area of the droplets is set to 1 and the background is zero. Then, the program treats each individual droplet as an object with its own properties including radius and circularity. This data was collected for each image of the droplets.

For the post-printing viability experiments, a MATLAB algorithm was developed that counts the number of cells by detection of the cell nuclei in the blue channel. As shown in figure 3.4, the cells were then considered viable if they follow the condition below in which I_c, I_b, and σ_i indicate the intensity of the cell, the intensity of the background, and the standard deviation of the intensity of the background, respectively:

$$I_c > I_b + 5\sigma_i \tag{3.12.1}$$

To quantify the IMR90 and HBPC recruitment experiments, first, we set the background intensity to zero using a MATLAB algorithm. Then, the integrated intensity of a region of interest (ROI) was measured with ImageJ. ROI was a thin rectangular area enclosing the printed HUVEC line while the remaining area of the image was used to measure the control intensity. All the intensity values were normalized for their respective area and relative intensity values were calculated using the following formula in which $I_{r,i}$, I_i, and I_0 denote the relative intensity in the i^{th} frame, intensity in the i^{th} frame, and intensity in the first

frame, respectively:

$$I_{r,i} = \frac{I_i - I_0}{I_0} \tag{3.12.2}$$

All the graphs and statistical comparisons were generated using GraphPad Prism.

3.13. Statistical Analysis

For the characterization of the horizontal list, two sets of experiments were performed to quantify droplet shape and jet angle. To measure the circularity and the radius of the printed droplets, three independent experiments were carried out. Across all three experiments, more than 90 droplets were printed and analyzed for each condition. The statistical analysis was carried out on all the data collected without grouping the data for each experiment together. To prevent the figures from becoming too crowded, individual values were not displayed. For the second set of experiments, 10 observations were made for each condition. All of the horizontal list characterization experiments were analyzed using a two-way ANOVA, followed by Tukey's multiple comparisons test.

Mechanical properties of fibrin hydrogel were measured three times in each of the three independent experiments for a total of 9 measurements. The data were analyzed through one-way ANOVA and Tukey's test was used for comparisons.

All the cell viability experiments were repeated three times and the data were analyzed by two-way ANOVA and compared using Tukey's test.

The IMR90 cell recruitment experiment was conducted three times and samples from each experiment were measured and the resulting values were averaged. Therefore the final analysis was based on three individual values. The data were analyzed through two-way ANOVA and Šidák's test was used for comparisons.

For all comparisons that were made, $P < 0.05$ was considered significant. All the values in the graphs are presented as mean ± standard deviation. GraphPad Prism version 9.5.1 was used for the statistical analyses.

Chapter 4

Results

4.1. Characterization of the horizontal configuration of LIST printing technique with a model ink

We performed a detailed study on the horizontal configuration of the LIST technique to characterize the printing conditions. We monitored the radius and circularity of the printed cell-free model ink droplets while exploring three variables; laser energy at the capillary, the flow rate of the ink through the glass capillary and the direction of the flow. We explored energies ranging from 20 µJ to 120 µJ with an interval of 20 µJ. At energies lower than 20 µJ, either we could not generate bubbles or the bubbles could not induce a high enough local pressure for the droplets to eject. Even at 20 µJ, we were hardly able to print droplets and the droplets did not land in the patterned position so it can be said that the energy threshold to print droplets is around 20 µJ for our model ink (figure 4.1). The effect of energies higher than 120 µJ was not explored due to the high possibility of breakage of the glass capillary wall. Printing was performed at the printing rate of 20Hz and ink flow rates were chosen as 1x, 5x, and 15x multiples of the rate of ink loss from the orifice of the glass capillary (i.e. the ink loss at the printing rate). The volume of the droplets printed by LIST was previously reported to be 1.675 to 6.1 nL (Ebrahimi Orimi et al., 2020). For our experiments, we estimated the droplet volume to be 5 nL, and given the printing rate, the flow rates were calculated to be 30, 90, and 300 µL/min. We explored the printing

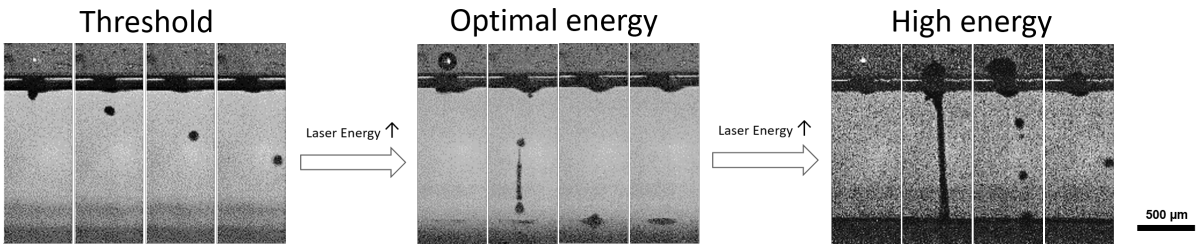

Fig. 4.1. Representative sequences of snapshots showing model ink jet evolution and droplet formation at different laser energies. The laser pulse was focused in the middle of the 500 µm ID capillary and 250 µm above its orifice. At the energy threshold, some of the laser pulses don't result in droplet formation and if formed, droplets generally do not land on the desired location. At high energy levels, droplet landing causes splashing and satellite droplets that might cause merging with adjacent droplets or a disorganized pattern. At the optimal laser energy, the laser pulse leads to the formation of round droplets that make small units of our desired pattern.

conditions during either injection or suction of the model ink through the glass capillary using a syringe pump. It can be seen how the shape of the droplets changes with alterations in the three mentioned variables in figure 4.2 during injection and in figure 4.3 during suction of the model ink. During both injection and suction, as we increase the laser energy, the droplets tend to get larger and satellite droplets are seen around the main printed droplets. They might also diverge from their patterned position and not land in the exact position that they're supposed to land on. As a result, at higher laser energies, the neighboring droplets merge and create a disordered final printing result. The undesirable pattern made the quantification harder as we did not have many single droplets at energies higher than 80 µJ to conduct droplet characterization. Therefore, we used the data in the laser energy range of 40 to 80 µJ for the data quantification.

4.1.1. Quantification of the circularity of the LIST printed droplets

One of the ways through which we can assess the quality of the printed droplets is by monitoring their circularity. Circularity is a measure of the roundness of 2D shapes and their resemblance to a perfect circle. Circularity values range from 0 to 1 with 1 being a perfect circle. In bioprinting, higher circularity values for the printed droplets are more favorable and signify more predictability of the shape of the final pattern.

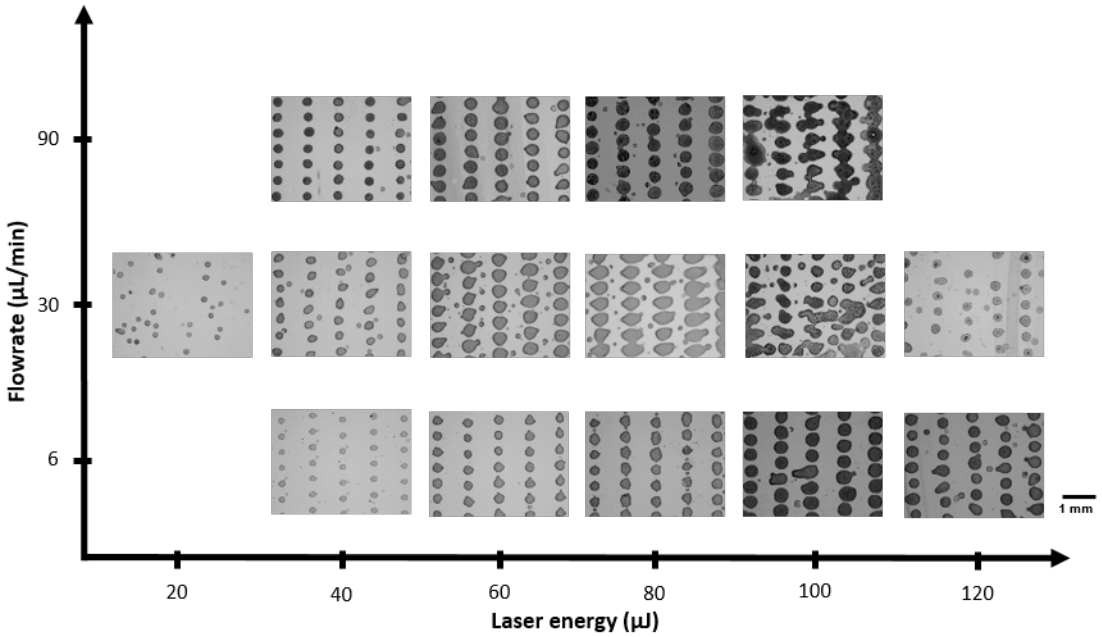

Fig. 4.2. Indicative images of the shape of droplets printed by horizontal LIST affected by ink flow rate and the laser energy during flow injection. Images were taken at 4x magnification.

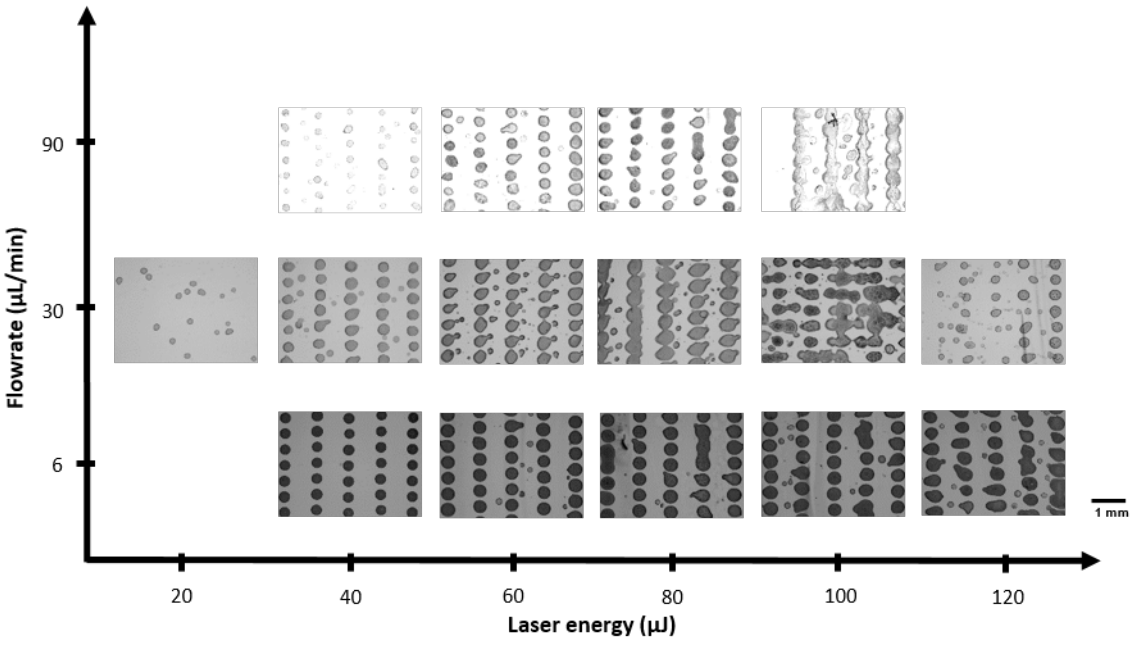

Fig. 4.3. Indicative images of the shape of droplets printed by horizontal LIST affected by ink flow rate and the laser energy during flow suction. Images were taken at 4x magnification.

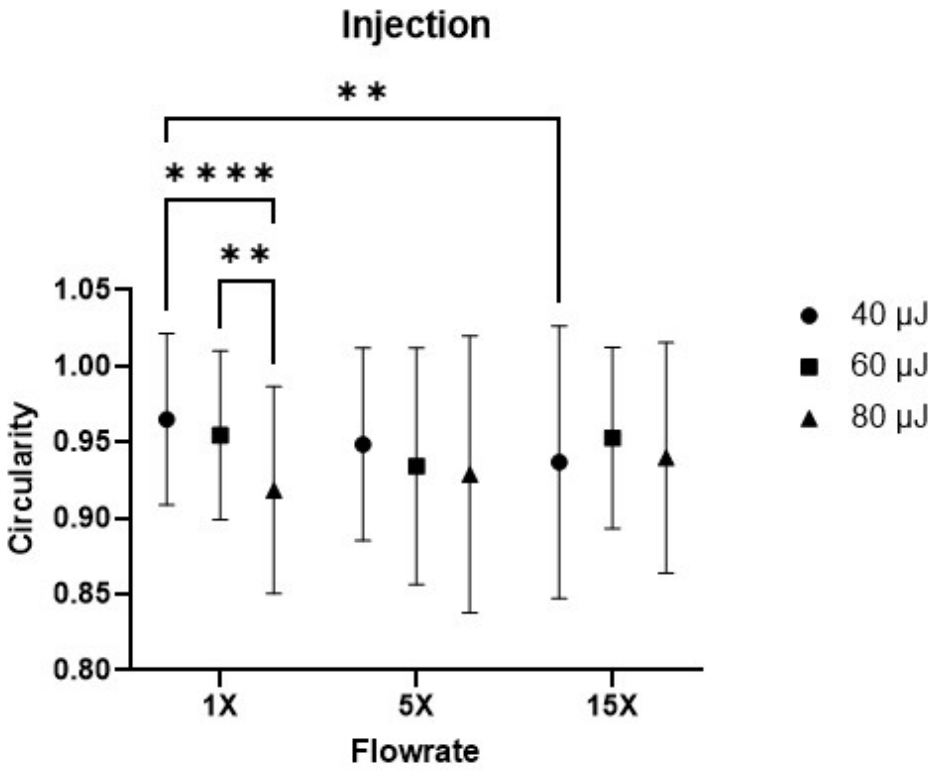

Fig. 4.4. Circularity of the droplets printed by the horizontal configuration of LIST during flow injection at three different energy levels (40, 60, and 80 µJ) and three ink flow rates (1x, 5x, and 15x; x denotes the rate of printing which is 6 µL/min at the 20 Hz laser repetition rate). The data were analyzed by two-way ANOVA and Tukey's test was used for multiple comparisons ($P > 0.05$). Shown are means±SD n=3.

According to figure 4.4, during injection, there's a general descending trend for circularity as the energy increases at 1x and 5x flow rates and for the 1x flow rate, such differences are significant. At 15x flow rate, we don't observe such a trend but the differences are statically insignificant based on the two-way ANOVA analysis. At constant laser energy, it is expected to see decreasing circularity in the higher flow rates and at 40 µJ, a significant reduction of droplet circularity at 15x flow rate compared to 1x flow rate is observed.

The data for the circularity of the printed droplets while the pump is withdrawing the model ink is shown in figure 4.5. As can be seen in the graph, all the significant changes are expected; in other words, droplet circularity has decreased with increasing laser energy or increasing flow rate. There is only one exception which is the value of circularity at 60 µJ laser energy and 15x flow rate which is significantly higher than 1x and 5x flow rates at the

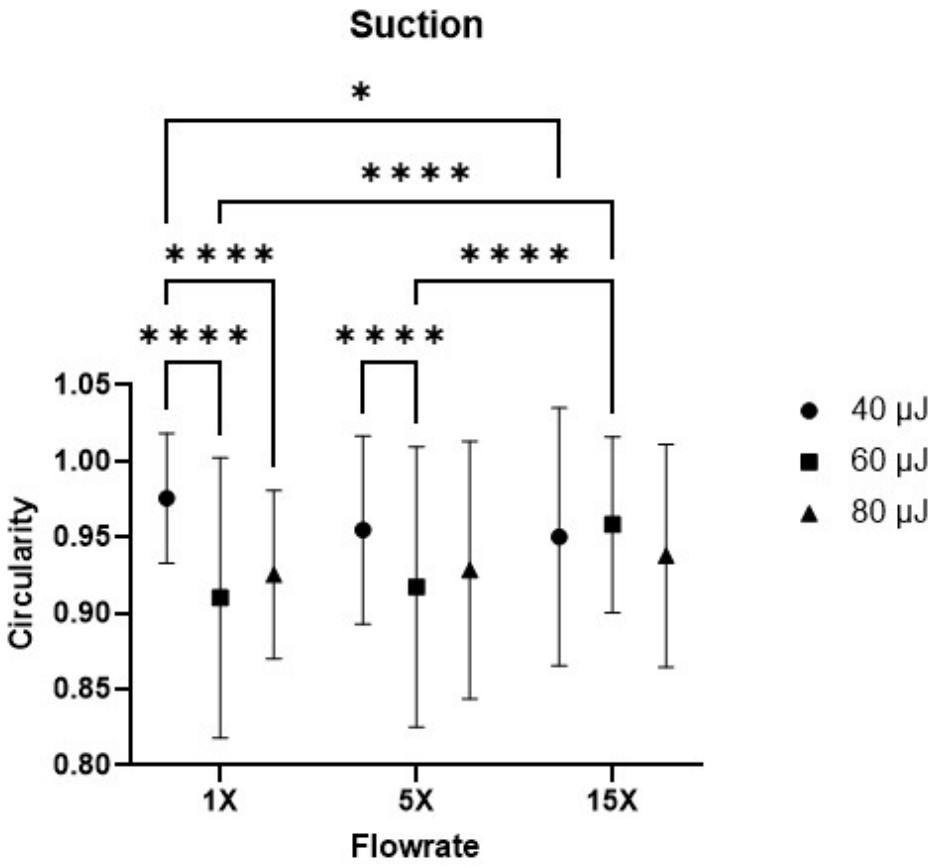

Fig. 4.5. Circularity of the droplets printed by the horizontal configuration of LIST during flow suction at three different energy levels (40, 60, and 80 µJ) and three ink flow rates (1x, 5x, and 15x; x denotes the rate of printing which is 6 µL/min at the 20 Hz laser repetition rate). The data were analyzed by two-way ANOVA and Tukey's test was used for multiple comparisons ($P > 0.05$). Shown are means±SD n=3.

same laser energy. This could be due to the lack of a large group of samples and might have become insignificant if the number of independent experiments was higher than 3. Otherwise, since we see that the trend of circularity is inconsistent with increasing flow rate, we could say that the circularity of the printed droplets might not have a strong association with the flow rate of the ink through the glass capillary.

4.1.2. Quantification of the radius of the LIST printed droplets

To be able to fabricate microcapillaries capable of mimicking the intricate structure of the ones in native tissue, the printed droplets need to be deposited with a high spatial resolution.

The radius of the printed droplets is a quantity that reflects the precision and resolution of the bioprinting method. Therefore, we performed this study to evaluate the printing resolution of the horizontal LIST and show the capabilities of this redesigned configuration.

Figure 4.6 shows the radius of the printed droplets at different laser energies and ink flow rates while pushing the ink through the horizontal glass capillary. It can be seen that there's an increasing pattern for the radius of the printed droplets when the energy of the laser increases at constant ink flow rates and the comparisons show significant differences for all comparisons except for 1x flow rate at 60 µJ vs. 80 µJ which still keeps the increasing pattern without being statically significant. At constant energy, there is a significant difference for 80 µJ at 1x vs. 5x and 1x vs, 15x flow rates which shows a positive correlation between flow rate and the radius of droplets but there are insignificant differences that show an inconsistent trend.

Finally, figure 4.7 shows the data for the radius of the printed droplet during the suction of the model ink with the syringe pump. At constant flow rate, once again, the energy of the laser shows a positive correlation with the radius of the printed droplet and except for one case at 60 µJ that shows an insignificantly larger droplet size compared to 80 µJ at 1x flow rate, the pattern seems to stay consistent. On the other hand, similar to the previously seen inconsistent patterns in figure 4.6, there are significant differences in the graph that show contradictory patterns for the effect of the bioink flow rate on the printed droplet size and we cannot deduce a clear trend from these data.

4.1.3. Quantification of the angle of the model ink jet at different flow conditions

Another study that we did to characterize this new horizontal LIST configuration was the measurement of the angle of the ink jet at different ink flow rates and the two flow directions. Figure 4.8 shows the angle of the ink jet at four different flow conditions. There is a significant difference between the angle of the jet at 15x and 50x during the injection.

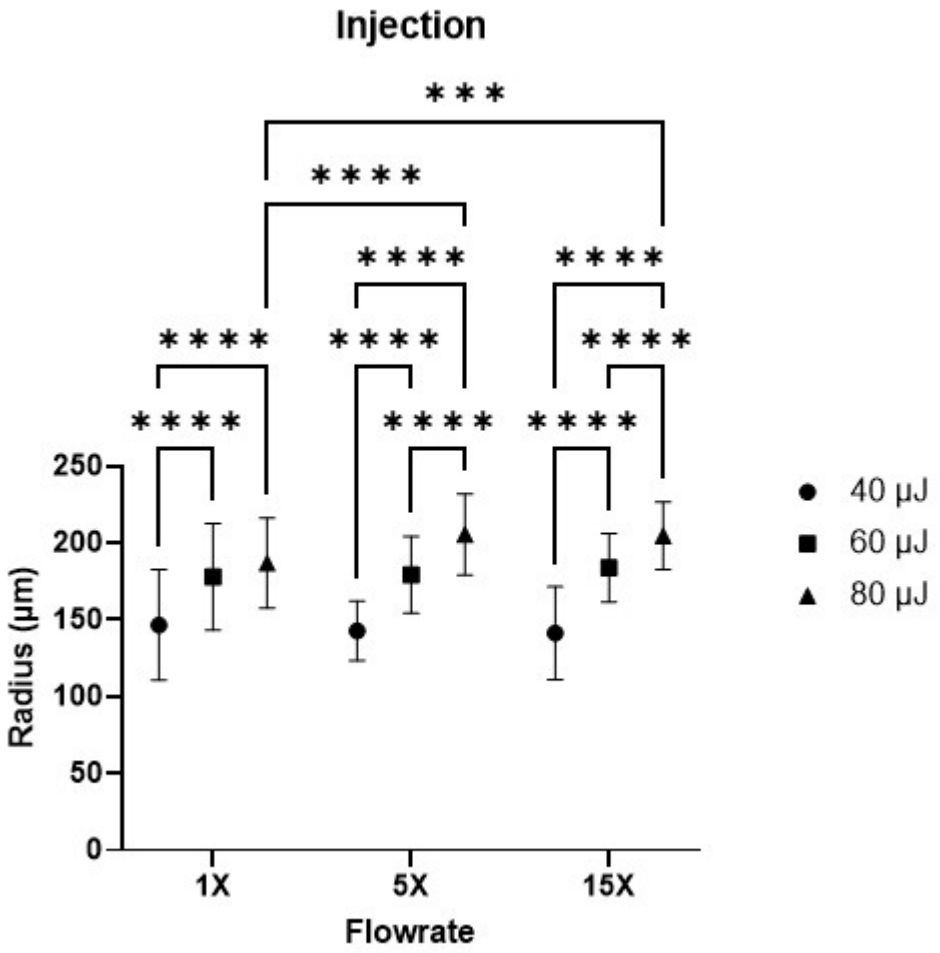

Fig. 4.6. Radius of the droplets printed by the horizontal configuration of LIST during flow injection at three different energy levels (40, 60, and 80 µJ) and three ink flow rates (1x, 5x, and 15x; x denotes the rate of printing which is 6 µL/min at the 20 Hz laser repetition rate). The data were analyzed by two-way ANOVA and Tukey's test was used for multiple comparisons ($P > 0.05$). Shown are means±SD n=3.

However, the mean of the changes in the angle of the jet is almost between -1° to 1° which is quite small and would not have a considerable effect on the final printed pattern.

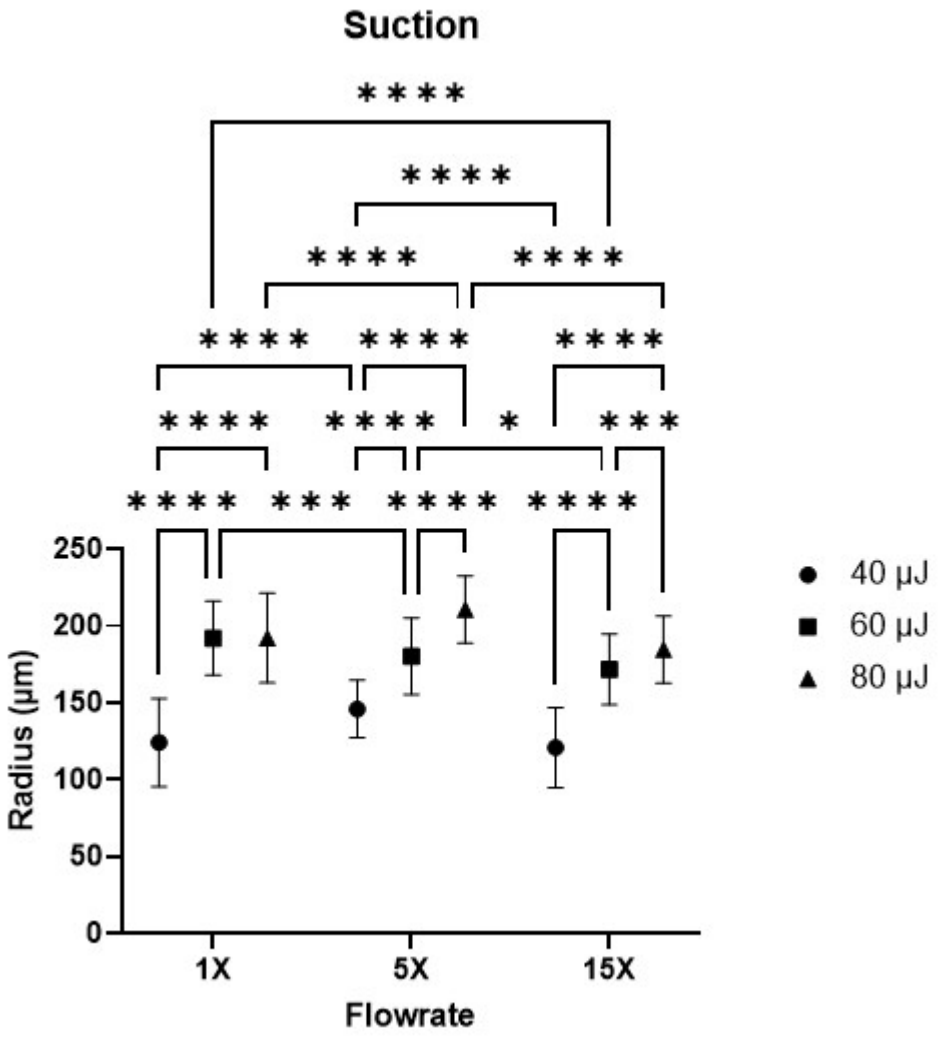

Fig. 4.7. Radius of the droplets printed by the horizontal configuration of LIST during flow suction at three different energy levels (40, 60, and 80 µJ) and three ink flow rates (1x, 5x, and 15x; x denotes the rate of printing which is 6 µL/min at the 20 Hz laser repetition rate). The data were analyzed by two-way ANOVA and Tukey's test was used for multiple comparisons ($P > 0.05$). Shown are means±SD n=3.

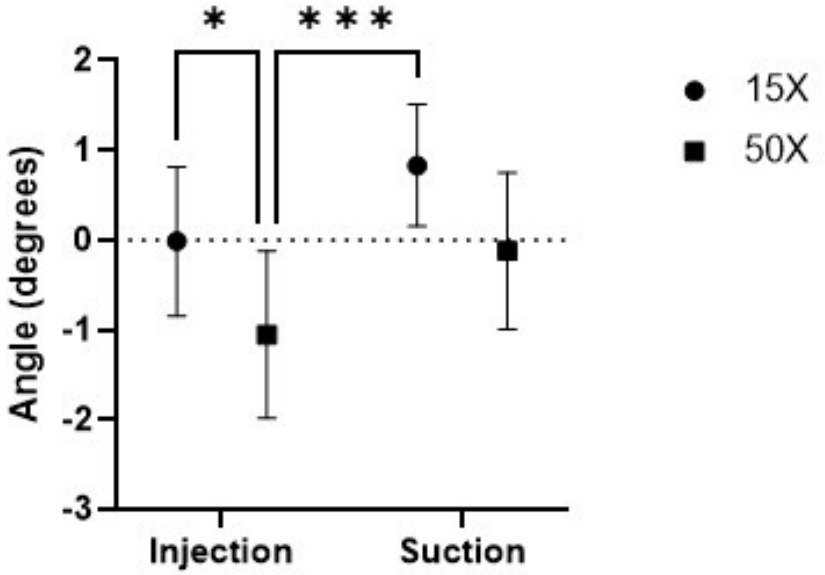

Fig. 4.8. Angle of the ink jet at two different flow rates (15x: 90 µL/min and 50x: 300 µL/min) during injection and suction of the flow. The data were analyzed by two-way ANOVA and Tukey's test was used for multiple comparisons ($P > 0.05$). Shown are means±SD n=3.

4.2. Validation of the cytocompatibility of the horizontal LIST

We conducted this study to validate the cytocompatibility of the horizontal LIST through the measurement of HUVEC viability. For these experiments, we were not planning to investigate the endothelial cord formation on the Matrigel/thrombin substrates so we used fibrin due to the relatively shorter preparation time, easier handling, and lower cost. First, we investigated the optimal formulation of fibrin substrates for printing with the horizontal LIST and then measured the viability of the horizontal LIST-printed HUVECs and compared it to the manually-pipetted controls.

4.2.1. Investigating the optimal formulation of the fibrin substrates for printing with the horizontal LIST

In several printing attempts with the horizontal configuration of LIST, we observed that the droplets that land on the fibrin substrates cause depressions in the gel which is not desirable. These depressions on the surface of the gel appear as round black circles during imaging and make the ultimate quantification difficult. HUVECs were printed on three different fibrin substrates with fibrinogen concentrations of 5, 7.5, and 10 mg/mL. In figure 4.9, it could be observed that the printed droplets caused the mentioned depressions on 5 and 7.5 mg/mL but only the fibrin substrate with the highest tested fibrinogen concentration had enough mechanical stiffness to withstand the stress caused by the landing droplets. We also performed rheology tests to explore these findings quantitatively. As can be seen in figure 4.10, storage and loss modulus for the highest concentration of fibrinogen is the highest but the comparison of these values between all fibrinogen concentrations shows insignificant differences. This could be as a result of the relatively large sample preparation variation of our rheometry approach that lowers the precision and hence, fails to give rise to significant differences in our measurements. At this concentration, most of the droplets smoothly land and sit on the gel without causing any perforations. Therefore, we conducted our upcoming

horizontal LIST printing experiments with fibrin substrates that are made with 10 mg/ml fibrinogen.

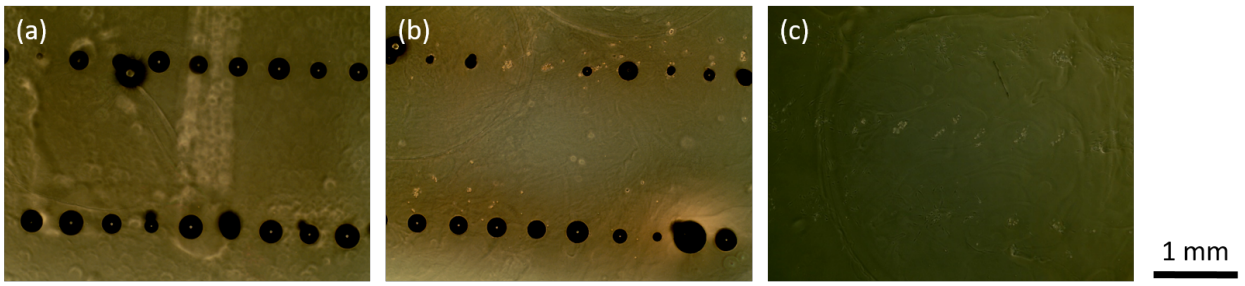

Fig. 4.9. Comparison of depressions caused by printed droplets on fibrin substrates with varying fibrinogen concentrations of (a) 5 mg/mL, (b) 7.5 mg/mL, and (c) 10 mg/mL. No depressions were observed for samples with the highest fibrinogen concentration. Images were taken at 4x magnification.

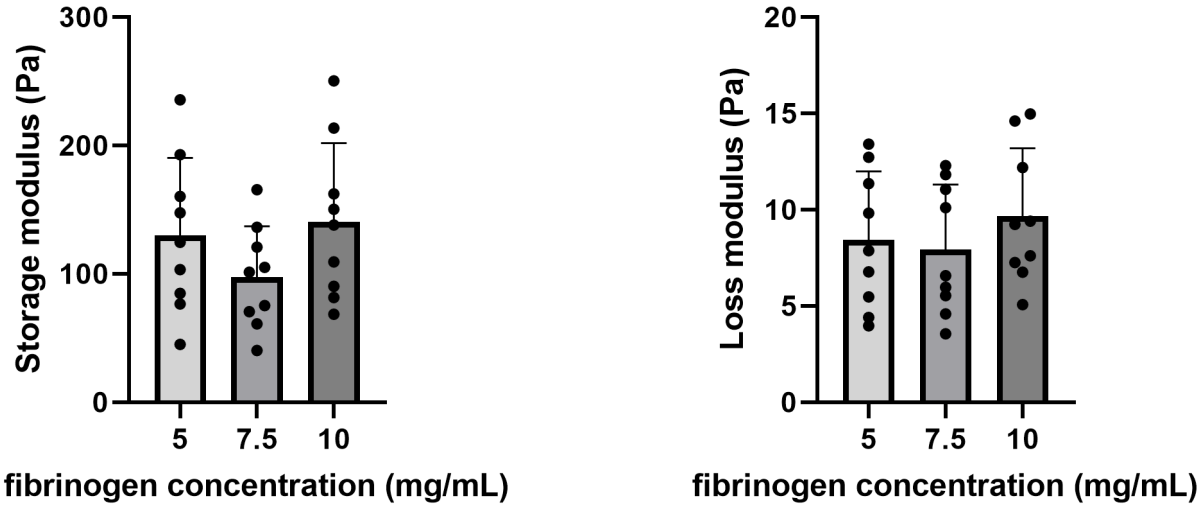

Fig. 4.10. Storage modulus (right) and loss modulus (left) of fibrin hydrogel with varying fibrinogen concentrations. The data were analyzed by one-way ANOVA and Tukey's test was used for multiple comparisons ($P > 0.05$). Shown are means±SD n=3 with points denoting each individual value.

4.2.2. Measurement of the viability of the horizontal LIST-printed HUVECs

In the vertical configuration of LIST, the cells were exposed to conditions that could differ from those of the horizontal configuration. Therefore, measurement of cell viability is needed

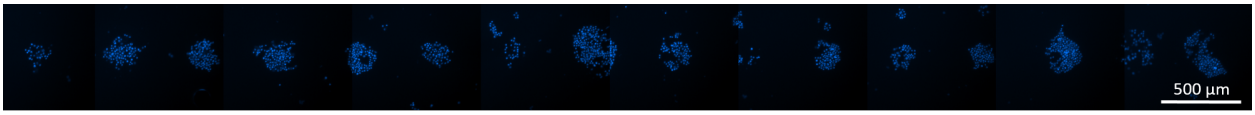

Fig. 4.11. HUVECs printed by the horizontal configuration of LIST. Cells were stained with Hoechst 33342 (blue). Images were taken one hour after printing at 10x magnification and stitched together due to the limited field of view.

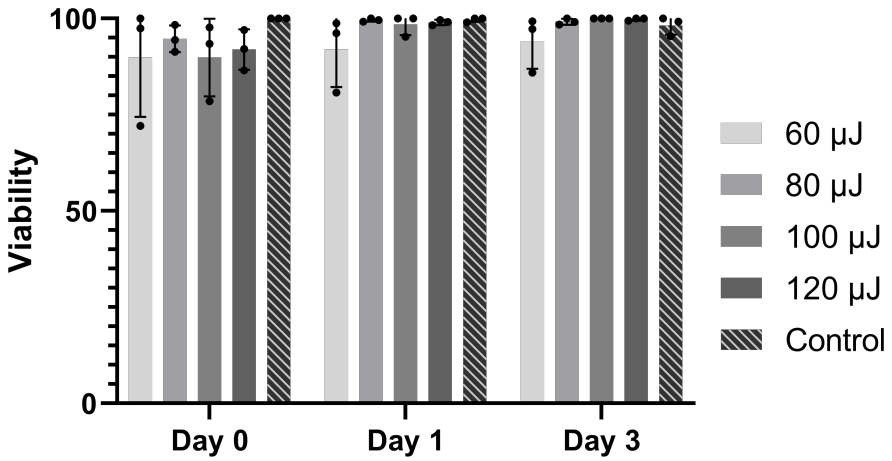

Fig. 4.12. Viability of HUVECs printed by the horizontal configuration of LIST at different laser energy levels from 60 to 120 µJ. The graph shows that the viability ratio of HUVECs printed by this configuration is generally 90% or more and this configuration does not significantly affect HUVEC viability. The data were analyzed by two-way ANOVA and Tukey's test was used for multiple comparisons ($P > 0.05$). Shown are means±SD n=3 with points denoting each individual value.

to verify this method for cell bioprinting applications. The viability of HUVECs that were printed by the horizontal LIST configuration (figure 4.11) was measured and compared with the pipetted controls right after printing and on the first and the third day after printing. It can be seen in figure 4.12 that the viability ratio for the printed samples at all energy levels is about 90% or above and there is no statistically significant difference between the viability of HUVECs at different laser energies printed by the horizontal LIST and the control samples. This shows that the horizontal configuration of LIST does not affect the viability of cells significantly and on average, maintains a high viability ratio of 90% or more.

4.3. Preliminary evaluation of a IMR90 cell-laden bioink for LIST bioprinting

We conducted a series of experiments to evaluate the compatibility of IMR90 cells with our bioink and substrate formulations and their behavior after printing. Although by the end of this section we will conclude that the inclusion of IMR90 cells in our HUVEC samples by printing is not feasible, these studies served as a stepping stone toward our ultimate objective of incorporating supporting cells.

4.3.1. Effect of Allura Red dye on IMR90 viability

The laser light that we use in our printing experiments has a wavelength of 532 nm and could have a high enough energy to break the glass capillary wall and hinder the progression of the experiment. By boosting the absorption coefficient of the bioink, the required laser energy for droplet ejection would diminish and the risks of damage to the equipment as well as injury hazards to the operator would be greatly reduced. We included Allura red dye in our bioink formulation to boost the laser energy absorption but the effect of this dye on IMR90 cell viability is unknown.

In this study, the effect of Allura red dye at the concentration that is used for our application was investigated. The cells were exposed to 10mM Allura red for 1 hour and then their viability was measured using the Trypan Blue exclusion test of cell viability. The measurements were compared to the viability rate of the control group that was cultured in the same conditions except for the 1-hour exposure to Allura red dye. It can be seen in figure 4.13 that the test showed there is no significant difference between the viability of the experimental and the control group over three days. Therefore, during our bioprinting process, Allura red dye does not significantly affect the viability of fibroblasts at 10 mM concentration.

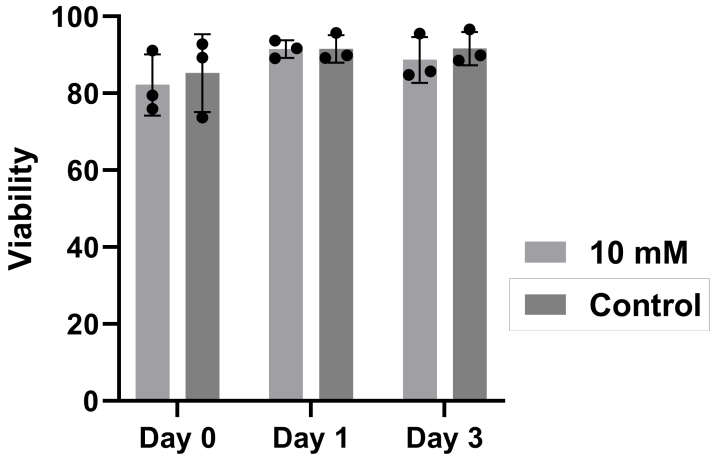

Fig. 4.13. Viability of IMR90 fibroblasts over three days after the one-hour exposure to 10 mM Allura red dye. There is no significant effect on IMR90 viability between the 10mM Allura red and the control group. The data were analyzed by two-way ANOVA and Tukey's test was used for multiple comparisons ($P > 0.05$). Shown are means±SD n=3 with points denoting each individual value.

4.3.2. Seeding four different formulations of IMR90 cell suspension on fibrin and Matrigel substrates

Fibroblasts can show contrasting phenotypes from round clustered morphology to an extended spindle-like shape depending on their environment. We conducted this set of experiments to assess IMR90 cell behavior on our gel substrates and see if the ingredients in the formulation of our cell suspension bioink affect these behaviors.

First, we investigated the effect of fibrin substrate (fibrinogen 5 mg/mL) as well as fibrinogen (F) and Allura red dye (D) in the bioink formulation on fibroblast behavior. The bioink droplets that contained fibrinogen solidified rapidly after being pipetted on fibrin and the fibroblasts stayed attached to the substrate. It is apparent in figure 4.14 that in the samples with fibrinogen-containing bioink formulations (CM+F+D and CM+F), fibroblasts remained on the substrate after adding the culture medium and did not detach but due to the presence of fibrinogen in the droplets which leads to the reaction with the remaining thrombin and quick gelation after landing on the substrate, the cells got trapped inside the

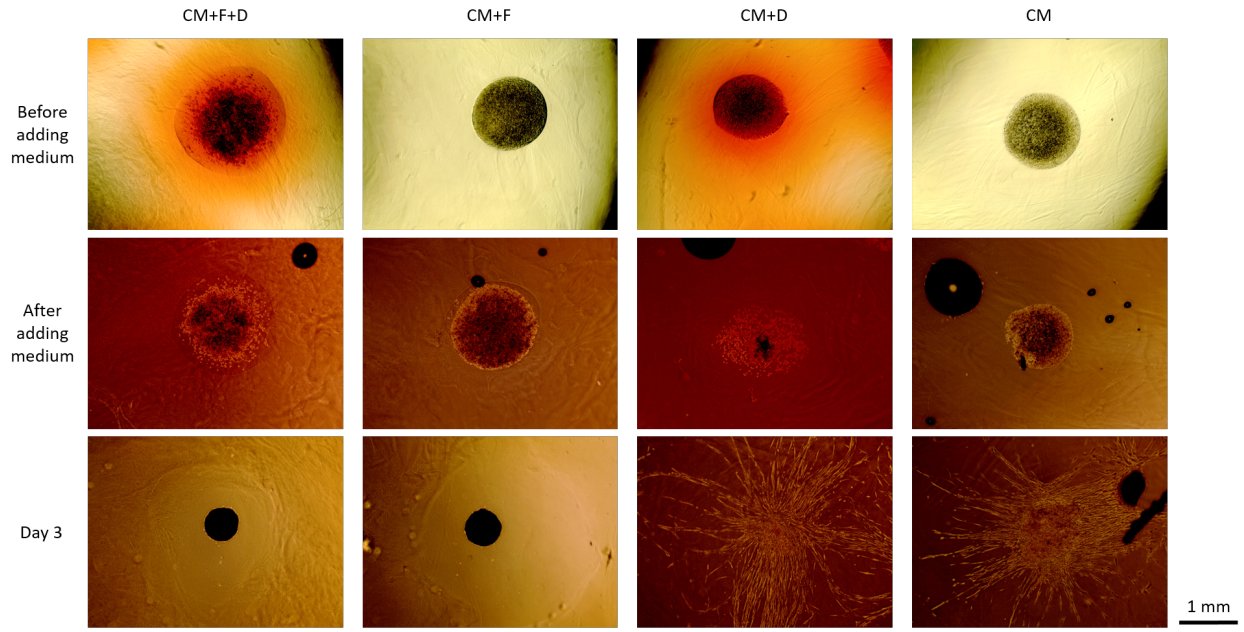

Fig. 4.14. Four formulations of IMR90 cell suspension bioink pipetted on fibrin substrates. The base solvent for all formulations was DMEM culture medium (CM) and the effect of fibrinogen (F) and Allura red dye (D) in the bioink formulation was investigated. Images were taken from samples after droplet deposition (top row), after the addition of culture medium (middle row), and after three days in culture (bottom row) at 4x magnification.

initial area defined by the gelled droplet even until day 3. In other words, the cells were confined to the periphery of the printed droplets even after three days in these samples. In contrast, we can see in figure 4.14 that the bioink droplets that did not contain fibrinogen (CM+D and CM), lost a few cells after the addition of the culture medium but did not confine the cells to a limited area. After three days, the cells proliferated and spread throughout the fibrin substrate and developed a stretched spindle-like phenotype. It is also noteworthy to mention that there was no observable effect of Allura red dye on IMR90 cell behavior and for the bioink formulations with dye, CM+F+D and CM+D, fibroblasts showed similar behavior in our microscopic images compared to the bioink formulations that lacked the dye, CM+F, and CM+D, respectively.

Then the behavior of the manually-pipetted IMR90 cells was assessed on Matrigel/thrombin substrates after being suspended in the four mentioned bioinks. Similar to what we observed on fibrin substrates in figure 4.14, due to the presence of thrombin in our gel substrate formulation, the bioink droplets that contained fibrinogen gelled soon after they were

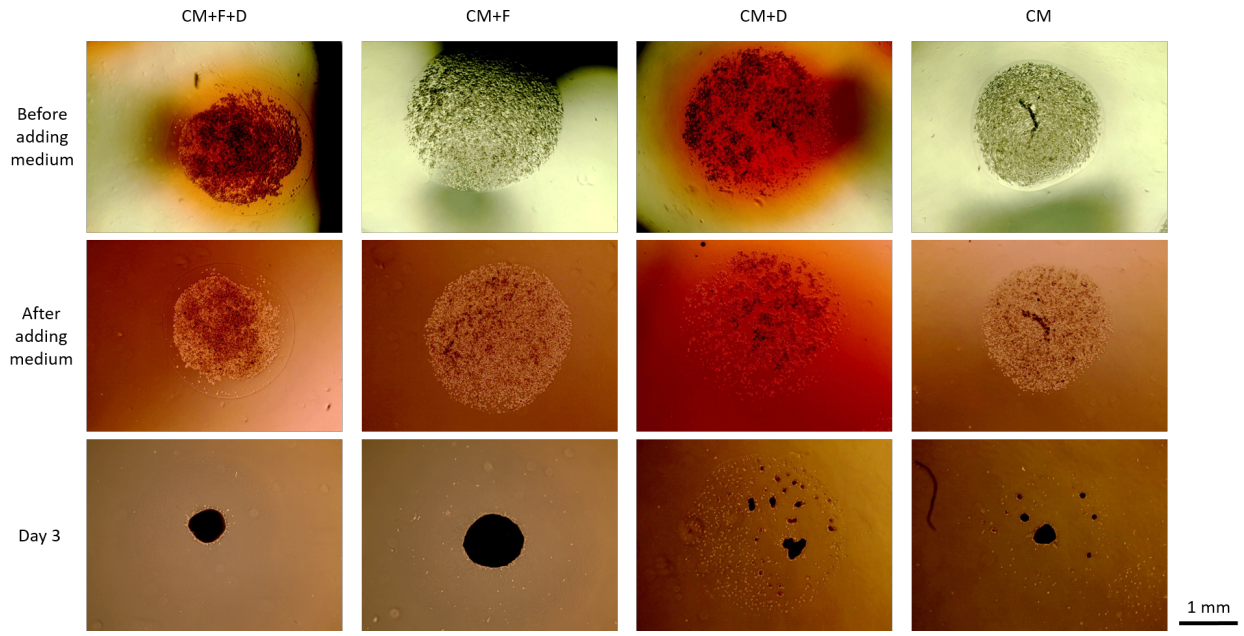

Fig. 4.15. Four formulations of IMR90 cell suspension bioink pipetted on Matrigel substrates. The base solvent for all formulations was DMEM culture medium (CM) and the effect of fibrinogen (F) and Allura red dye (D) in the bioink formulation was investigated. Images were taken from samples after droplet deposition (top row), after the addition of culture medium (middle row), and after three days in culture (bottom row) at 4x magnification.

deposited on Matrigel and resulted in a better cell attachment of fibroblasts. It can be seen in figure 4.15 that in samples with fibrinogen-containing bioinks (CM+F+D and CM+F), fibroblasts remained on the substrate after the addition of the culture medium and did not detach, but since their formulation contained fibrinogen, the cells remained inside the initial area defined by the gelled droplet on day 3. However, we can see in figure 4.15 that bioink droplets that did not have fibrinogen (CM+D and CM) lost a few cells after the addition of the culture medium. Furthermore, after three days, the majority of the fibroblasts were detached and the ones that were still on the substrate did not proliferate or migrate to other areas and kept their round morphology. Some of the cells in these groups formed clusters that could be seen as black areas in figure 4.15 due to the high density of cells. Moreover, there was no observable effect of Allura red dye on IMR90 cell behavior and for the bioink formulations with dye, CM+F+D and CM+D, fibroblasts showed similar behavior in our microscopic images compared to the bioink formulations that lacked the dye, CM+F, and CM+D, respectively.

4.3.3. Printing IMR90 on Matrigel substrates

Unlike HUVECs, we had difficulties printing IMR90 cells with the horizontal LIST due to quick cell aggregation and capillary clogging during the bioink injection with the syringe pump after the bioink loading step. However, in the vertical LIST, it is possible to load the bioink through the capillary end directly from the reservoir by suction with the syringe pump. Therefore, we printed fibroblasts with the old configuration of LIST. Furthermore, we already showed that printed HUVECs on thrombin-containing Matrigel substrates stay attached to the gel, develop intercellular connections with adjacent cells, and form tubular structures after a few days in culture Orimi et al. (2022). Since we want to study the incorporation of fibroblasts in these HUVEC tubular structures that are formed on Matrigel, we need to use the same substrate. Therefore, in this experiment, we studied how printed IMR90 cells evolve over time on thrombin-containing Matrigel substrates.

It can be observed in figure 4.16 that fibroblasts start forming connections as soon as day 1 in culture and gradually start connecting to the adjacent patterned lines of cells that are 2mm apart on day 5. These observations are in accordance with the behavior of manually-pipetted fibroblasts in Matrigel which show the aggregation of IMR90 cells over time.

4.3.4. Preliminary efforts to incorporate IMR90 cells into HUVEC cord-like formations

As a first step to incorporate fibroblasts in the tubular structures made by printed HUVECs, we tried several printing patterns including the print of fibroblasts on top of HUVECs, in parallel to them or changing the spacing between the lines in the patterns to determine the optimal printing pattern of the second cell type. Regardless of the cell printing pattern, IMR90 cells seemed to be unaffected by the HUVECs and formed the same cell clusters that we previously observed when printing them alone (figure 4.16). What's more, they caused clustering of the HUVEC patterns that used to form tubular structures on their own and made them aggregate likewise (figure 4.17). Therefore, this attempt to include fibroblasts in our samples was unsuccessful and we observed that the effect of IMR90 cells on HUVECs was

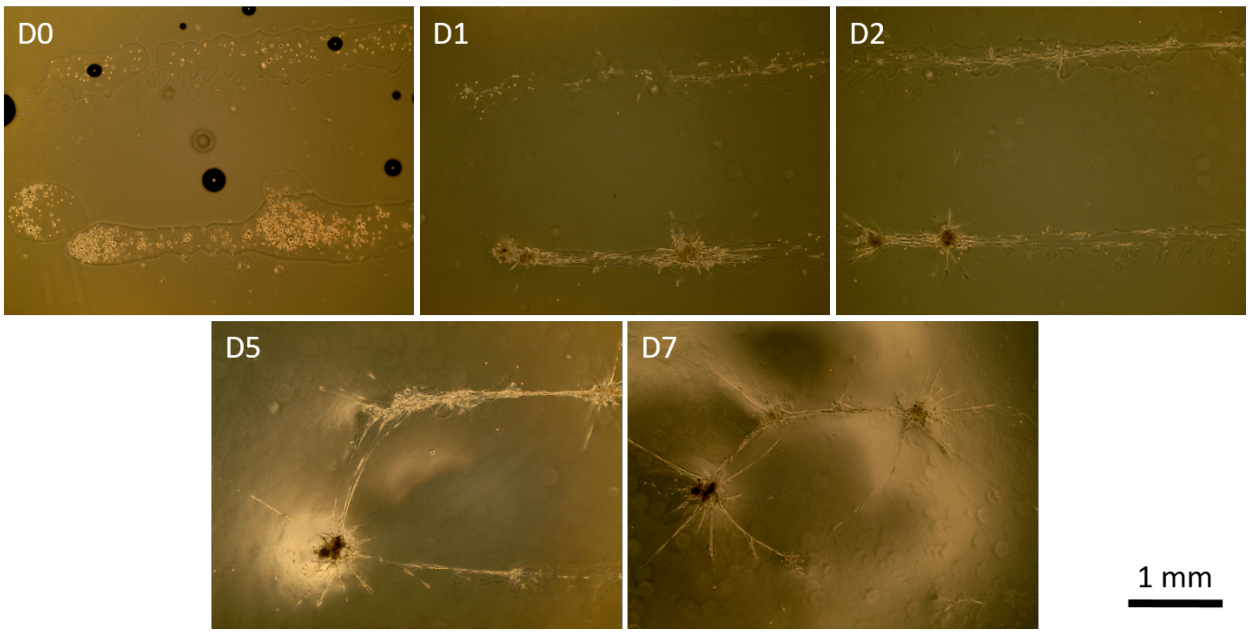

Fig. 4.16. Printed IMR90 cells on Matrigel over 7 days in culture. Fibroblasts form connections with neighboring cells and gradually start forming cell clusters after 5 days in culture. Images were taken at 4x magnification.

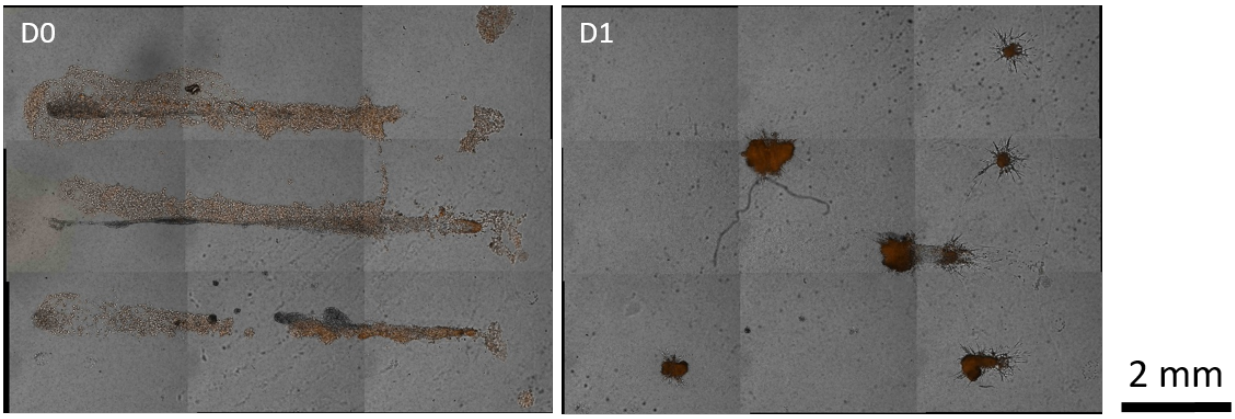

Fig. 4.17. IMR90 cells printed on top of previously printed HUVEC lines. IMR90 cells are stained with PKH26 (red). Images were taken one hour after IMR90 printing and on day 1 at 2.5x magnification and stitched together due to the limited field of view.

too harsh. In other words, the examined printing cell density of fibroblasts caused HUVECs to cluster instead of forming the previously-observed tubular structures Orimi et al. (2022). As a result, we decided to move forward with a new strategy and seed the second cell type at a lower concentration on the printed HUVEC samples.

4.4. Incorporation of the perivascular supporting cell types in endothelial structures

4.4.1. Seeding IMR90 cells on printed HUVECs on Matrigel substrates

Since the effect of fibroblasts at 20x10^6 cells/mL printing concentration was too strong on HUVECs and caused them to cluster, we tried to reduce this fibroblast effect by seeding IMR90 suspensions with low cell densities on printed HUVEC patterns to see how the two cell types react. In this study, we seeded three different concentrations of IMR90 cells on printed lines of HUVECs four days post-printing. The IMR90 concentrations used in this experiment were 136,000 cells/ml, 34,000 cells/ml, and 8,500 cells/ml. We can observe in figure 4.18 that printed patterns of HUVECs still disintegrated as a result of the strong effect of fibroblasts at the highest concentration but for the middle concentration of 34,000 cells/ml, we saw that surprisingly, IMR90 cells start attaching to the printed HUVEC lines as soon as they were seeded and move along the length of the lines. The observed recruitment of IMR90 cells on the HUVEC lines happens without the previously seen disintegration of the printed HUVEC patterns. In the samples with the lowest concentration of seeded fibroblasts, HUVEC lines still recruited IMR90 cells but there were much fewer cells to attach to the line so it was harder to see the cell recruitment. Therefore, the middle concentration (34,000 cells/ml) was chosen to be optimal for our experiment as the effect of cell recruitment could be easily seen without forcing the printed HUVEC patterns to aggregate into cell clusters along with fibroblasts. The time-lapse of the aggregation of the HUVEC patterns for the highest concentration and recruitment and movement of fibroblasts along the printed HUVEC lines for the middle (optimal) and the lowest concentration of IMR90 cells from 1 to 16 hours after printing is shown in figure 4.18.

A narrow region of the sample enclosing a printed HUVEC line with the optimal seeding IMR90 concentration over a 15-hour period is shown in figure 4.19. It can be observed that the stained fibroblasts gradually attach to the HUVEC pattern as the intensity of the red

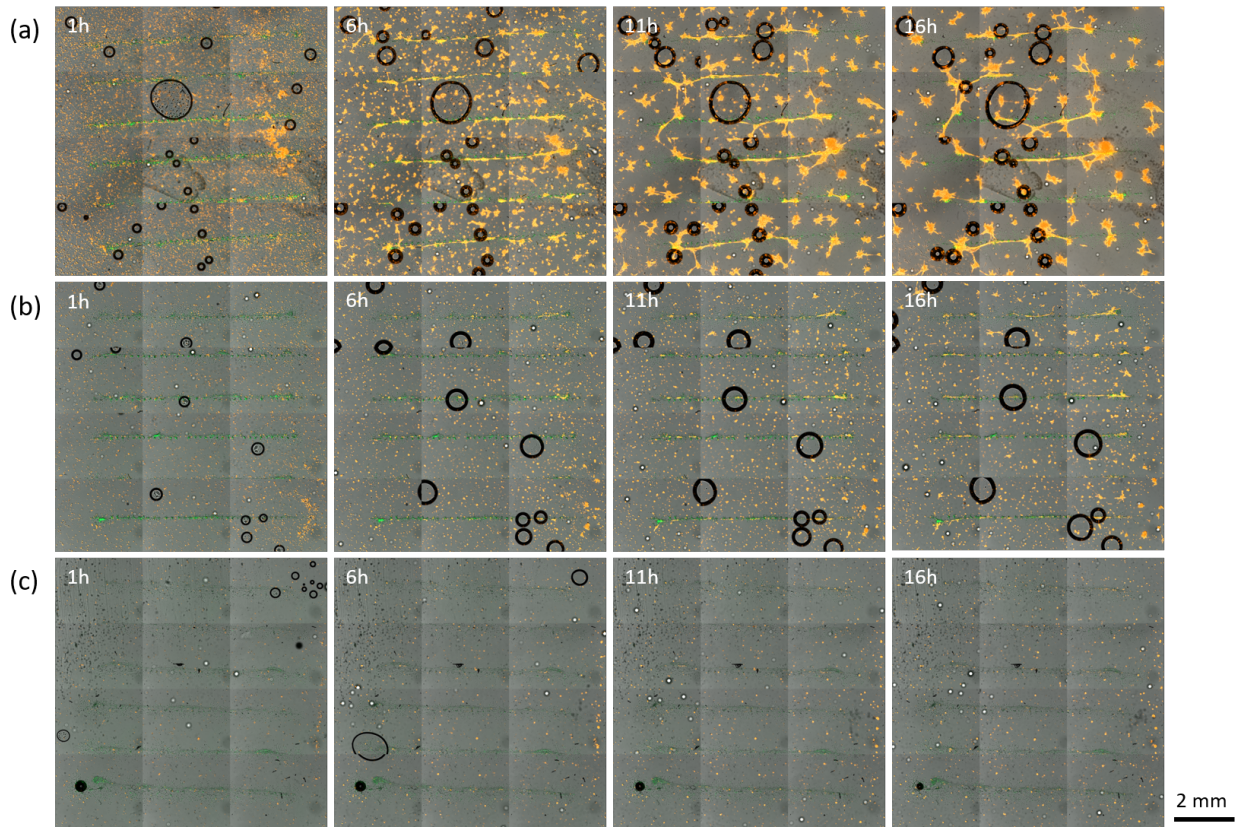

Fig. 4.18. Seeding IMR90 cells at three concentrations of (a) 136,000 cells/mL, (b) 34,000 cells/mL, and (c) 8,500 cells/mL on the printed line patterns of HUVECs 1, 6, 11, and 16 hours after seeding. HUVECs and IMR90 cells were stained with PKH67 (green) and PKH26 (red). The black circles only show the periphery of the bubbles that were floating on top of the culture medium and are not meant to point to any particular details. Images were taken at 2.5x magnification and stitched together due to the limited field of view.

channel is increasing over the HUVEC line. It's also worth mentioning that the fibroblasts that are located further from the line are less likely to attach to HUVECs and instead, form cell clusters that have been seen before.

4.4.2. Seeding HBPCs on printed HUVECs on Matrigel substrates

PCs are known for their role in the support and maturation of ECs. Therefore, to fabricate stable capillary networks, the inclusion of pericytes is essential. To include PCs, instead of printing HBPCs on HUVECs, we decided to observe their behavior at a low seeding concentration as a first step and if need be, we would explore their incorporation by printing. Therefore, we performed a study to find the optimal seeding concentration

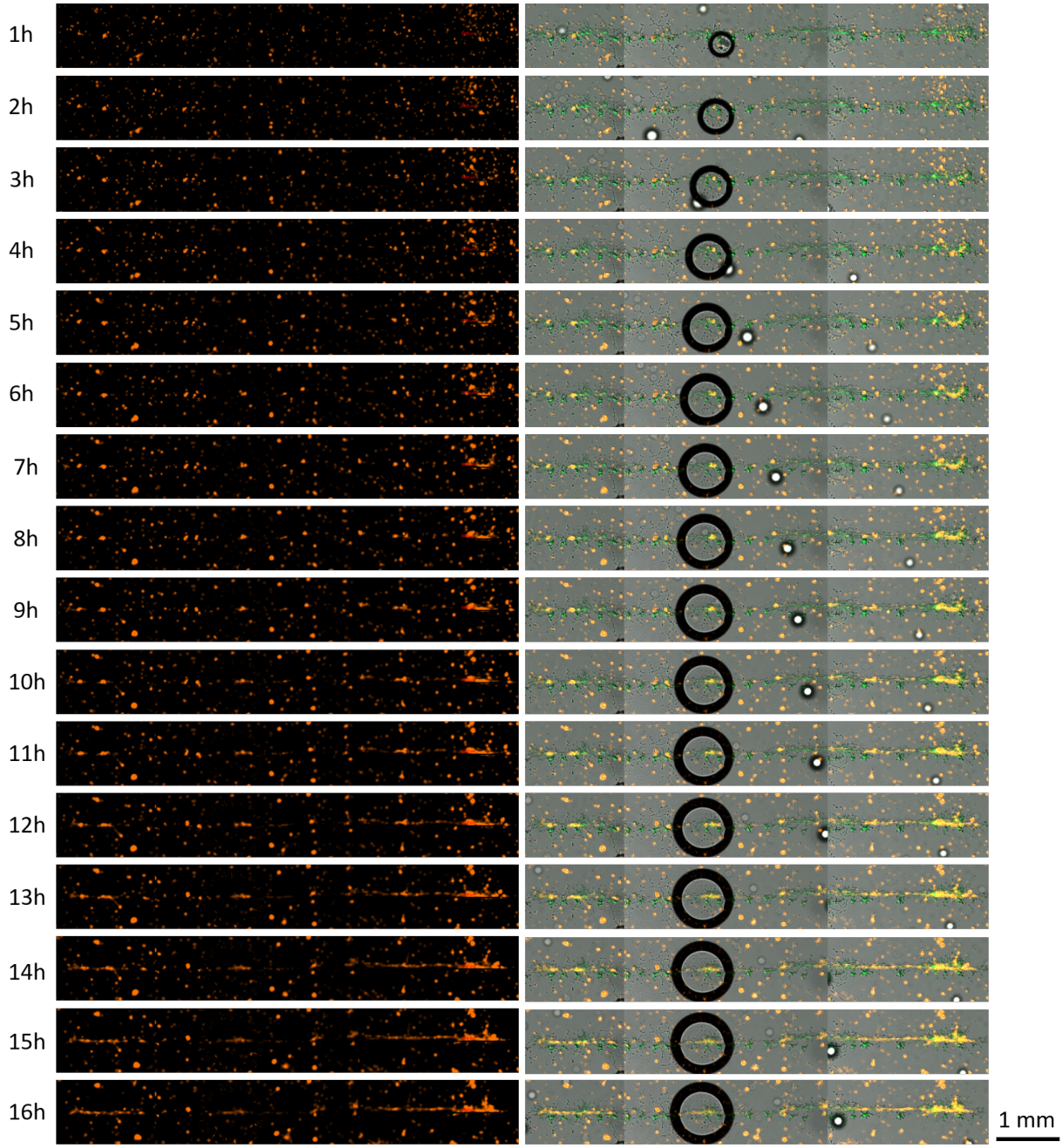

Fig. 4.19. Time lapse of seeding IMR90 cells at the optimal concentration (34,000 cells/mL) on a printed HUVEC line. Images were taken for 15 hours with a 1-hour time interval. HUVECs and IMR90 cells were stained with PKH67 (green) and PKH26 (red). The black circles only show the periphery of the bubbles that were floating on top of the culture medium and are not meant to point to any particular details. Images were taken at 2.5x magnification and stitched together due to the limited field of view.

of PCs on printed HUVEC lines. We prepared HBPC cell suspensions with two different concentrations of 136,000 and 34,000 cells/mL. The images that were taken starting an hour

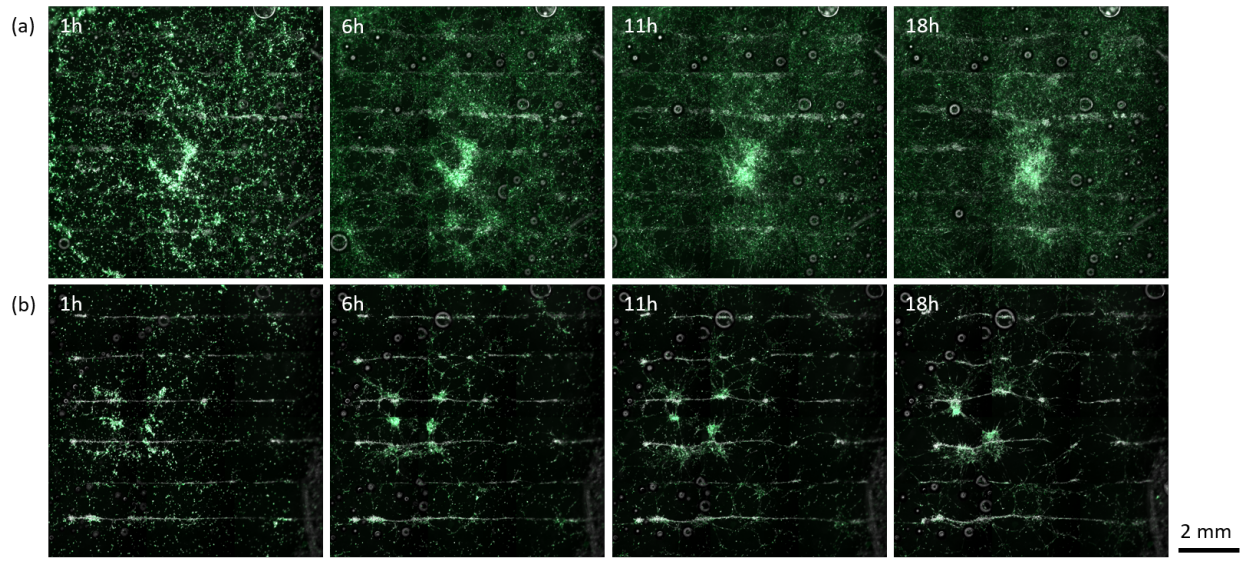

Fig. 4.20. Seeding HBPCs at two concentrations of (a) 134,000 cells/mL and (b) 36,000 cells/mL on the printed line patterns of HUVECs 1, 6, 11, and 18 hours after seeding. HBPCs were stained with PKH67 (green). Images were taken at 2.5x magnification and stitched together due to the limited field of view.

after seeding on printed HUVECs show that both concentrations of PCs are too high and cause the disintegration of the printed HUVEC patterns into several cell clusters (figure 4.20. As expected, the effect of the higher concentration of HBPCs was harsher and caused the aggregation sooner than the lower concentration.

In the following experiment, we lowered the concentration of HBPCs even more and used two HBPC cell suspensions of 17,000 and 8,500 cells/mL for seeding. This time we observed that PCs at the cell density of 17,000 cells/mL behave almost the same way as fibroblasts at their optimal concentration. They attached to the printed HUVEC lines and crawled back and forth but did not disintegrate the printed pattern. As expected, PCs at the lower concentration (8,500 cells/mL) did not disrupt the HUVEC patterns but for quantification purposes and obtaining a higher SNR, we decided to go with the highest concentration that does not cause disintegration of the HUVECs. Therefore, we considered the optimal seeding concentration of HBPCs to be 17,000 cells/mL which is half the optimal seeding concentration for IMR90 cells and that would suggest that HBPCs have a stronger effect than IMR90 cells on HUVECs. The time-lapse of HBPC recruitment over a printed HUVEC line at the optimal seeding concentration over a 19-hour period is shown in figure 4.21.

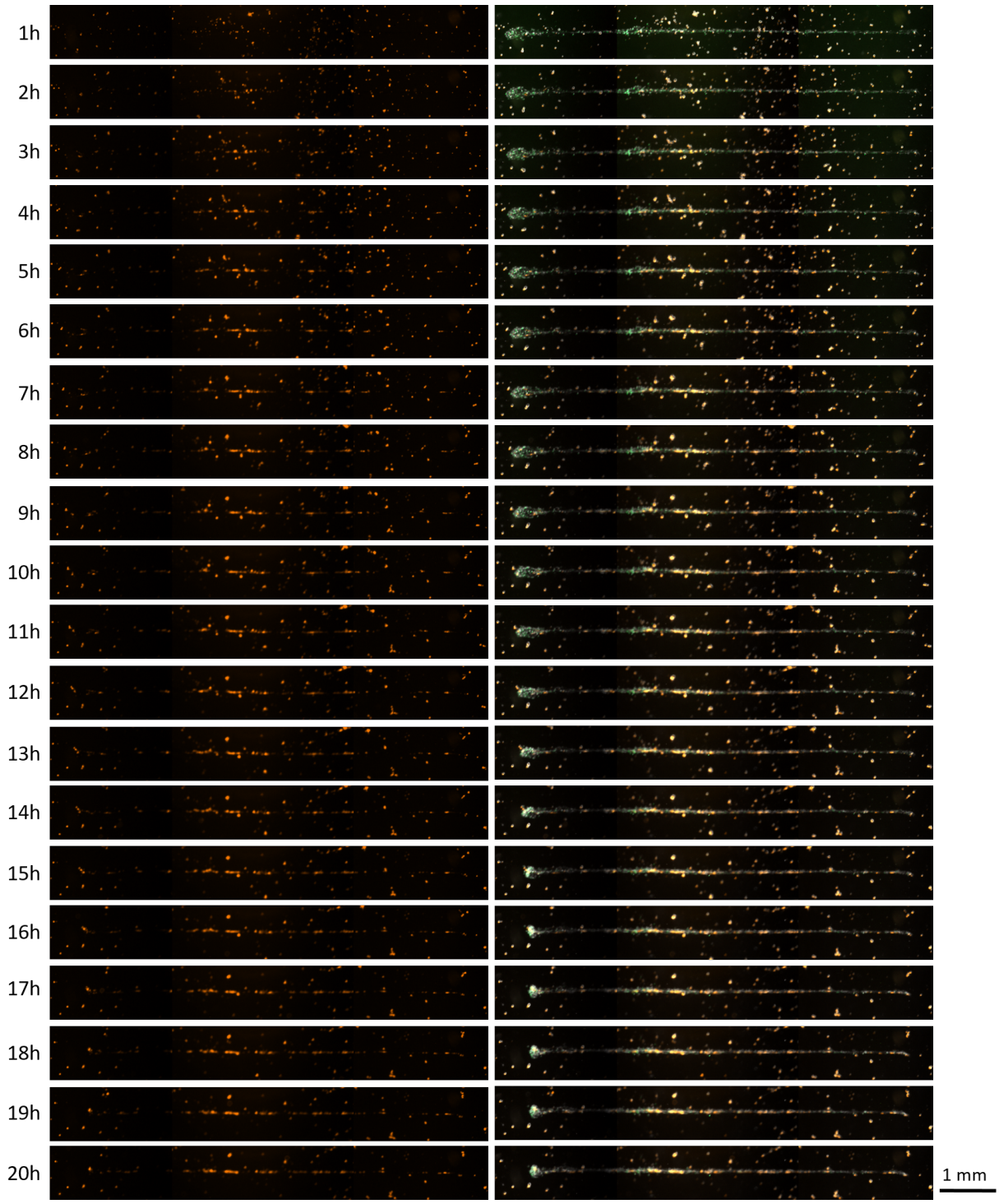

Fig. 4.21. Time lapse of seeding HBPCs at the optimal concentration (17,000 cells/mL) on a printed HUVEC line. Images were taken for 19 hours with a 1-hour time interval. HUVECs and HBPCs were stained with PKH67 (green) and PKH26 (red). Images were taken at 2.5x magnification and stitched together due to the limited field of view.

4.4.3. Quantification of IMR90 and HBPC recruitment on printed patterns of HUVECs on Matrigel substrates

The quantification of cell recruitment was an important goal of this work to help us make objective and precise conclusions and make more informed decisions for the continuation of cell studies. One of the events that we tried to quantify was the back-and-forth crawling of IMR90 cells and HBPCs on the printed HUVEC lines. We developed a cell-tracking MATLAB program to follow the path that the supporting cells take on the HUVEC patterns however this type of quantification turned out to be more complicated than expected. The program could not properly detect the cells that cross past each other or aggregate so it lost track of the cell path. Therefore, we had to come up with another quantification method which is described below.

Over time, the patterned lines of HUVECs recruit IMR90 cells or HBPCs and this effect can be quantified by measuring the pixel intensity of a narrow region that encloses the printed HUVEC line in all frames. The IMR90 recruitment graph in figure 4.22 shows the data for relative pixel intensity over time for all the printed lines in three independent experiments. Therefore, each point on the bars represents the mean of relative intensity over all the printed HUVEC lines for one independent experiment at a particular time point. Due to the insufficient amount of time, we could only perform one independent experiment with HBPCs and the graph in figure 4.23 shows the data for just one independent PC recruitment experiment. Moreover, each point on the bars of this graph represents relative intensity over a single printed HUVEC line at a certain time point. Sample denotes the relative intensity over the HUVEC lines and control indicates the same quantity over the background area around each line. Fibroblasts did not show a significant effect in cell recruitment compared to the background control but the relative intensity of the samples is at all times higher than the control. For HBPC recruitment, we did not do any comparisons between the samples and controls due to insufficient data however, the sample relative intensity is higher than the values for the control at all time points. Both graphs seem to reach a plateau section from a certain point which means that cell recruitment starts rapidly during the first few

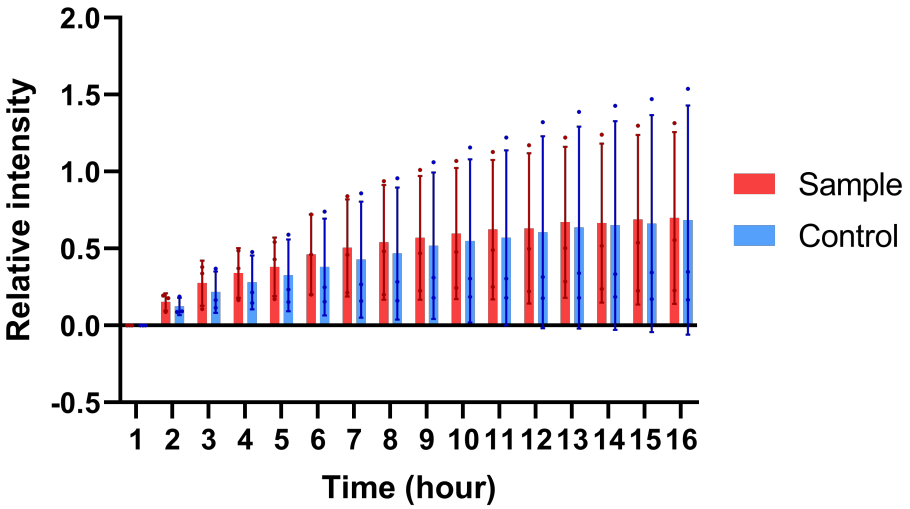

Fig. 4.22. The time-dependent relative pixel intensity of the stained IMR90 cells over a narrow ROI around the printed HUVEC lines. Each point in the triple sets on the bars represents the mean relative pixel intensity of all the samples in one of the three mutually-independent experiments. The data were analyzed by two-way ANOVA and Šidák's test was used for multiple comparisons ($P > 0.05$). Shown are means±SD n=3 with points denoting each individual value.

hours of the experiment and then, gradually slows down and the number of the cells that are attached to the lines becomes stable.

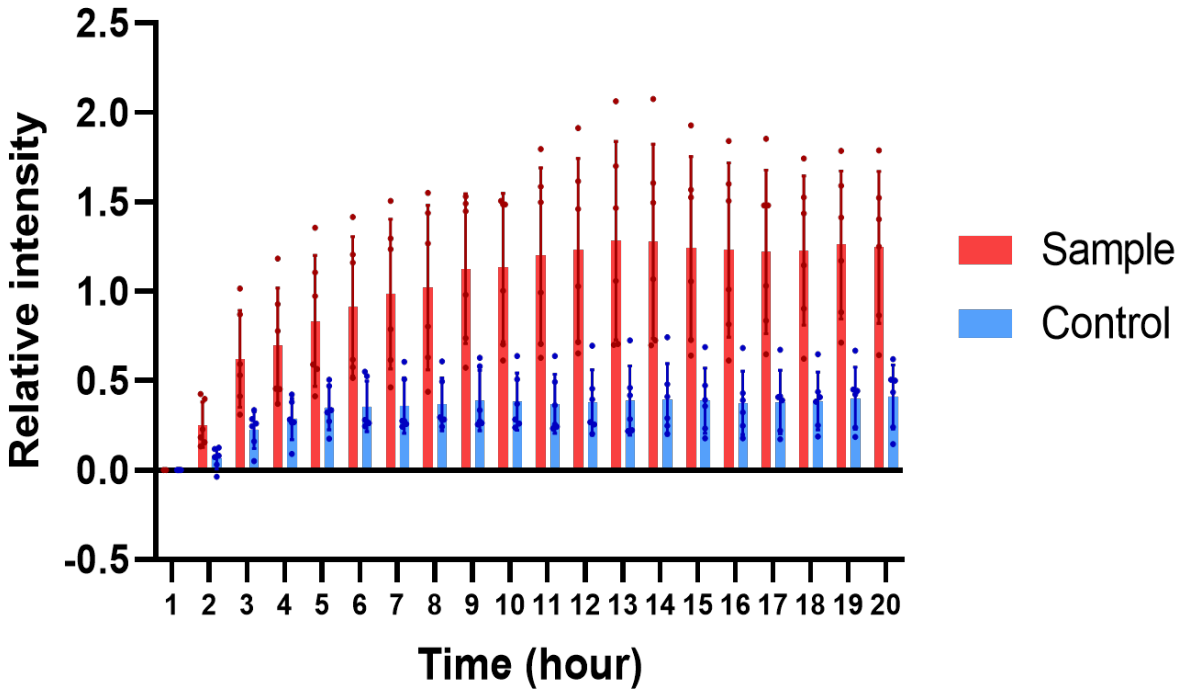

Fig. 4.23. The time-dependent relative pixel intensity of the stained HBPC cells over a narrow ROI around the printed HUVEC lines. The graph shows the inter-sample variability so each point on the bars represents the relative pixel intensity over a single HUVEC line or its background area that was printed in the same experiment. Shown are means±SD n=6 with points denoting each individual value.

Chapter 5

Discussion

In this project, we have developed a horizontal configuration of the previously-introduced vertical LIST technique that allows us to overcome a number of challenges we faced in the past. In the new configuration, we have the possibility of flowing the bioink through the glass capillary at any desired flow rate or flow pattern. As opposed to the vertical LIST, this would allow us to mix the bioink in the tube without withdrawal and reloading by back-and-forth pumping using a syringe pump. This would solve major issues in the process. clogging of the nozzle could be avoided by maintaining a constant flow throughout the experiment; it would prevent accumulation and sedimentation of the cells around the orifice due to gravity as well as thickening of thixotropic biomaterials under static conditions by exploiting their shear-thinning behavior (Mewis, 1979). Furthermore, we experienced that no matter how long the cell suspensions are mixed before the bioink loading step, they will gradually become inhomogeneous in the tube. Therefore, parts of the bioink in the tube will have an excessive cell density while the others might only be filled with the suspension medium. This issue can be overcome by the horizontal LIST by flowing the bioink until the desired cell density is observed above the orifice where the laser produces bioink droplets. On top of that, the horizontal LIST potentially enables high-speed printing of more viscous materials; In the vertical LIST, after printing each droplet, in the place of the deposited bioink volume, an inward convex meniscus of the bioink forms in the glass capillary and as long as the capillary is not refilled with the bioink through the aid of gravity or a syringe pump, it is either not

possible to print droplets or the printed droplets would be non-ideal with undesired shapes and dislocated landing position. This is more of an issue for the viscous materials since their resistance to flow delays the refilling of the glass capillary and complicates printing at high rates. Flow compensation with the aid of a syringe pump is an option however the printing process becomes more and more unstable with higher viscosities and printing rates. Through the use of the horizontal LIST, it is possible to flow the material in the capillary and constantly refill the liquid above the orifice.

We investigated the two flow directions that we called "injection" and "suction" directions. These two directions introduce different conditions to the flow; during injection, the liquid pressure on the syringe pump side is higher than the atmospheric pressure of the free end of the plastic tubing and the capillary orifice. On the other hand, during suction, the liquid pressure gradually decreases as we move from the capillary orifice toward the syringe side. Therefore, besides the effect of the energy and flow rate magnitude, the effect of the direction of the flow on the shape of the printed droplets needs to be investigated. To characterize the horizontal LIST, we avoided the use of our cell suspension bioink due to the non-ideal conditions such as the gradual cell aggregation and loss of homogeneity in the tube as well as the cell accumulation and wetting around the orifice which would considerably complicate the study.

The resolution of the bioprinting methods is determined by the smallest reproducible feature size. According to our data, the printing resolution of the horizontal LIST is in the range of 250-290 µm and it seems that the resolution is somewhat improved during the suction direction. This could be explained by the comparison of the fluid pressure at the orifice and the syringe pump side. With the injection direction, the fluid pressure is higher in the glass capillary compared to the orifice and the flow has a tendency to leak out of the orifice if it overcomes the opposing surface tension force. The bubble formation by the laser beam in the glass capillary above the orifice allows for exceeding the surface tension and with the help of the extra pressure from the syringe pump, the volume of the discharged liquid would increase to some degree. However, we do not have such force during the suction of the

bioink since the pressure in the glass capillary and the tube is lower than the atmospheric pressure of the orifice.

According to our data, printing at high laser energies has a detrimental effect on droplet circularity. It is well known that with increasing the absorbed laser energy in the bioink, larger bubbles will form (Evans et al., 2008; Dou et al., 2021) and that would create a stronger driving force for droplet ejection. The larger force increases the velocity of the tip of the forming liquid jet and upon landing on the receiver substrate, the detached droplet is more likely to splash and divide into several satellite droplets (Ng et al., 2022). As a result, the accuracy and quality of the printed pattern will be affected and that would explain our observations on the droplet circularity. There was no clear pattern in the droplet circularity with variations of bioink flow rate which leads us to believe that there needs to be a larger group of samples to deduce a correlation between these two variables or more simply, the bioink flow rate might not have any noticeable effect on the droplet circularity and after increasing our sample size, the observed differences might become insignificant.

As mentioned earlier, the bioink is much more likely to leak through the glass capillary orifice during the flow injection due to the higher fluid pressure in the tube compared to the orifice. On the other hand, if the flow rate is too high during the flow suction, we would introduce air bubbles in the bioink through the orifice that will separate the bioink into several segments in the tube. We have experienced an increased incidence of such issues in both flow directions at flow rates above 300 µL/min, especially with the cell suspension bioink in which the cells introduce non-ideal and non-uniform conditions to the flow (Zhang et al., 2017). Therefore we tested the jet angle at flow rates equivalent to 15x (90 µL/min) and 50x (300 µL/min) multiples of the bioink printing rate and did not go further than 300 µL/min. The measurements showed that despite the flow rate and flow direction, the jet angel mostly remains in the $0°\pm2°$ range and this slight sideways slope would not noticeably diverge the droplet from its patterned landing position and affect the overall printing quality.

Before conducting any cell studies with the newly developed horizontal LIST, its cytocompatibility needs to be validated for cell printing applications. The HUVEC viability

measurements showed no significant difference between the viability rate of the printed and the manually-pipetted cells over three days which projects the potential of this technique in cell printing applications. However, these promising results are not surprising since it has already been shown that compared to the manually-pipetted ECs, the thermal stress that the cells are exposed to during the bioprinting process will eventually aid them in survival and angiogenesis due to the expression of growth factors in response to the heat shock (Solis et al., 2019).

The droplet ejection threshold for our cell-free bioink was found to be about 30 µJ in the horizontal LIST and at 40 µJ, we printed relatively smaller and rounder droplets leading to a better resolution compared with 60 µJ and 80 µJ. It has been shown that the laser energy threshold for droplet ejection of cell suspension bioinks is higher than the cell-free bioinks (Zhang et al., 2017). Therefore, to print our cell suspension bioink, we would get a comparable droplet shape and quality with a slightly higher energy level than the optimal 40 µJ for our cell-free bioink. We found that the optimal energy level for our cell printing experiments would be in the 60-80 µJ range.

We observed in our cell studies that IMR90 cells would proliferate and spread over the fibrin substrates however a round clustered morphology would be developed on Matrigel. These observations are in accordance with the previous findings that confirm the fibroblast migration (Serban et al., 2008) or aggregation (Brown et al., 1993) on the respective gels in our experiments. However, besides the fact that Matrigel is known for supporting endothelial cord formations (Kuzuya and Kinsella, 1994), our group discovered that with the inclusion of thrombin in Matrigel substrate formulation, it is possible to prevent the migration of HUVECs and the disintegration of the printed pattern (Orimi et al., 2022). Therefore, we continued the cell studies with Matrigel and incorporated fibroblasts as a secondary cell type. Furthermore, the Allura red dye did not show any significant effect on the viability of fibroblasts. Considering the fact that it is a food dye, the results do not come as a surprise.

In the fibroblast printing experiments, we once again observed the clustered morphology after a few days on Matrigel. Even in the presence of the printed HUVEC lines, the printed

IMR90 cells not only showed no change in their behavior but also dragged these HUVEC cord-like structures and made them aggregate into cell clusters along with themselves. So printing fibroblasts at a high cell density on top of or in parallel to the patterned lines of HUVECs on Matrigel seemed not to be the right choice for their incorporation into our construct. The change of our gel substrate into fibrin could also be examined since fibroblast-derived growth factors have been shown to support lumen formation of HUVECs in fibrin gels (Nakatsu et al., 2003). However, according to our data, HUVECs spread and migrate from their initial position 2 days after printing on fibrin (Orimi et al., 2022), and therefore, we could not have guided angiogenesis and control over the position of the capillary network.

The next way that we tried to incorporate these cells into our printed HUVEC cords was to seed the IMR90 cells at a lower cell density compared to cell printing. At the optimal IMR90 cell seeding density, we observed gradual fibroblast recruitment by the HUVEC lines and subsequently the movement of fibroblasts on these endothelial cords. For the inclusion of PCs, we started with the same cell seeding method instead of printing at a high cell density. At the optimal HBPC cell seeding density which was half of that of IMR90 cells, we observed EC-PC interactions that were similar to the EC-fibroblast interactions. Although there have been several published studies on the symbiotic relationship of ECs with fibroblasts and PCs (Darland et al., 2003; Newman et al., 2011), to our knowledge, such cell-cell interactions have not been reported previously. We suppose that this is due to the mutual expression of signaling molecules resulting from the presence of these pair of cell types in combination.

In cell recruitment studies for both supporting cell types, there is a need for more individual experiments; for fibroblasts, it can be seen that one particular experiment did not go as well as the other two and it negatively affected the results and we believe that with the inclusion of more mutually-independent experiments in the graph, this particular experiment will end up being an outlier or not having a strong effect on the overall analysis. For the completion of the PC recruitment graph, there need to be at least two more independent experiments to confirm the EC-PC interaction effect. Notwithstanding the lack of enough data,

our graphs show promising results highlighting the increasing population of these secondary cell types on the HUVEC cord-like structures over time.

Chapter 6

Future works

We performed a detailed study to examine the effects of laser energy and bioink flow on the quality of the printed droplets. However, there are other variables in play that are worthy of being studied but were not investigated in this project including the bioink viscosity and printing rate. Since horizontal LIST enables flow compensation unlike the vertical LIST, it is worthwhile to perform another study to derive the viscosity range that this configuration can potentially print at different printing rates and compare the capabilities of this technique with LIFT or other bioprinting techniques. Furthermore, the volume and the contact angle of the printed droplets are two other dependent variables that could be monitored as well as the droplet circularity and radius.

To improve our printing resolution, we can do several adjustments to the printing setup. The size of the orifice which was 200 µm in our study, can be reduced to decrease the ejected droplet volume. The shape of the orifice could also be an important factor in the shape of the landed droplet that could be investigated. Another method that could affect the resolution is the surface treatment of the orifice using a coating material. This would change the contact angle and shape of the bioink jet so the bioink volume is likely to change as well.

Besides the technical properties of the bioprinting method, printing resolution depends on the physiochemical properties of the bioink and the surface properties of the receiver substrate. These factors show their effect on the contact angle of the printed droplets. Contact angle increases as the interfacial tension between the bioink and the substrate grows

(Miri et al., 2019); therefore, by changing the bioink formulation or coating the surface of the receiver substrate, it is possible to increase the contact angle and further improve the printing resolution.

With our laser source, we can have a range of laser frequencies up to 30 Hz that can be successfully employed to print our bioink. Considering the average droplet volume in LIST Ebrahimi Orimi et al. (2020), our maximum printing rate would be about 9 µL/min. However, using long capillaries with several distanced orifices could increase our maximum printing speed depending on the number of the orifices. The laser beam could be directed to aim at all the positions above each orifice through the use of precise beam-steering optical devices called galvanometer optical scanners (a.k.a. Galvos, Galvo scanners, or galvanomaters). We could even install several capillaries to benefit from the increased printing rate as well as the possibility of loading several bioinks that could be simultaneously printed. This would also be an opportunity to print multiple cell types or ECM-mimicking biomaterials at the same time.

This configuration is still dealing with a number of challenges but has a lot of potentials to become more user-friendly. There is an occasional leaking of the bioink through the orifice, especially with the cell suspension bioink. Although the cell suspension is mixed properly through trituration before the bioink loading step, the cells tend to stick together and form cell clusters that move in groups. As a result, the bioink loses its homogeneity which leads to variable flow conditions above the orifice that could cause the occasional leaking. By surface treatment of the material, we can increase the interfacial tension between the bioink and the glass capillary surface and therefore avoid or reduce these incidents. Additionally, the whole setup would become much less bulky and therefore easier to use with the use of optical fibers that would eliminate several optical elements that take up a lot of space.

Furthermore, the cell suspension bioink is kept at non-biological conditions during the print which could be fixed by installing an apparatus that controls the temperature and CO2 content of the environment. By doing so, in addition to making the setup more biocompatible, there would be ample amount of time for the printing process to finish. That

will also reduce the inter-sample variation in each individual experiment; the cells on the samples that were prepared in the beginning were exposed to non-biological conditions much shorter than the last samples. This duration would affect the viability and the function of the printed cells on each sample and with environmental condition-controlling systems, this source of inter-sample variation would be omitted.

We observed strong cell aggregation in the bioink with both IMR90 cells and HBPCs that hindered their printing by severe nozzle clogging. The use of more viscous materials to delay the cells from causing gradual inhomogeneity in the cell suspension or formulations that contain gentle cell dissociation reagents like chelating agents (e.g. EDTA) or enzymes (e.g. Asaccumax or Accutase) are two options that could be investigated.

There could be improvements in the ECM-mimicking hydrogel in our printed constructs. Although Matrigel was proven to be beneficial in our work due to its pro-angiogenic properties, it comes from murine tumor tissue which is not a desirable source, especially for clinical studies (Kaur et al., 2021). Moreover, the mechanical properties of the hydrogel substrate have been shown to affect cell proliferation, migration, gene expression and overall cell behavior (Brandl et al., 2007). Therefore, rheological characterization of our biomaterials is crucial in our application as it was shown by Koch et al. that a diluted gel substrate resulted in convincing lumen formation by ECs (Benning et al., 2018; Koch et al., 2021). Also, in order to allow the hydrogel matrix to better mimic the 3D environment of the cells in the native ECM, manual deposition of multiple hydrogel layers in between the printed cell layers could be done.

The very next step in this project is to treat the samples with the anti-angiogenic factor, bone morphogenetic protein 9 (BMP9), that has been shown by our group to improve tubulogenesis of ECs (Orimi et al., 2022). The investigation of the accumulated effects of stabilizing and maturation-inducing secretions from the supporting cell types and BMP9 followed by z-stack imaging to monitor the lumen formation would be an intriguing study that was not done due to the limited amount of time. Moreover, the fluorescent images of the supporting cell recruitment by the HUVEC lines could be analyzed to count the number

of attached cells over time. The pixel intensity over our ROI could be divided by the average pixel intensity of a single fibroblast or PC to give a gradual increase in the number of recruited cells.

Fibroblasts and PCs were incorporated in our printed HUVEC samples due to their beneficial relationship with ECs that would supposedly lead to better stability and functionality of the capillary-like structures. However, due to the limited time, these effects were not studied here. The stability of our HUVEC samples on Matrigel could be analyzed in the presence and the absence of the secondary cell types to see if the inclusion of a perivascular cell could preserve the printed cord-like formations for longer. Furthermore, in the native tissue, larger vessels are coated with layers of SMCs so, the addition of this cell type to our construct could also be studied. Besides, multiple supporting cell types could be incorporated altogether in our EC sample and their accumulated effect could be analyzed.

One of the potentials of this project is to test our printed patterns of micro-capillaries on animal models and monitor the integration of the printed construct. It has been a long-term goal of regenerative medicine to either transplant the biofabricated tissue constructs or directly perform in situ bioprinting. In the future, there could be the possibility to alleviate the shortage of organs for transplantation and improve wound healing. Furthermore, the use of iPSC-ECs instead of HUVECs as the cell source for our printed constructs paves the way for personalized medicine and transplantation with improved immunologic tolerance (de Almeida et al., 2014).

Chapter 7

Conclusion

Although improved in comparison with LIFT in some aspects such as scalability and material printability, our previously-introduced vertical configuration of LIST presented a number of challenges that were addressed in this study. The new configuration of LIST was set up by positioning a horizontal glass capillary in front of the laser beam and printing the loaded bioink droplets through a small orifice in the capillary wall facing the receiver substrate. The horizontal LIST was characterized to assess the effects of the printing parameters on the final pattern shape and was validated for its cytocompatibility. We have found a method for the successful incorporation of IMR90 cells and HBPCs and observed the interactive behavior of these perivascular cells and HUVECs. The added fibroblasts and PCs gradually get recruited on the cord-like formations of ECs in the first few hours of cell seeding and move along the patterned lines of HUVECs.

These bioprinted multi-cell microcapillaries mimic the structure of the capillary bed in the native tissue more closely and have the potential to be incorporated along with the parenchymal cells in the fabricated thick tissue constructs and serve as a drug screening model or as a solution for the shortage of the transplantable organs in the future.

References

Abbott, A. (2003). Cell culture: biology's new dimension. *Nature*, 424(6951):870–873.

Aguirre, A., Planell, J., and Engel, E. (2010). Dynamics of bone marrow-derived endothelial progenitor cell/mesenchymal stem cell interaction in co-culture and its implications in angiogenesis. *Biochemical and biophysical research communications*, 400(2):284–291.

Alajati, A., Laib, A. M., Weber, H., Boos, A. M., Bartol, A., Ikenberg, K., Korff, T., Zentgraf, H., Obodozie, C., Graeser, R., et al. (2008). Spheroid-based engineering of a human vasculature in mice. *Nature methods*, 5(5):439–445.

Ando, K., Fukuhara, S., Izumi, N., Nakajima, H., Fukui, H., Kelsh, R. N., and Mochizuki, N. (2016). Clarification of mural cell coverage of vascular endothelial cells by live imaging of zebrafish. *Development*, 143(8):1328–1339.

Armulik, A., Genové, G., and Betsholtz, C. (2011). Pericytes: developmental, physiological, and pathological perspectives, problems, and promises. *Developmental cell*, 21(2):193–215.

Atala, A., Bauer, S. B., Soker, S., Yoo, J. J., and Retik, A. B. (2006). Tissue-engineered autologous bladders for patients needing cystoplasty. *The lancet*, 367(9518):1241–1246.

Attarwala, H. (2010). Tgn1412: from discovery to disaster. *Journal of Young Pharmacists*, 2(3):332–336.

Au, P., Tam, J., Fukumura, D., and Jain, R. K. (2008). Bone marrow–derived mesenchymal stem cells facilitate engineering of long-lasting functional vasculature. *Blood, The Journal of the American Society of Hematology*, 111(9):4551–4558.

Bancroft, G. N., Sikavitsas, V. I., and Mikos, A. G. (2003). Design of a flow perfusion bioreactor system for bone tissue-engineering applications. *Tissue engineering*, 9(3):549–554.

Barron, J., Wu, P., Ladouceur, H., and Ringeisen, B. (2004). Biological laser printing: a novel technique for creating heterogeneous 3-dimensional cell patterns. *Biomedical microdevices*, 6(2):139–147.

Barrs, R. W., Jia, J., Silver, S. E., Yost, M., and Mei, Y. (2020). Biomaterials for bioprinting microvasculature. *Chemical reviews*, 120(19):10887–10949.

Ben-Shaul, S., Landau, S., Merdler, U., and Levenberg, S. (2019). Mature vessel networks in engineered tissue promote graft–host anastomosis and prevent graft thrombosis. *Proceedings of the National Academy of Sciences*, 116(8):2955–2960.

Benning, L., Gutzweiler, L., Tröndle, K., Riba, J., Zengerle, R., Koltay, P., Zimmermann, S., Stark, G. B., and Finkenzeller, G. (2018). Assessment of hydrogels for bioprinting of endothelial cells. *Journal of Biomedical Materials Research Part A*, 106(4):935–947.

Bertassoni, L. E., Cecconi, M., Manoharan, V., Nikkhah, M., Hjortnaes, J., Cristino, A. L., Barabaschi, G., Demarchi, D., Dokmeci, M. R., Yang, Y., et al. (2014). Hydrogel bioprinted microchannel networks for vascularization of tissue engineering constructs. *Lab on a Chip*, 14(13):2202–2211.

Black, A. F., Berthod, F., L'Heureux, N., Germain, L., and Auger, F. A. (1998). In vitro reconstruction of a human capillary-like network in a tissue-engineered skin equivalent. *The FASEB journal*, 12(13):1331–1340.

Blanco, R. and Gerhardt, H. (2013). Vegf and notch in tip and stalk cell selection. *Cold Spring Harbor perspectives in medicine*, 3(1):a006569.

Borselli, C., Oliviero, O., Battista, S., Ambrosio, L., and Netti, P. A. (2007). Induction of directional sprouting angiogenesis by matrix gradients. *Journal of Biomedical Materials Research Part A*, 80(2):297–305.

Bourget, J.-M., Kérourédan, O., Medina, M., Rémy, M., Thébaud, N. B., Bareille, R., Chassande, O., Amédée, J., Catros, S., and Devillard, R. (2016). Patterning of endothelial

cells and mesenchymal stem cells by laser-assisted bioprinting to study cell migration. *BioMed research international*, 2016.

Brandl, F., Sommer, F., and Goepferich, A. (2007). Rational design of hydrogels for tissue engineering: impact of physical factors on cell behavior. *Biomaterials*, 28(2):134–146.

Brown, L. F., Lanir, N., McDonagh, J., Tognazzi, K., Dvorak, A. M., and Dvorak, H. F. (1993). Fibroblast migration in fibrin gel matrices. *The American journal of pathology*, 142(1):273.

Caduff, J., Fischer, L., and Burri, P. H. (1986). Scanning electron microscope study of the developing microvasculature in the postnatal rat lung. *The Anatomical Record*, 216(2):154–164.

Calvert, P. (2001). Inkjet printing for materials and devices. *Chemistry of materials*, 13(10):3299–3305.

Campbell, K. T., Stilhano, R. S., and Silva, E. A. (2018). Enzymatically degradable alginate hydrogel systems to deliver endothelial progenitor cells for potential revasculature applications. *Biomaterials*, 179:109–121.

Chang, R., Nam, J., and Sun, W. (2008). Effects of dispensing pressure and nozzle diameter on cell survival from solid freeform fabrication–based direct cell writing. *Tissue Engineering Part A*, 14(1):41–48.

Chen, X., Aledia, A. S., Ghajar, C. M., Griffith, C. K., Putnam, A. J., Hughes, C. C., and George, S. C. (2009). Prevascularization of a fibrin-based tissue construct accelerates the formation of functional anastomosis with host vasculature. *Tissue Engineering Part A*, 15(6):1363–1371.

Compton, C. C., Butler, C. E., Yannas, I. V., Warland, G., and Orgill, D. P. (1998). Organized skin structure is regenerated in vivo from collagen-gag matrices seeded with autologous keratinocytes. *Journal of investigative dermatology*, 110(6):908–916.

Cui, X. and Boland, T. (2009). Human microvasculature fabrication using thermal inkjet printing technology. *Biomaterials*, 30(31):6221–6227.

Cui, X., Boland, T., DD'Lima, D., and K Lotz, M. (2012). Thermal inkjet printing in tissue engineering and regenerative medicine. *Recent patents on drug delivery & formulation*, 6(2):149–155.

Cui, X., Dean, D., Ruggeri, Z. M., and Boland, T. (2010). Cell damage evaluation of thermal inkjet printed chinese hamster ovary cells. *Biotechnology and bioengineering*, 106(6):963–969.

Da Silva, I. R. F. and Frontera, J. A. (2015). Worldwide barriers to organ donation. *JAMA neurology*, 72(1):112–118.

Darland, D., Massingham, L., Smith, S., Piek, E., Saint-Geniez, M., and D'amore, P. (2003). Pericyte production of cell-associated vegf is differentiation-dependent and is associated with endothelial survival. *Developmental biology*, 264(1):275–288.

de Almeida, P., Meyer, E. H., Kooreman, N. G., Diecke, S., Dey, D., Sanchez-Freire, V., Hu, S., Ebert, A., Odegaard, J., Mordwinkin, N. M., et al. (2014). Transplanted terminally differentiated induced pluripotent stem cells are accepted by immune mechanisms similar to self-tolerance. *Nature communications*, 5(1):1–12.

Di Carlo, S. E., Peduto, L., et al. (2018). The perivascular origin of pathological fibroblasts. *The Journal of clinical investigation*, 128(1):54–63.

Dou, C., Perez, V., Qu, J., Tsin, A., Xu, B., and Li, J. (2021). A state-of-the-art review of laser-assisted bioprinting and its future research trends. *ChemBioEng Reviews*, 8(5):517–534.

Ebrahimi Orimi, H., Hosseini Kolkooh, S. S., Hooker, E., Narayanswamy, S., Larrivée, B., and Boutopoulos, C. (2020). Drop-on-demand cell bioprinting via laser induced side transfer (list). *Scientific reports*, 10(1):1–9.

Evans, R., Camacho-López, S., Pérez-Gutiérrez, F., and Aguilar, G. (2008). Pump-probe imaging of nanosecond laser-induced bubbles in agar gel. *Optics Express*, 16(10):7481–7492.

Fitzgerald, K. A., Malhotra, M., Curtin, C. M., O'Brien, F. J., and O'Driscoll, C. M. (2015). Life in 3d is never flat: 3d models to optimise drug delivery. *Journal of controlled release*,

215:39–54.

Fleischer, S., Tavakol, D. N., and Vunjak-Novakovic, G. (2020). From arteries to capillaries: approaches to engineering human vasculature. *Advanced functional materials*, 30(37):1910811.

Gerhardt, H., Golding, M., Fruttiger, M., Ruhrberg, C., Lundkvist, A., Abramsson, A., Jeltsch, M., Mitchell, C., Alitalo, K., Shima, D., et al. (2003). Vegf guides angiogenic sprouting utilizing endothelial tip cell filopodia. *The Journal of cell biology*, 161(6):1163–1177.

Grebenyuk, S. and Ranga, A. (2019). Engineering organoid vascularization. *Frontiers in bioengineering and biotechnology*, 7:39.

Grellier, M., Bordenave, L., and Amedee, J. (2009). Cell-to-cell communication between osteogenic and endothelial lineages: implications for tissue engineering. *Trends in biotechnology*, 27(10):562–571.

Gruene, M., Pflaum, M., Hess, C., Diamantouros, S., Schlie, S., Deiwick, A., Koch, L., Wilhelmi, M., Jockenhoevel, S., Haverich, A., et al. (2011). Laser printing of three-dimensional multicellular arrays for studies of cell–cell and cell–environment interactions. *Tissue Engineering Part C: Methods*, 17(10):973–982.

Guidolin, D., Albertin, G., Sorato, E., Oselladore, B., Mascarin, A., and Ribatti, D. (2009). Mathematical modeling of the capillary-like pattern generated by adrenomedullin-treated human vascular endothelial cells in vitro. *Developmental Dynamics: An Official Publication of the American Association of Anatomists*, 238(8):1951–1963.

Guillemot, F., Souquet, A., Catros, S., and Guillotin, B. (2010). Laser-assisted cell printing: principle, physical parameters versus cell fate and perspectives in tissue engineering. *Nanomedicine*, 5(3):507–515.

Guillotin, B., Souquet, A., Catros, S., Duocastella, M., Pippenger, B., Bellance, S., Bareille, R., Rémy, M., Bordenave, L., Amédée, J., et al. (2010). Laser assisted bioprinting of engineered tissue with high cell density and microscale organization. *Biomaterials*, 31(28):7250–7256.

Gutzweiler, L., Kartmann, S., Troendle, K., Benning, L., Finkenzeller, G., Zengerle, R., Koltay, P., Stark, G. B., and Zimmermann, S. (2017). Large scale production and controlled deposition of single huvec spheroids for bioprinting applications. *Biofabrication*, 9(2):025027.

Güven, S., Mehrkens, A., Saxer, F., Schaefer, D. J., Martinetti, R., Martin, I., and Scherberich, A. (2011). Engineering of large osteogenic grafts with rapid engraftment capacity using mesenchymal and endothelial progenitors from human adipose tissue. *Biomaterials*, 32(25):5801–5809.

Harrison, B. S., Eberli, D., Lee, S. J., Atala, A., and Yoo, J. J. (2007). Oxygen producing biomaterials for tissue regeneration. *Biomaterials*, 28(31):4628–4634.

JA, R. B. K. H. B. (2004). Krizman db chrisey db jackman s. auyeung ryc spargo bj laser printing of pluripotent embryonal carcinoma cells. *Tissue Eng*, 10:483.

Jain, R. K. (1999). Transport of molecules, particles, and cells in solid tumors. *Annual review of biomedical engineering*, 1(1):241–263.

Jakobsson, L., Franco, C. A., Bentley, K., Collins, R. T., Ponsioen, B., Aspalter, I. M., Rosewell, I., Busse, M., Thurston, G., Medvinsky, A., et al. (2010). Endothelial cells dynamically compete for the tip cell position during angiogenic sprouting. *Nature cell biology*, 12(10):943–953.

Jungebluth, P., Alici, E., Baiguera, S., Blomberg, P., Bozóky, B., Crowley, C., Einarsson, O., Gudbjartsson, T., Le Guyader, S., Henriksson, G., et al. (2011). Retracted: tracheobronchial transplantation with a stem-cell-seeded bioartificial nanocomposite: a proof-of-concept study.

Kaur, S., Kaur, I., Rawal, P., Tripathi, D. M., and Vasudevan, A. (2021). Non-matrigel scaffolds for organoid cultures. *Cancer Letters*, 504:58–66.

Kérourédan, O., Bourget, J.-M., Rémy, M., Crauste-Manciet, S., Kalisky, J., Catros, S., Thébaud, N. B., and Devillard, R. (2019). Micropatterning of endothelial cells to create a capillary-like network with defined architecture by laser-assisted bioprinting. *Journal of Materials Science: Materials in Medicine*, 30(2):1–12.

Koch, L., Deiwick, A., and Chichkov, B. (2021). Capillary-like formations of endothelial cells in defined patterns generated by laser bioprinting. *Micromachines*, 12(12):1538.

Kolesky, D. B., Homan, K. A., Skylar-Scott, M. A., and Lewis, J. A. (2016). Three-dimensional bioprinting of thick vascularized tissues. *Proceedings of the national academy of sciences*, 113(12):3179–3184.

Kolesky, D. B., Truby, R. L., Gladman, A. S., Busbee, T. A., Homan, K. A., and Lewis, J. A. (2014). 3d bioprinting of vascularized, heterogeneous cell-laden tissue constructs. *Advanced materials*, 26(19):3124–3130.

Koob, S., Torio-Padron, N., Stark, G. B., Hannig, C., Stankovic, Z., and Finkenzeller, G. (2011). Bone formation and neovascularization mediated by mesenchymal stem cells and endothelial cells in critical-sized calvarial defects. *Tissue Engineering Part A*, 17(3-4):311–321.

Korff, T., Kimmina, S., MARTINY-BARON, G., and Augustin, H. G. (2001). Blood vessel maturation in a 3-dimensional spheroidal coculture model: direct contact with smooth muscle cells regulates endothelial cell quiescence and abrogates vegf responsiveness. *The FASEB journal*, 15(2):447–457.

Kuzuya, M. and Kinsella, J. L. (1994). Reorganization of endothelial cord-like structures on basement membrane complex (matrigel): involvement of transforming growth factor β1. *Journal of cellular physiology*, 161(2):267–276.

Lammert, E., Cleaver, O., and Melton, D. (2001). Induction of pancreatic differentiation by signals from blood vessels. *Science*, 294(5542):564–567.

Lammert, E., Cleaver, O., and Melton, D. (2003). Role of endothelial cells in early pancreas and liver development. *Mechanisms of development*, 120(1):59–64.

Lee, V. K., Lanzi, A. M., Ngo, H., Yoo, S.-S., Vincent, P. A., and Dai, G. (2014). Generation of multi-scale vascular network system within 3d hydrogel using 3d bio-printing technology. *Cellular and molecular bioengineering*, 7(3):460–472.

Lee, W., Lee, V., Polio, S., Keegan, P., Lee, J.-H., Fischer, K., Park, J.-K., and Yoo, S.-S. (2010). On-demand three-dimensional freeform fabrication of multi-layered hydrogel

scaffold with fluidic channels. *Biotechnology and bioengineering*, 105(6):1178–1186.

Lee, Y.-J., Lee, H.-J., Choi, S.-h., Jin, Y. B., An, H. J., Kang, J.-H., Yoon, S. S., and Lee, Y.-S. (2012). Soluble hspb1 regulates vegf-mediated angiogenesis through their direct interaction. *Angiogenesis*, 15(2):229–242.

Li, X., Liu, B., Pei, B., Chen, J., Zhou, D., Peng, J., Zhang, X., Jia, W., and Xu, T. (2020). Inkjet bioprinting of biomaterials. *Chemical Reviews*, 120(19):10793–10833.

Lin, A., Peiris, N. J., Dhaliwal, H., Hakim, M., Li, W., Ganesh, S., Ramaswamy, Y., Patel, S., and Misra, A. (2021). Mural cells: Potential therapeutic targets to bridge cardiovascular disease and neurodegeneration. *Cells*, 10(3):593.

Lin, Y., Huang, G., Huang, Y., Tzeng, T.-R. J., and Chrisey, D. (2010). Effect of laser fluence in laser-assisted direct writing of human colon cancer cell. *Rapid Prototyping Journal*.

Lin, Y., Huang, Y., and Chrisey, D. B. (2009). Droplet formation in matrix-assisted pulsed-laser evaporation direct writing of glycerol-water solution. *Journal of Applied Physics*, 105(9):093111.

MacDougall, J. and McCabe, M. (1967). Diffusion coefficient of oxygen through tissues. *Nature*, 215(5106):1173–1174.

Malda, J., Visser, J., Melchels, F. P., Jüngst, T., Hennink, W. E., Dhert, W. J., Groll, J., and Hutmacher, D. W. (2013). 25th anniversary article: engineering hydrogels for biofabrication. *Advanced materials*, 25(36):5011–5028.

Manning, F. J., Swartz, M., et al. (1995). Review of the fialuridine (fiau) clinical trials.

Mazurek, R., Dave, J. M., Chandran, R. R., Misra, A., Sheikh, A. Q., and Greif, D. M. (2017). Vascular cells in blood vessel wall development and disease. *Advances in Pharmacology*, 78:323–350.

McDonald, D. M. and Choyke, P. L. (2003). Imaging of angiogenesis: from microscope to clinic. *Nature medicine*, 9(6):713–725.

Mewis, J. (1979). Thixotropy-a general review. *Journal of Non-Newtonian Fluid Mechanics*, 6(1):1–20.

Miller, J. S., Stevens, K. R., Yang, M. T., Baker, B. M., Nguyen, D.-H. T., Cohen, D. M., Toro, E., Chen, A. A., Galie, P. A., Yu, X., et al. (2012). Rapid casting of patterned vascular networks for perfusable engineered three-dimensional tissues. *Nature materials*, 11(9):768–774.

Miri, A. K., Mirzaee, I., Hassan, S., Oskui, S. M., Nieto, D., Khademhosseini, A., and Zhang, Y. S. (2019). Effective bioprinting resolution in tissue model fabrication. *Lab on a Chip*, 19(11).

Moore, N. (2016). Lessons from the fatal french study bia-10-2474.

Mori, N., Morimoto, Y., and Takeuchi, S. (2017). Skin integrated with perfusable vascular channels on a chip. *Biomaterials*, 116:48–56.

Murphy, S. V. and Atala, A. (2014). 3d bioprinting of tissues and organs. *Nature biotechnology*, 32(8):773–785.

Nakamura, M., Kobayashi, A., Takagi, F., Watanabe, A., Hiruma, Y., Ohuchi, K., Iwasaki, Y., Horie, M., Morita, I., and Takatani, S. (2005). Biocompatible inkjet printing technique for designed seeding of individual living cells. *Tissue engineering*, 11(11-12):1658–1666.

Nakatsu, M. N., Sainson, R. C., Aoto, J. N., Taylor, K. L., Aitkenhead, M., Pérez-del Pulgar, S., Carpenter, P. M., and Hughes, C. C. (2003). Angiogenic sprouting and capillary lumen formation modeled by human umbilical vein endothelial cells (huvec) in fibrin gels: the role of fibroblasts and angiopoietin-1. *Microvascular research*, 66(2):102–112.

Newman, A. C., Nakatsu, M. N., Chou, W., Gershon, P. D., and Hughes, C. C. (2011). The requirement for fibroblasts in angiogenesis: fibroblast-derived matrix proteins are essential for endothelial cell lumen formation. *Molecular biology of the cell*, 22(20):3791–3800.

Ng, W. L., Huang, X., Shkolnikov, V., Goh, G. L., Suntornnond, R., and Yeong, W. Y. (2022). Controlling droplet impact velocity and droplet volume: Key factors to achieving high cell viability in sub-nanoliter droplet-based bioprinting. *International Journal of Bioprinting*, 8(1).

Orimi, H. E., Hooker, E., Narayanswamy, S., Larrivée, B., and Boutopoulos, C. (2022). Spatially guided endothelial tubulogenesis by laser-induced side transfer (list) bioprinting

of huvecs. *Bioprinting*, 28:e00240.

Ovsianikov, A., Gruene, M., Pflaum, M., Koch, L., Maiorana, F., Wilhelmi, M., Haverich, A., and Chichkov, B. (2010). Laser printing of cells into 3d scaffolds. *Biofabrication*, 2(1):014104.

Ozbolat, I. T. and Hospodiuk, M. (2016). Current advances and future perspectives in extrusion-based bioprinting. *Biomaterials*, 76:321–343.

Park, J.-U., Hardy, M., Kang, S. J., Barton, K., Adair, K., Lee, C. Y., Strano, M. S., Alleyne, A. G., Georgiadis, J. G., Ferreira, P. M., et al. (2007). High-resolution electrohydrodynamic jet printing. *Nature materials*, 6(10):782–789.

Pirlo, R. K., Wu, P., Liu, J., and Ringeisen, B. (2012). Plga/hydrogel biopapers as a stackable substrate for printing huvec networks via biolp™. *Biotechnology and bioengineering*, 109(1):262–273.

Polykandriotis, E., Horch, R., Arkudas, A., Labanaris, A., Brune, K., Greil, P., Bach, A. D., Kopp, J., Hess, A., Kneser, U., et al. (2006). Intrinsic versus extrinsic vascularization in tissue engineering. In *Tissue Engineering*, pages 311–326. Springer.

Prendergast, M. E., Solorzano, R. D., and Cabrera, D. (2017). Bioinks for biofabrication: current state and future perspectives. *Journal of 3D printing in medicine*, 1(1):49–62.

Ritossa, F. (1962). A new puffing pattern induced by temperature shock and dnp in drosophila. *Experientia*, 18(12):571–573.

Rouwkema, J., Rivron, N. C., and van Blitterswijk, C. A. (2008). Vascularization in tissue engineering. *Trends in biotechnology*, 26(8):434–441.

Rouwkema, J., Westerweel, P. E., De Boer, J., Verhaar, M. C., and Van Blitterswijk, C. A. (2009). The use of endothelial progenitor cells for prevascularized bone tissue engineering. *Tissue Engineering Part A*, 15(8):2015–2027.

Roux, B. M., Akar, B., Zhou, W., Stojkova, K., Barrera, B., Brankov, J., and Brey, E. M. (2018). Preformed vascular networks survive and enhance vascularization in critical sized cranial defects. *Tissue Engineering Part A*, 24(21-22):1603–1615.

Roversi, K., Orimi, H. E., Erfanian, M., Talbot, S., and Boutopoulos, C. (2022). List: A newly developed laser-assisted cell bioprinting technology. *Bio-protocol*, 12(19):e4527–e4527.

Salameh, S., Tissot, N., Cache, K., Lima, J., Suzuki, I., Marinho, P. A., Rielland, M., Soeur, J., Takeuchi, S., Germain, S., et al. (2021). A perfusable vascularized full-thickness skin model for potential topical and systemic applications. *Biofabrication*, 13(3):035042.

Satchell, S. C. and Braet, F. (2009). Glomerular endothelial cell fenestrations: an integral component of the glomerular filtration barrier. *American Journal of Physiology-Renal Physiology*, 296(5):F947–F956.

Schöneberg, J., De Lorenzi, F., Theek, B., Blaeser, A., Rommel, D., Kuehne, A. J., Kießling, F., and Fischer, H. (2018). Engineering biofunctional in vitro vessel models using a multilayer bioprinting technique. *Scientific reports*, 8(1):1–13.

Serban, M. A., Liu, Y., and Prestwich, G. D. (2008). Effects of extracellular matrix analogues on primary human fibroblast behavior. *Acta biomaterialia*, 4(1):67–75.

Serini, G., Ambrosi, D., Giraudo, E., Gamba, A., Preziosi, L., and Bussolino, F. (2003). Modeling the early stages of vascular network assembly. *The EMBO journal*, 22(8):1771–1779.

Serra, P. and Piqué, A. (2019). Laser-induced forward transfer: fundamentals and applications. *Advanced Materials Technologies*, 4(1):1800099.

Smith, C. M., Stone, A. L., Parkhill, R. L., Stewart, R. L., Simpkins, M. W., Kachurin, A. M., Warren, W. L., and Williams, S. K. (2004). Three-dimensional bioassembly tool for generating viable tissue-engineered constructs. *Tissue engineering*, 10(9-10):1566–1576.

Solis, L. H., Ayala, Y., Portillo, S., Varela-Ramirez, A., Aguilera, R., and Boland, T. (2019). Thermal inkjet bioprinting triggers the activation of the vegf pathway in human microvascular endothelial cells in vitro. *Biofabrication*, 11(4):045005.

Steffens, L., Wenger, A., Stark, G. B., and Finkenzeller, G. (2009). In vivo engineering of a human vasculature for bone tissue engineering applications. *Journal of cellular and molecular medicine*, 13(9b):3380–3386.

Stratman, A. N., Pezoa, S. A., Farrelly, O. M., Castranova, D., Dye III, L. E., Butler, M. G., Sidik, H., Talbot, W. S., and Weinstein, B. M. (2017). Interactions between mural cells and endothelial cells stabilize the developing zebrafish dorsal aorta. *Development*, 144(1):115–127.

Sweet, R. G. (1965). High frequency recording with electrostatically deflected ink jets. *Review of scientific instruments*, 36(2):131–136.

Swift, M. R. and Weinstein, B. M. (2009). Arterial–venous specification during development. *Circulation research*, 104(5):576–588.

Takahashi, K., Tanabe, K., Ohnuki, M., Narita, M., Ichisaka, T., Tomoda, K., and Yamanaka, S. (2007). Induction of pluripotent stem cells from adult human fibroblasts by defined factors. *cell*, 131(5):861–872.

Tamplenizza, M., Tocchio, A., Gerges, I., Martello, F., Martelli, C., Ottobrini, L., Lucignani, G., Milani, P., and Lenardi, C. (2015). In vivo imaging study of angiogenesis in a channelized porous scaffold. *Molecular Imaging*, 14(6):7290–2015.

Tröndle, K., Koch, F., Finkenzeller, G., Stark, G. B., Zengerle, R., Koltay, P., and Zimmermann, S. (2019). Bioprinting of high cell-density constructs leads to controlled lumen formation with self-assembly of endothelial cells. *Journal of tissue engineering and regenerative medicine*, 13(10):1883–1895.

Tufro-McReddie, A., Norwood, V., Aylor, K., Botkin, S., Carey, R., and Gomez, R. (1997). Oxygen regulates vascular endothelial growth factor-mediated vasculogenesis and tubulogenesis. *Developmental biology*, 183(2):139–149.

Unger, C., Gruene, M., Koch, L., Koch, J., and Chichkov, B. N. (2011). Time-resolved imaging of hydrogel printing via laser-induced forward transfer. *Applied Physics A*, 103(2):271–277.

Unger, R. E., Sartoris, A., Peters, K., Motta, A., Migliaresi, C., Kunkel, M., Bulnheim, U., Rychly, J., and Kirkpatrick, C. J. (2007). Tissue-like self-assembly in cocultures of endothelial cells and osteoblasts and the formation of microcapillary-like structures on three-dimensional porous biomaterials. *Biomaterials*, 28(27):3965–3976.

Vunjak-Novakovic, G., Obradovic, B., Martin, I., Bursac, P. M., Langer, R., and Freed, L. E. (1998). Dynamic cell seeding of polymer scaffolds for cartilage tissue engineering. *Biotechnology progress*, 14(2):193–202.

Wahlberg, B., Ghuman, H., Liu, J. R., and Modo, M. (2018). Ex vivo biomechanical characterization of syringe-needle ejections for intracerebral cell delivery. *Scientific reports*, 8(1):1–17.

Wang, L., Fan, H., Zhang, Z.-Y., Lou, A.-J., Pei, G.-X., Jiang, S., Mu, T.-W., Qin, J.-J., Chen, S.-Y., and Jin, D. (2010). Osteogenesis and angiogenesis of tissue-engineered bone constructed by prevascularized β-tricalcium phosphate scaffold and mesenchymal stem cells. *Biomaterials*, 31(36):9452–9461.

Wijshoff, H. (2010). The dynamics of the piezo inkjet printhead operation. *Physics reports*, 491(4-5):77–177.

Winkler, E. A., Bell, R. D., and Zlokovic, B. V. (2011). Central nervous system pericytes in health and disease. *Nature neuroscience*, 14(11):1398–1405.

Wu, P. and Ringeisen, B. (2010). Development of human umbilical vein endothelial cell (huvec) and human umbilical vein smooth muscle cell (huvsmc) branch/stem structures on hydrogel layers via biological laser printing (biolp). *Biofabrication*, 2(1):014111.

Wu, P., Ringeisen, B., Callahan, J., Brooks, M., Bubb, D., Wu, H., Piqué, A., Spargo, B., McGill, R., and Chrisey, D. (2001). The deposition, structure, pattern deposition, and activity of biomaterial thin-films by matrix-assisted pulsed-laser evaporation (maple) and maple direct write. *Thin Solid Films*, 398:607–614.

Wu, W., DeConinck, A., and Lewis, J. A. (2011). Omnidirectional printing of 3d microvascular networks. *Advanced materials*, 23(24):H178–H183.

Xiong, R., Zhang, Z., Shen, J., Lin, Y., Huang, Y., and Chrisey, D. B. (2015). Bubble formation modeling during laser direct writing of glycerol solutions. *Journal of Micro and Nano-Manufacturing*, 3(1).

Xu, T., Olson, J., Zhao, W., Atala, A., Zhu, J.-M., and Yoo, J. J. (2008). Characterization of cell constructs generated with inkjet printing technology using in vivo magnetic resonance

imaging. *Journal of manufacturing science and engineering*, 130(2).

Yamazaki, T. and Mukouyama, Y.-s. (2018). Tissue specific origin, development, and pathological perspectives of pericytes. *Frontiers in Cardiovascular Medicine*, 5:78.

Yanez, M., Rincon, J., Dones, A., De Maria, C., Gonzales, R., and Boland, T. (2015). In vivo assessment of printed microvasculature in a bilayer skin graft to treat full-thickness wounds. *Tissue Engineering Part A*, 21(1-2):224–233.

Yu, H., VandeVord, P. J., Mao, L., Matthew, H. W., Wooley, P. H., and Yang, S.-Y. (2009). Improved tissue-engineered bone regeneration by endothelial cell mediated vascularization. *Biomaterials*, 30(4):508–517.

Zhang, B., Korolj, A., Lai, B. F. L., and Radisic, M. (2018). Advances in organ-on-a-chip engineering. *Nature Reviews Materials*, 3(8):257–278.

Zhang, Y., Xia, L., Zhai, D., Shi, M., Luo, Y., Feng, C., Fang, B., Yin, J., Chang, J., and Wu, C. (2015). Mesoporous bioactive glass nanolayer-functionalized 3d-printed scaffolds for accelerating osteogenesis and angiogenesis. *Nanoscale*, 7(45):19207–19221.

Zhang, Z., Xu, C., Xiong, R., Chrisey, D. B., and Huang, Y. (2017). Effects of living cells on the bioink printability during laser printing. *Biomicrofluidics*, 11(3):034120.

Zheng, F., Derby, B., and Wong, J. (2021). Fabrication of microvascular constructs using high resolution electrohydrodynamic inkjet printing. *Biofabrication*, 13(3):035006.

Appendix A

MATLAB programs

We coded several MATLAB programs to analyze our microscopy images and help in their quantification. Herein, we have provided the programs that were used for this project.

A.1. Measurement of the circularity and the radius of the model ink droplets

```
clc;clear all;
close all;
Ratio = 2.1361;    % Ratio um/pixel using hemocytometer for the 4X lens
RadThreshold = 80;
% Threshold that lets you filter the small areas that you don't want. ...
    Radius in um
Im = imread('J:\EVOS\BF\3\20hz-80uj-1x-p3005.tif');    % Read file/image
[J,rect] = imcrop (Im);    % Manually select the area to keep (the area ...
    to crop)
% and rect will store the important values of the drawn rectangle
Icroped = Im(floor(rect(2)):floor(rect(2)+rect(4)),floor(rect(1))...
    :floor(rect(1)+rect(3)),:);
figure (1)
imshow(Icroped)    % Displays the image
```

```
13 Im = rgb2gray(Icroped);     % Turns image to gray
14 bwB = im2bw(Im,graythresh(Im));     % Turns image to black and white
15 bwB = imcomplement(bwB);     % Black becomes white and white becomes black
16 bw2B = imfill(bwB,'holes');     % Fills if any black area in white circle
17 Properties = regionprops(bw2B,{'Centroid','Area', 'Circularity'});
18 % Analyzes the image by different regions and calculates
19 % the Area and centroid (x,y position) for each region
20 hold on
21 Count = 1;     % Counter independent of the one in the for
22 % loop to avoid getting array indexes with nothing in it
23 imshow(bw2B)
24
25 for i=1:length(Properties)
26     if sqrt((Properties(i).Area)/pi)*Ratio > RadThreshold
27         % Filters the small areas that are not actual droplets
28         images.roi.Circle(gca,'Center',Properties(i)...
29             .Centroid,'Radius',sqrt((Properties(i).Area)/pi));
30         % Draws a circle with the radius calculated from the area that ...
               we got above
31         % over the already opened graph (gca) and puts the center on ...
               the Centroid
32         AREAS(Count)   = Properties(i).Area;
33         % Creates a matrix with all the areas that pass the if condition
34         RADIUS(Count) = sqrt((Properties(i).Area)/pi);
35         % Creates a matrix with all the radiuses that pass the if condition
36         CIRC(Count) = Properties(i).Circularity;
37         % Creates a matrix with all the circularity ratio (between 0 ...
               and 1)
38         Count=Count+1;     % Increments counter when the if condition is ...
               true
39         hold on
40     end
41 end
```

```
42
43 %%
44 AREAS_UM2 = (Ratio^2)*AREAS    % Transforms pixel^2 to um^2 for the area
45 RADIUS_UM = Ratio*RADIUS    % Transforms pixel into um for the radiuses
46 CIRC
47
48 a = [CIRC' RADIUS_UM']
```

A.2. The live/dead cell detection of stained HUVEC samples

```
1  clc;clear all;close all;
2  Ratio = 0.664;
3  TimesG=5;
4  NAME_blue = '22 Aug\Day3\Control\blue.png';
5  NAME_green = '22 Aug\Day3\Control\green.png';
6  B = imread(NAME_blue);
7  G = imread(NAME_green);
8  [ValG IdxG] = imcrop(G);
9  MatG=reshape(ValG,[size(ValG,1)*size(ValG,2) 1]);
10 Thre_intensity_G = mean(double(MatG))+TimesG*std(double(MatG));
11 TotalCell=0;
12 TotalAliveCell=0;
13 [ValP,IdxP] = imcrop(B);
14 View = floor(IdxP);
15 VIEW=View(1);
16 for ii=1
17     [Val Idx]=imcrop(B,[View(1)  View(2)  View(3)  View(4)]);
18     IMB=B(floor(Idx(2)):floor(Idx(2))+floor(Idx(4)),floor(Idx(1))...
19         :floor(Idx(1))+floor(Idx(3)));
```

```
20      IMG=G(floor(Idx(2)):floor(Idx(2))+floor(Idx(4)),floor(Idx(1))...
21          :floor(Idx(1))+floor(Idx(3)));
22
23      %%
24      I = adapthisteq(IMB);
25      I = imclearborder(I);
26      I = wiener2(I, [5 5]);
27      bw = im2bw(I, graythresh(I));
28      bw2 = imfill(bw,'holes');
29      bw3 = imopen(bw2, strel('disk',2));
30      bw4 = bwareaopen(bw3, 100);
31      bw4_perim = bwperim(bw4);
32      overlay1 = imoverlay(I, bw4_perim, [1 .3 .3]);
33      maxs = imextendedmax(I,  5);
34      maxs = imclose(maxs, strel('disk',3));
35      maxs = imfill(maxs, 'holes');
36      maxs = bwareaopen(maxs, 2);
37      overlay2 = imoverlay(I, bw4_perim | maxs, [1 .3 .3]);
38      Jc = imcomplement(I);
39      I_mod = imimposemin(Jc, ¬bw4 | maxs);
40      L = watershed(I_mod);
41      labeledImage = label2rgb(L);
42      [L, num] = bwlabel(L);
43      mask = im2bw(L, 1);
44      overlay3 = imoverlay(I, mask, [1 .3 .3]);
45
46      %%
47      Properties = regionprops(mask,IMB,...
48          {'Centroid','Area','Circularity','WeightedCentroid'});
49      Ifinal(:,:,2)=IMG;
50      Ifinal(:,:,3)=IMB;
51      imshow(Ifinal)
52      CountLive=0;
```

```
53      FinalLiveDropPro=[];
54      AllCell=-1;
55
56      for i=1:length(Properties)
57          AllCell=AllCell+1;
58          Cent = Properties(i).Centroid;
59          hold on
60          plot(Cent(1),Cent(2),'b+','MarkerSize',1)
61          IMR_AVG=[IMG(floor(Cent(2)),floor(Cent(1))),...
62              IMG(floor(Cent(2))+1,floor(Cent(1))+1), ...
63              IMG(floor(Cent(2))-1,floor(Cent(1))-1), ...
64              IMG(floor(Cent(2))-1,floor(Cent(1))+1), ...
65              IMG(floor(Cent(2))+1,floor(Cent(1))-1)];
66          if (mean(double(IMR_AVG))>Thre_intensity_G )
67              CountLive=CountLive+1;
68              plot(Cent(1),Cent(2),'g*','MarkerSize',10)
69              LastLiveDropPro=[Cent(1) Cent(2) ...
70                  (Ratio^2)*Properties(i).Area Properties(i).Circularity];
71              FinalLiveDropPro=[FinalLiveDropPro;LastLiveDropPro];
72          else
73          plot(Cent(1),Cent(2),'r*','MarkerSize',10)
74          end
75      end
76
77      AllCell;
78      Viability_prercentage=100*(CountLive)/(AllCell);
79      TotalAliveCell=TotalAliveCell+CountLive;
80      TotalCell=TotalCell+AllCell;
81      AliveEach(ii)=CountLive;
82      fprintf('number of living cells for droplet # %d is ...
            %4.2f\n',ii,CountLive)
83      All(ii)=AllCell;
84      fprintf('number of cells for droplet # %d is %4.2f\n',ii,AllCell)
```

```
85      ViabilityEach(ii)=Viability_prercentage;
86      fprintf('viability percentage for droplet # %d is ...
            %4.2f\n',ii,Viability_prercentage)
87  end
88
89  TotalViability=100*(TotalAliveCell)/(TotalCell);
90  fprintf('viability percentage is %4.2f\n',TotalViability)
91  ForViability=[All' AliveEach' ViabilityEach'];
92  figure
93  bar(ForViability)
94  xlabel('Droplets number')
95  legend('Number of the cells','Number of living cells','Viability ...
        percentage')
```

A.3. Boosting the SNR of the background in the IMR90 and HBPC recruitment images

```
1   folder = 'Experiments\HBPC\12 Sep\2nd sample\4th line\Red';
2   imRedFiles = dir(fullfile(folder,['Red*']));
3   for i = 1:size(imRedFiles, 1)
4       names{1, i} = char(imRedFiles(i).name);
5   end
6
7   [S,INDEX] = sort_nat(names);
8   for i = 1:size(S, 2)
9       fluoIm = imread([folder, '\', char(S(i))]);
10      Mask = (imbinarize(fluoIm(:,:,1), 'adaptive'));
11      Mask = imerode(Mask, strel('disk',2,6));
12      Mask = imdilate(Mask,strel('disk',2,6));
13      r = fluoIm(:,:,1);
```

```
14      g = fluoIm(:,:,2);
15      b = fluoIm(:,:,3);
16      r(Mask==0) = 0;
17      g(Mask==0) = 0;
18      b(Mask==0) = 0;
19      fluoIm(:,:,1) = r;
20      fluoIm(:,:,2) = g;
21      fluoIm(:,:,3) = b;
22      Name=['image ' num2str(i)];
23      imwrite(fluoIm,[folder '\' Name '.jpg'])
24  end
```